INVESTIGATION OF STRESS-DEPENDENT PERMEABILITY RELATED PROBLEMS FOR SHALE AND GULF OF MEXICO DEEPWATER RESERVOIRS WITH IN-HOUSE COUPLED FLOW-GEOMECHANICS SIMULATOR

A Dissertation

by

CHENG AN

Submitted to the Office of Graduate and Professional Studies of
Texas A&M University
in partial fulfillment of the requirements for the degree of

DOCTOR OF PHILOSOPHY

Chair of Committee,	John E. Killough
Committee Members,	Maria A. Barrufet
	Eduardo Gildin
	Hadi Nasrabadi
Head of Department,	Jeff Spath

May 2019

Major Subject: Petroleum Engineering

ABSTRACT

Reservoir compaction and stress changes could have considerable impacts on reservoir management and production performance under certain circumstances. To consider geomechanics effects and provide more realistic dynamic reservoir simulations, we have developed an in-house mathematical simulator coupling fluid flow and geomechanics behaviors on FORTRAN. The coupled simulator was validated by comparing with the analytical solutions of the Terzaghi's and Mandel consolidation problems. In this study, the developed coupled simulator is applied into four various reservoir applications, where unique physical mechanisms and additional geomechanics effects are added into the simulator.

Firstly, various stress-dependent permeability correlations and matrix shrinkage phenomenon are taken into account for the coupled model to investigate their impacts on permeability change during reservoir depletion and production performance for organic-rich shale reservoirs. Based on different rock properties and compaction behaviors, various stress-permeability correlations are separately applied into different sub-pore media (organic matter, inorganic matter, and natural fractures). Secondly, the coupled model usually encounters a large matrix system and high computational expenses for large-scale simulation problems, where the time stepping is a crucial factor for numerical stability and computational efficiency. We introduce an adaptive time stepping method with the modified local error technique to reduce iteration time and improve the computational efficiency for the coupled flow and geomechanics model.

Thirdly, the permeability reduction derived from Pressure Transient Analysis (PTA) appears more severe than the permeability decline measured from core samples for Gulf of Mexico (GOM) Deepwater turbidite reservoirs. Based on the provided laboratory measurements and recorded-field data, we present a comparison study between laboratory-measured and field-derived permeability loss under compaction effects. Irreversible compressibility and permeability hysteresis are proposed to explain the difference with the support of numerous simulation results. Fourthly, correct measurement of stress-dependent permeability is critical for production prediction and economic evaluation of shale reservoirs. However, stress creep and effective stress coefficient still present difficulties in correctly measuring and interpreting stress-dependent permeability for cores-based measurements. An improved stress-dependent permeability model is derived to consider the effect of time-dependent compaction behavior on permeability measurements by incorporating the stress creep mechanism. Additionally, how to correctly interpret stress-dependent permeability results with appropriate effective stress coefficient is introduced in detail.

DEDICATION

To my mom

ACKNOWLEDGEMENTS

My deepest appreciation goes to my advisor, Dr. John Killough. I have been working with Dr. Killough for seven years since my M.S. program, during which I have learned a lot from him both in research and other aspects of life. Without his numerous guide and support, I could never have completed this journey and reached where I am now.

I would like to thank my committee members, Dr. Maria Barrufet, Dr. Eduardo Gildin, and Dr. Hadi Nasrabadi, for their guidance and support throughout the course of this research. I am very grateful to Dr. Bryan Maggard, for providing me teaching experience and valuable discussions.

Many Thanks also go to my friends, colleagues, the department faculty and staff for making my time in Richardson Petroleum Engineering Building a great experience, especially to Bicheng Yan, Masoud Alfi, Xuyang Guo, and Lidong Mi for our enjoyable collaboration.

Finally, I would like to take this opportunity to thank my beloved mother Nianzhen Mao, my father Hanping An, and my wife Xiangjun Wu for their unconditional love, support and understanding all the time.

CONTRIBUTORS AND FUNDING SOURCES

Contributors

This work was supervised by a dissertation committee consisting of Professor John E. Killough (advisor), Eduardo Gildin, and Hadi Nasrabadi of the Department of Petroleum Engineering and Professor Maria A. Barrufet of the Department of Chemical Engineering.

The basic formulations for the modeling of fluid flow were collaborated with Bicheng Yan and Masoud Alfi. The coupled model validation was conducted in discussions with Xuyang Guo. The data analyzed for Chapter V was provided by Eni S.p.A. and the history matching was collaborated with Professor John E. Killough.

All other work conducted for the dissertation was completed by the student independently.

Funding Sources

Graduate study was supported by a fellowship from Crisman Institute for Petroleum Research and the financial support from Eni.

TABLE OF CONTENTS

Page

LIST OF FIGURES

Page

LIST OF TABLES

Page

CHAPTER I

INTRODUCTION

1.1 Background and Motivation

1.1.1 Organic-rich Shale Reservoirs

With the advanced technologies of multistage fracturing and horizontal drilling, the well productivity has been significantly improved for extra-low permeability formations, which results in huge amounts of hydrocarbons economically produced from shale reservoirs. Shale gas reservoirs have become an increasingly important resource of natural gas in United States. The increasing tread of exploration and production is expected to continue for providing more gas supply and satisfying growing energy demands. Many analysts predict that shale gas will be extensively explored around the world and greatly expand worldwide energy supply. Shale gas reservoirs are typically extraordinarily fine-grained sediments with low porosity and extra-low permeability (Javadpour, 2009), which could be both reservoir rock and source rock. Organic matters are commonly existed in shale reservoirs, and they are typically reported as Total Organic Content (TOC) (Curtis et al. 2010; Ambrose et al. 2010; Loucks et al. 2012). Fig. 1 shows the kerogen network based on the three-dimensional (3D) Scanning Electron Microscope (SEM) images, where kerogen is a solid organic matter in sedimentary rocks. These organic matter can play important roles in petrophysical properties, rock permeability, rock compaction behaviors, and hydrocarbon reserve.

Jarvie (2004) evaluated the hydrocarbon generation and storage in the Barnett shale by experiments. He found both the free gas and adsorbed gas are existed in the shale matrix, and the amount is linearly increased with total organic carbon (TOC). By applying scanning electron microscope (SEM) images, different pore-media have been extensively observed in shale core samples: organic matter also known as kerogen, inorganic matter (such as clay, quartz, and carbonate), natural fractures, and hydraulic fractures. Due to different rock properties and flow mechanisms in each sub-pore medium, many authors have proposed to divide the organic-rich shale reservoir into multi-porous media in order to better capture different flow mechanisms and describe the gas flow processes in these different pore media (Wang and Reed 2009; An et al. 2015; An et al. 2016; Yan et al. 2016; Alfi et al. 2017). Yan et al. (2013) established a two phase micro model to divide shale matrix into various sub medium, where mixed wettability, high capillary pressure and the randomly distributed kerogen are taken into account to interpret the dynamic of gas and water flow at this micro scale level. In addition, as a result of tiny pore size and extra-low permeability, some non-Darcian flow mechanisms, such as gas diffusion, gas desorption, and slippage flow, are recommended to describe the transport of gas and liquid in shale (Javadpour 2009; Shabro et al. 2011; Civan et al. 2011; Wang et al. 2017)

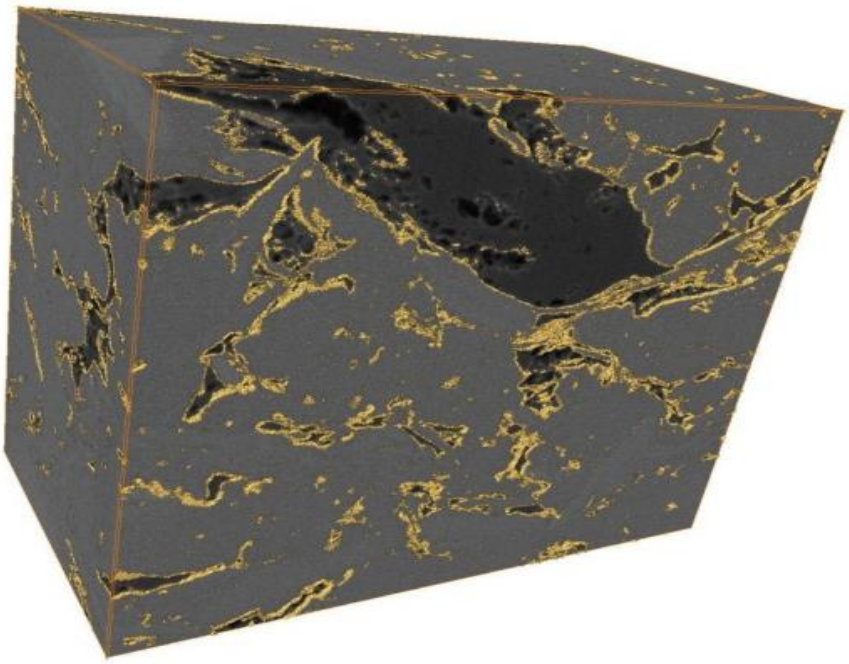

Figure 1: 3D SEM segmentation showing kerogen network, yellow color outlines the kerogen network (reprinted from Ambrose et al. 2010).

1.1.2 Coupled Flow-Geomechanics Model

Rock compressibility is often applied to calculate the change of pore volume under a defined loading condition for traditional reservoir simulations, where few major assumptions are required: the total stress is constant, the local-bridging effect around a grid block could be ignored, and the rock permeability and porosity is insensitive to the change of stress state (Chin et al., 2002; Alpak, 2015). These assumptions above are appropriate for reservoirs with competent rock, while they are not realistic for many weaker formations and complicated formations, such as unconventional shale reservoirs and Deepwater unconsolidated reservoirs. Furthermore, reservoir compaction and stress

changes can have considerable impacts on permeability change and production performance under many reservoir circumstances.

Soeder (1988) found the permeability decreases with an increase in confining pore pressure in the Marcellus shale. Gutierrez et al. (2000) performed an experimental study about the stress dependent permeability of demineralized fractures in shale. They presented the fracture permeability considerably decreases if the effective normal stress is increased. Bustin et al. (2008) stated the permeability of shale could vary by few orders of magnitude with different effective stresses. As shown on Fig. 2, their measured data showed the exponential dependence of shale permeability on effective stress for Barnett, Muskwa, and Ohio shale samples. Ali and Sheng (2015) concluded the effects of geomechanics has a significant impact on Haynesville shale by integrating RTA analysis and simulation study. By applying both steady state flow method and pulse-decay method to measure permeability of Eagle Ford core, Katsuki et al. (2016) stated the shale reservoir permeability exponentially decreases with the increase of net stress. Al Ismail and Zoback (2016) conducted pulse-decay permeability experiments on Utica and Permian shale samples. Their measurements show the permeability significantly decreases along with the increase of effective stress in an exponential relationship. Therefore, the geomechanics effects are necessary to be considered for many specific formations in order to provide more realistic dynamic flow prediction, especially for reservoirs associated with stress-dependent properties and formation subsidence.

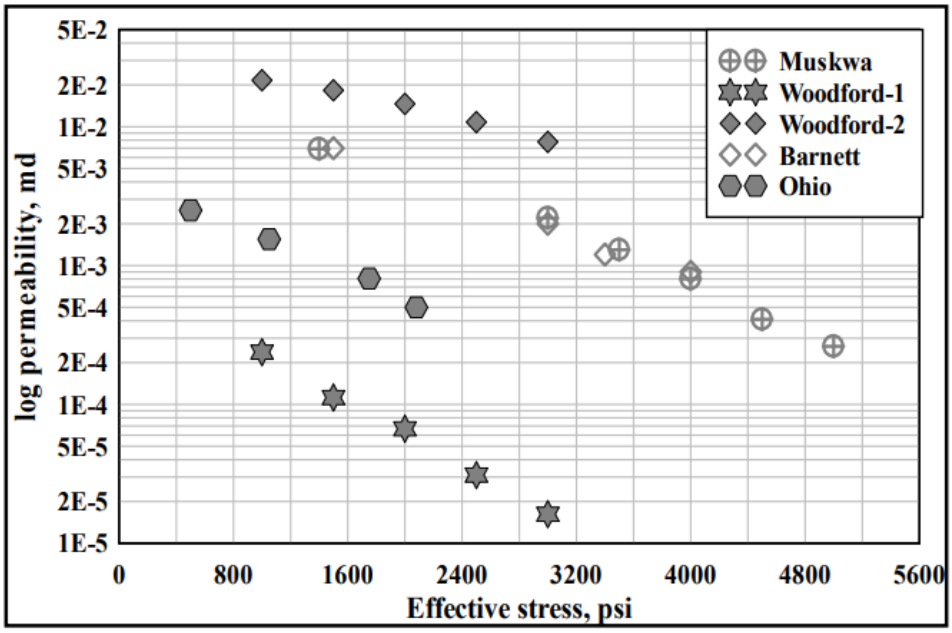

Figure 2: Pulse decay permeability under varying confining pressures for different shale rock samples (reprinted from Bustin et al. 2008).

Reservoir models coupling flow and geomechanics have been widely developed to study the rock movement and the geomechanics impacts on reservoir properties (Settari and Walters 1999; Minkoff et al. 2003; Dean et al. 2006; Samier and Gennaro 2008; Thornton and Crook 2014; An et al. 2017a & 2017b; Zhang et al. 2019). The coupled flow-geomechanics models are generally classified into three types: fully coupled, iteratively coupled, and loosely coupled. The fully coupled models solve the large nonlinear equations system of flow and geomechanics simultaneously at each iteration within every time step. The iteratively coupled models solve the two sets of equations sequentially and independently, where the flow and mechanics are coupled through the change of pore volume at the end of each time step. The loosely coupled models also solve

the two sets of equations independently, but the information between flow and mechanics is only exchanged at designated time intervals, not for every time step.

The fully coupled models are usually considered to provide the true solution of a coupled problem, while intensive computational cost and considerable work force are needed. The loosely coupled models can significantly decrease the computational cost, while it at best only provides an approximate solution and the numerical error cannot be ignored for many complex reservoirs. However, the iteratively coupled analysis can not only yield the true solution of coupled problems when the iterative process converges, but it also has several great advantages compared to the fully coupled analysis, such as much better computational efficiency, more easily to be implemented, and more flexible to be directly applied on existed flow and geomechanics codes. Therefore, many researchers and scholars have already chosen the iteratively coupled method for various coupled problems in deformable porous media.

Settari and Mourits (1994) put forward a sequential-implicit coupled method, where the flow equations are solved first, followed by the mechanics equations. By linking two computer codes TOUGH2 and FLAC3D, Rutqvist et al. (2002) presented a modeling approach for analysis of coupled multiphase fluid flow, heat transfer, and deformation in fractured porous rock. Jeannin et al. (2006) studied two accelerated algorithms for the iterative resolution of coupled reservoir-geomechanics problems. For the iteratively coupled approach, either the flow equations or the mechanics equations are solved first. Pan et al. (2013) integrated the two computer codes TOUGH2 and RDCA for coupled

hydromechanical analysis of multiphase fluid flow and discontinuous mechanical behavior in heterogeneous rock.

1.1.3 Stress-dependent Permeability Measurements

Permeability measurement is one of the critical parts to characterize reservoir and predict the production performance over the reservoir depletion life. Due to complex lithology and extra-low permeability, how to measure permeability for tight shale rock is different from the procedures of conventional rock samples. The most commonly utilized methods for measuring permeability of tight rock are steady state flow method, pulse-decay method, and crushed rock method (Tinni et al. 2012; Chhatre et al. 2014). Even though the crushed rock method is the cheapest, quickest, and most commercially available permeability measurements for tight rock, the measured results are largely variable with even two orders of magnitude difference based on some experimental data (Spears et al. 2011; Tinni et al. 2012). Another major issue of the crushed rock method is the absence of impacts of overburden stress and in-situ pore structures. On the other hand, many physical properties of porous rock vary as a function of stress. Based on the experimental data mentioned on the above section, reservoir compaction and stress change could have large effects on rock permeability, especially for low-permeability rock. Therefore, the permeability should be measured under various stress conditions to obtain the stress-dependent permeability trends in order to correctly predict the permeability change and production performance during reservoir depletion.

However, the stress creep phenomenon and effective stress coefficient still present challenge to the correct measurement of rock permeability, especially for organic-rich or clay-rich shale reservoirs. The stress creep is discussed in this paragraph, and the path-dependent stress will be discussed in next paragraph. Time dependent deformation of porous rock is an important factor for estimating dynamic rock properties. This phenomenon has been widely observed in laboratory creep measurements under constant loaded stress condition. The creep process under constant loaded stress is typically divided into three different stages: primary creep, secondary creep, and tertiary creep. Sone and Zoback (2011) studied the time dependent deformational properties of shale gas reservoir rocks by using a triaxial deformation apparatus in laboratory creep experiments. The results presented obvious increase of creep strain over time after instantaneous stress load as on Fig. 3, and they stated the amount of creep strain increases with clay content. By studying the elastic moduli and ductile creep behavior of shale gas reservoir rocks from Barnett, Haynesville, Eagle Ford, and Fort St. John shale plays in triaxial laboratory experiments, Sone and Zoback (2013) summarized the creep deformation is generally more obvious in core samples with higher clay and kerogen content.

Mighani et al. (2015) investigated the creep behavior of Wolfcamp shale reservoir at a small scale by using Nanoindentation. The measured creep of shale is comparably higher than other conventional rocks, such as Lyons sandstone and Indiana limestone. Additionally, they stated the creep process depends strongly on the rock composition, where TOC and clay content correlate positively with the creep. The change in volumetric strain caused by creep could result in the variation of rock porosity and permeability over

time. Sinha et al. (2013) and Chhatre et al. (2014) have observed the measured permeability significantly reduces over time for tight rock samples when all other variables keep constant. Fig. 4 shows measured oil permeability drastically decreases along with time under constant confining stress. They stated it was the stress creep that contributed to the decline of permeability over time, where the stress creep is defined as a reduction of measured porosity and permeability over time under the effect of the applied constant stress. Based on the experimental data above, permeability measurements could be considerably overestimated if we don't pay enough attention to the stress creep, which will in return provide incorrect rock characterization and prediction of productivity of targeted formations. Therefore, more studies are required to better understand the physics of creep phenomenon on shale rock and the impact of stress creep on permeability measurements.

The other important factor affecting permeability measurement is effective stress coefficient, which is highly related to path-dependent stress by determining how to calculate effective stress. As we explained in the above paragraph, rock properties including permeability are a function of stress. To be more specific, rock permeability depends on the net effective stress, which is defined as overburden pressure minus the product of pore pressure and effective stress coefficient: $\sigma_{\text{effective}} = p_{\text{confining}} - \alpha \times p_{\text{pore}}$. During the process of hydrocarbon production from reservoir, pore pressure is reduced to lead an increase of effective stress acted on rock surface. However, for laboratory measurements, it is often the confining stress that be changed to alter effective stress because of several reasons, such as apparatus requirement and the degree of

convenience. These two processes above provide different paths but same result to change effective stress. If the effective stress coefficient α is not equal to one, the certain decrease of pore pressure and the same amount of increase of confining pressure will result in different changes of effective stress. As a result, the stress-dependent permeability trend obtained from laboratory cannot be directly used to predict the permeability change during reservoir depletion.

Many results from experimental measurements have demonstrated the effective stress coefficient is not equal to one for some rock types, especially for the rock containing much soft materials, such as clay and kerogen. The soft materials with high compressibility are regarded as the major reason to lead the effective stress coefficient not equal to one. For these specific rock types, effective stress coefficient cannot be directly calculated from the Biot equation: $\alpha = 1 - \mathrm{K_{rock}}/\mathrm{K_{mineral}}$ because this equation is not applicable. Effective stress coefficient should be obtained from experimental measurements, where permeability should be measured under a series of both pore pressures and confining pressures. Different effective stress coefficients could bring inconsistent results of stress-dependent permeability trends and considerably different results in terms of prediction of production performance. Therefore, it is not a wise approach to directly apply the stress-dependent permeability trend obtained from laboratory (by changing confining stress) into reservoir-field prediction before we have determined effective stress coefficient is equal to one by experimental measurements.

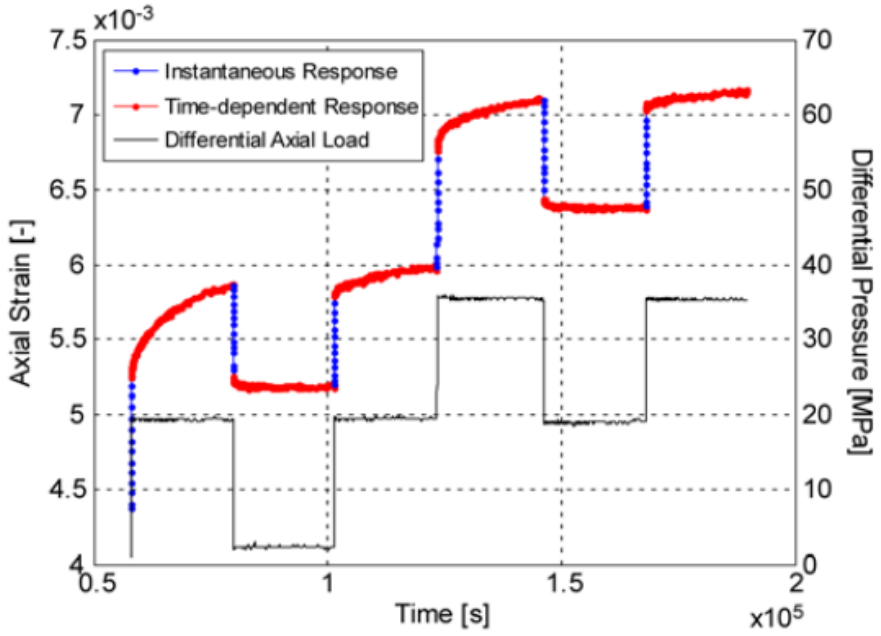

Figure 3: Creep observed during loading and re-loading process (reprinted from Sone and Zoback, 2011).

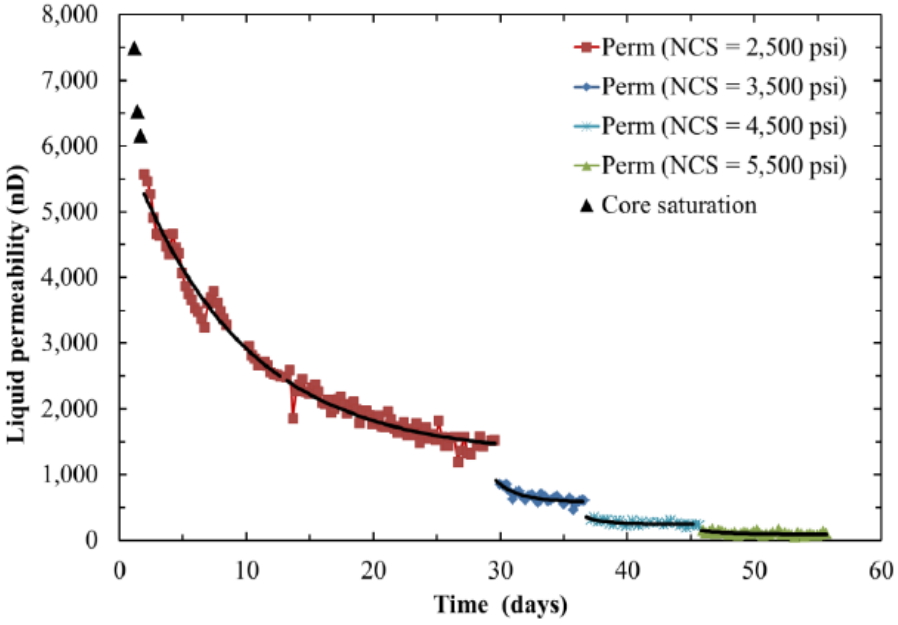

Figure 4: Measured oil permeability along with time at different net confining stresses (reprinted from Chhatre et al. 2014).

1.1.4 GOM Deepwater Reservoirs

Most reservoirs are initially in static stress equilibrium prior to the hydrocarbon production. However, during the hydrocarbon production process from reservoirs, the pore fluid pressure is decreased, and the effective stress acted on reservoir rock matrix is increased, which in return leads to reservoir compaction. Reservoir compaction can be an important drive mechanism to provide pressure support and improve production recovery. On the other hand, the unintended consequences of compaction are to reduce formation porosity and permeability, causing a decline of well productivity for both unconventional tight reservoirs and Deepwater unconsolidated reservoirs (Davies and Davies 2001; An et al. 2018 & 2019). Well stability and surface subsidence problems can be also brought by reservoir compaction. Reservoir compaction depends on the increase of effective stress, reservoir thickness, and reservoir rock compressibility (Nagel 2001). Reservoir thickness and rock compressibility are intrinsic characteristics of rock, which cannot be easily and largely changed. The increase of effective stress caused from the production of pore fluids is the main reason for the reservoir compaction problems above. Therefore, either to control the production rate or schedule the drawdown pressure is practice methods to manage the reservoir compaction problems, such as water injection is performed to maintain the reservoir pressure level.

Loss of formation integrity with the associated completion problems has been a continuing difficulty for many Gulf of Mexico offshore operators of fields with large formation compaction. Petro et al. (1997) evaluated the compaction effects in the Ewing Bank Block 873 field by using pressure transient testing. Their results demonstrated

reservoir compaction effects in Deepwater turbidite sands can significantly affect reservoir permeability and field production profiles, where the well deliverabilities can be reduced as much as 70%. Based on some core analysis related to the compaction effects for Deepwater Gulf of Mexico trubidites, Ostermeier (1996 & 2001) concluded compaction does significantly impact rock permeability. The observed relative reduction in permeability is generally approximately four to five times larger than the relative reduction in porosity. In addition, their measurements show pore volume compressibility can vary considerably in magnitude for different Deepwater GOM reservoirs. Pourciau et al. (2005) discussed the results and lessons learned through the first four years of the Chevron's Genesis project in the areas of well performance and reservoir management. They found reservoir compaction has significantly impacted well productivity during the first four years of production at Genesis, and several wells have lost more than 80% of the original permeability. One significant lesson they learned related to reservoir compaction is that the compaction impacts measured from core samples in laboratory severely underestimated the actual compaction observed from the Genesis reservoirs. Guenther et al. (2005) presented a case study in reservoir management of a compaction gas reservoir in the Deepwater Gulf of Mexico. The reservoir consists of turbidite unconsolidated sands separated by thin shales. Pressure transient analysis have been conducted and their analyses have shown up to 80% reduction of the original flow capacity for several wells. Additionally, the quantitative impact of compaction could not be predicted directly from core samples in laboratory.

Shumbera and Wang (2008) presented a comparison of laboratory-measured permeability loss trends with the permeability loss evaluated from well production performance for two Deepwater GOM oil field. They stated Gulf of Mexico Deepwater turbidite reservoirs often experience substantial compaction permeability loss due to increasing compaction impacts, which in return affect production rate, drainage areas, and ultimate recovery. More importantly, their results showed the permeability decline evaluated from field production data is much larger than the permeability loss from the core-measurements in laboratory. Based on all available data, Fig. 5 shows the difference of generalized permeability loss trends between laboratory-measured method and PTA-derived approach, where PTA stands for Pressure Transient Analysis. Therefore, the trend of permeability decline from laboratory measurements cannot be directly used to predict the actual permeability drop in GOM Deepwater reservoirs. In other words, the reservoir permeability and production performance will be overestimated if the core-measured stress-dependent permeability is directly used for the reservoir modeling and management.

Even though different mechanisms, such as grain particle rotation and crushing, different stress paths measuring core permeability, relative permeability changes, and fines migration, have been proposed to explain why the permeability loss observed from production performance is larger than the core-measured, all available information from the Genesis field (Pourciau et al. 2005) indicated the permeability losses were actual losses caused by reservoir compaction. Meanwhile, their studies indicated the relative permeability change and asphaltene deposition were not the cause. Overall, reservoir compaction can result in extremely high loss in reservoir permeability along with the

reservoir depletion and then significantly affect production performance and field development in the Gulf of Mexico Deepwater turbidite reservoirs. Therefore, the improved understanding of the compaction mechanisms within these unconsolidated formations and their dynamic effects on reservoir properties and production performance is significantly required, especially for the typical high-cost and high-uncertainty Deepwater reservoirs. Compaction analysis and prediction should be an integral part of the Deepwater field development and reservoir management.

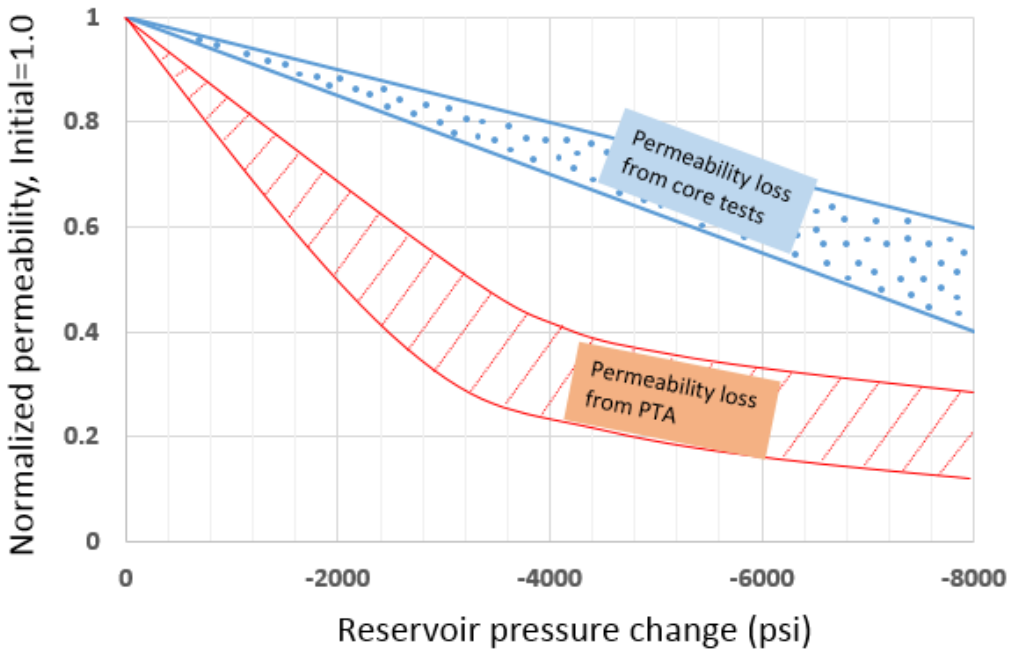

Figure 5: Generalized permeability loss trends from lab-measured and PTA-derived.

1.2 Study Objectives

In this study, an in-house mathematical simulator coupling fluid flow and geomechanics behaviors have been developed to investigate the effects of reservoir compaction and stress change on stress-dependent rock properties and production performance for shale reservoirs and Gulf of Mexico Deepwater reservoirs. Based on the background and motivations we introduced above, the study's objectives are briefly described as follows:

(1) An in-house mathematical simulator coupling fluid flow process and geomechanics effects is developed on FORTRAN. The code should be capable of being added any other physical mechanisms and function modules.

(2) The stress-dependent permeability correlations and matrix shrinkage of organic matter are added into the coupled model to investigate their effect on permeability change during reservoir depletion and production performance for organic-rich shale reservoirs.

(3) An adaptive time stepping method with the modified local error technique is proposed to reduce the total iteration time and improve the computational efficiency for the coupled flow-geomechanics model.

(4) A comparison study between laboratory-measured and field-derived permeability decline under compaction effects is presented for Gulf of Mexico (GOM) Deepwater unconsolidated reservoirs. Irreversible compressibility and permeability hysteresis are proposed to explain the permeability difference with the support of simulation results.

(5) An improved stress-dependent permeability model is derived to consider the effect of time-dependent compaction behaviors on permeability measurements by incorporating the stress creep mechanism. Additionally, how to correctly interpret stress-dependent permeability results with approximate effective stress coefficient is introduced in detail.

1.3 Organization of the Dissertation

In the following chapters, we will demonstrate how we solve each unique reservoir problem and achieve the objectives above in detail. The organization of the dissertation is described as follows:

Chapter I: General introduction to the background, motivations, and objectives of this study.

Chapter II: Development and validation of the coupled flow and geomechanics simulator, where how to derive and solve governing equations of the coupled model is thoroughly presented.

Chapter III: The coupled model is applied to investigate the effects of stress change and matrix shrinkage on reservoir permeability and production performance, where different stress-permeability correlations are separately applied to organic matter, inorganic matter, and natural fractures.

Chapter IV: An adaptive time stepping method with the modified local error approach is proposed to improve the computational efficiency for the coupled model. The numerical results and sensitivity analysis are shown as well.

Chapter V: A comparison between laboratory-measured and field-derived permeability decline trends under compaction effects is presented for Gulf of Mexico Deepwater reservoirs, where the laboratory-measured data, field-recorded data, and simulation results are displayed.

Chapter VI: A creep stain model and an improved stress-dependent permeability model are derived to describe the effects of time-dependent compaction behaviors on permeability measurements by incorporating the stress creep mechanism. Additionally, the influences of effective stress coefficient on interpreting stress-dependent permeability results are also studied.

Chapter VII: Conclusions of this study and recommendations for future work.

CHAPTER II

COUPLED FLOW AND GEOMECHANICS MODEL*

2.1 Iteratively Coupled Method

Based on Terzaghi's (1925) consolidation theory and the concept of effective stress, Biot (1941, 1956) developed a general theory describing fluid-solid coupling problems. Fung et al. (1994) displayed examples of multiphase flow by the iteratively coupled approach. Armero and Simo (1992) presented an unconditionally stable scheme based on an undrained split of the flow and mechanics problems. Chin et al. (2002) proposed an iterative procedures for coupled analysis of geomechanics and multi-phase flow in reservoir simulation for large-scale, full-field, and three-dimensional problems. Tran et al. (2004) developed a novel porosity formula for the iterative coupling of stress and flow to reduce the iteration number and improve the accuracy. As we mentioned in the introduction section, the iteratively coupled method can provide accurate solution, significantly better computational efficiency, and excellent flexibility for applications. In addition, Kim et al. (2011a) investigated the stability analysis for poro-elasticity and poro-elasto-plasticity with single-phase flow for four different sequential methods. They strongly recommended the fixed-stress split approach in terms of stability, consistency,

* Part of data reported in this chapter is reprinted with permission from "Stress-dependent Permeability of Organic-rich Shale Reservoirs: Impacts of Stress Changes and Matrix Shrinkage" by An, C., Killough, J., Mi, L., 2019. Journal of Petroleum Science and Engineering, Volume 172, Pages 1034-1047, Copyright 2019 by Elsevier. Part of data reported in this chapter is reprinted with permission from "A Modified Local Error Method for Adapting Time Step-size in Coupled Flow-geomechanics Problems" by An, C., Wang, Y., Wang, Y., Killough, J., 2018. Journal of Petroleum Science and Engineering, Volume 162, Pages 763-773, Copyright 2018 by Elsevier.

accuracy, and efficiency. Latterly, Kim et al. (2011b) specifically analyzed the stability and convergence for the fixed-strain split and fixed-stress split methods for coupled flow and geomechanics, and they showed the fixed-stress split is unconditionally stable with great accuracy. Therefore, the iteratively (sequential) coupled method will be applied for the development of coupled flow and geomechanics model in this study, where the fixed-stress split method is chosen to be used. This sequential coupled method is implemented by using the Galerkin Finite Element Method for the mechanics balance equations and the finite difference method for the mass balance equations, where fluid pressure (and saturation) and solid displacement are chosen as primary variables.

2.2 Mathematical Equations

2.2.1 Governing Equations for Fluid Flow

The sequential iteratively coupled method is applied for the coupled flow and geomechanics model, where the governing equations for fluid flow and geomechanics are separately solved at each time step. The governing equations for fluid flow and geomechanics are derived separately based on the mass balance and linear momentum balance. Since the fixed-stress technique is used with the sequential coupled method, the governing equations of fluid flow are solved first, and then the governing equations of geomechanics are solved next. If we turn off the geomechanics modules, the coupled model will become a pure reservoir flow simulation model. Therefore, we will separately show how to derive the governing equations for fluid flow and geomechanics. This section is for reservoir fluid flow, and next section is for geomechanics.

The mass balance equations and energy balance equation are generally described as on Eq. (1) for every grid block of simulation domain. The mass accumulation terms for water, oil, gas, and heat are calculated based on Eq. (2) to (5). Currently, the partitioning of the mass components among multi-phase is not considered. For example, the component of gas only exist in the gas phase, not in aqueous and organic phase. The mass flux terms for water, oil, gas, and heat are calculated based on Eq. (6) to (9). As shown on Eq. (8), gas diffusion and desorption have been taken into account for mass accumulation of gas. The effective Netwon-Raphson iteration method is used to solve the mass balance equation, and the continuum equations are discretized in time and space by using the integral finite difference method. Eq. (10) shows the residual terms that should reach to zero when the simulation converges. Since a mass balance equation exists for each component (water, oil, and gas), there is a residual equation as Eq. (10) to be solved for each component. The number of unknown variables is equal to the number of residual equation.

By expending the Taylor series with only first order term remained, Eq. (11) displays how the primary variable is updated by Newton Raphson iteration method, where both the residual and Jacobian terms are needed to be calculated in advance. We firstly starts with an initial reasonable guess for $x_{i,p}$, and $x_{i,p+1}$ can be computed from Equation (11), where $\partial R_n/\partial x_i$ is the Jacobian matrix. In each grid block, pressure, saturation, and temperature are the primary unknown variables to be solved, where the primary variables depend on reservoir initial conditions. By applying Eq. (11), $x_{i,p+1}$ is iteratively calculated, and the iteration is continued until the residuals $R_n^{k,t+1}$ is smaller than a given

convergence tolerance according to Eq. (12). If convergence cannot be achieved within a certain number of iterations, the time step size Δt will be reduced and a new iteration process is started.

$$\frac{\partial}{\partial t} M_l = \nabla \cdot \left(\overrightarrow{F_l}\right) + \sum Q_l \tag{1}$$

$$M_w = \phi S_w \rho_w \tag{2}$$

$$M_o = \phi S_o \rho_o \tag{3}$$

$$M_g = \phi S_g \rho_g + \rho_s \rho_{g_{std}} \frac{V_L P_g}{P_L + P_g} (1 - \phi) \tag{4}$$

$$M_h = (1 - \phi) \rho_R C_R T + \sum_{l=w,o,g} \phi S_l \rho_l U_l \tag{5}$$

$$\overrightarrow{F_w} = -\rho_w k \frac{k_{rw}}{\mu_w} (\nabla P_w - \rho_w \vec{g}) \tag{6}$$

$$\overrightarrow{F_o} = -\rho_o k \frac{k_{ro}}{\mu_o} (\nabla P_o - \rho_o \vec{g}) \tag{7}$$

$$\overrightarrow{F_g} = -\rho_g \, k \frac{k_{rg}}{\mu_{\,g}} \left(1 + \frac{b}{P_g}\right) \left(\nabla P_g - \rho_g \, \vec{g}\right) + \rho_g \, D_g c_g \nabla P_g \tag{8}$$

$$\overrightarrow{F_h} = -\left[(1 - \phi) K_R + \phi \left(S_w K_w + S_o K_o + S_g K_g\right)\right] \nabla T + \sum_{l=w,o,g} h_l \overrightarrow{F_l} \tag{9}$$

$$R_n^{l,t+1} = M_n^{l,t+1} - M_n^{l,t} - \frac{\Delta \mathrm{t}}{V_n} \left(\sum_m A_{nm} F_{nm}^{l,t+1} + V_n q_n^{l,t+1}\right) = 0 \tag{10}$$

$$x_{i,p+1} = x_{i,p} - \frac{R_n^{t+1}(x_{i,p})}{\partial R_n^{t+1} / \partial x_i} \tag{11}$$

$$\left|\frac{R_n^{t+1}}{M_n^{t+1}}\right| \leq \varepsilon_1 \tag{12}$$

Where the subscript l stands for the index of component, such as water (w), oil (o), and gas (g), M indicates mass accumulation of component l, F denotes the mass flux of component l, Q represents the source and sink term of component l, t represents time, ϕ is media porosity, S denotes saturation of component l, ρ stands for component density of

component l, ρ_s represents the skeleton density of the porous media, $\rho_{g_{std}}$ stands for gas density at standard pressure and temperature (273.15 K and 101.325 Pa), V_L denotes Langmuir volume, P_L denotes Langmuir pressure, P_g stands for gas pressure, M_h indicates heat accumulation, ρ_R denotes rock density, C_R represents heat capacity of the dry rock, T stands for rock temperature, U indicates specific internal energy of component l, k indicates the absolute permeability of porous media, k_{rl} represents the relative permeability of component l, μ_l stands for the viscosity of component l, P_l indicates the pressure of component l, g is the gravitational acceleration, b indicates the Klinkenberg factor accounting for gas slippage effects, D_g is gas diffusivity coefficient, c_g stands for gas compressibility, K_R indicates thermal conductivity of the rock, K_w represents thermal conductivity of water, K_o represents thermal conductivity of oil, K_g represents thermal conductivity of gas, h_l stands for specific enthalpy of component l, $R_n^{l,t+1}$ denotes the residual of component l at time step $t+1$ in the grid block n, where superscript t represents time step and subscript n represents the grid block number, Δt stands for size of time step, V_n is volume of grid n, A_{nm} represents the common surface between grid n and grid m, $x_{i,p+1}$ stands for the primary variables, where subscript i denotes grid block number and p represents the iteration index, ε_1 stands for the relative convergence criterion.

2.2.2 Governing Equations for Geomechanics

For the geomechanics module, the quasi-static system is used, and the governing equation for force equilibrium can be expressed in terms of total stress as Eq. (13). By applying the small strain theory, the linearized strain tensor relationship is obtained as Eq. (15). To couple the flow and mechanics equations, a relationship between stress and strain need to be built (Biot 1941; Coussy 1995; Borja 2006). According to the formulas of Coussy (1995), the poroelasticity equations could be descried as Eq. (16) to (18). By inserting Eq. (17) into Eq. (13) and rewriting Eq. (16), the coupling equations for fluid flow and geomechanics system can be expressed as Eq. (19) and (20), which are for single-phase flow. With the presence of saturation and capillary pressure, the mass variation of each phase $dm/d\rho$ will be different for multi-phase flow. The volumetric strain ε_v is the bridge to couple the two primary variables displacement and pressure by Eq. (16), (17), and (21). More details about how to derive these equations can be found in the dissertations of Wan (2002) and Kim (2010).

$$\nabla\sigma + \rho_b g = 0 \tag{13}$$

$$\rho_b = \phi\rho_f + (1-\phi)\rho_s \tag{14}$$

$$\varepsilon_{ij} = \frac{1}{2}\left(\frac{\delta u_i}{\delta x_j} + \frac{\delta u_j}{\delta x_i}\right) \tag{15}$$

$$\frac{dm}{\rho_f} = \left(\phi c_f + \frac{\alpha-\phi}{K_s}\right)\frac{dP}{dt} + \alpha\frac{d\varepsilon_v}{dt} \tag{16}$$

$$\delta\sigma = C_{dr}\delta\varepsilon - \alpha\delta P\boldsymbol{I} \tag{17}$$

$$\alpha = 1 - \frac{K_d}{K_s} \tag{18}$$

$$\alpha \frac{d\varepsilon_v}{dt} + \left(\phi c_t + \frac{\alpha-\phi}{K_s}\right)\frac{dP}{dt} + \frac{dm}{\rho_f} = f \quad (19)$$

$$Div(C_{dr}\delta\varepsilon - \alpha\delta P\boldsymbol{I}) + \rho_b g = 0 \quad (20)$$

$$\varepsilon_v = \varepsilon_{xx} + \varepsilon_{yy} + \varepsilon_{zz} \quad (21)$$

$$\varepsilon = \frac{1}{3}\varepsilon_v \boldsymbol{I} + e \quad (22)$$

Where σ is total stress, ρ_b denotes bulk density, ρ_f represents fluid density, ρ_s stands for density of solid phase, ε denotes the linearized strain tensor, u is the displacement vector, where $i\ and\ j$ stand for displacement direction, c_f represents fluid compressibility, α is the Biot coefficient, K_s denotes the bulk modulus of the solid grain, ε_v represents the volumetric strain, f is the fluid source and sink term, C_{dr} stands for the rank-4 elasticity tensor, and $\boldsymbol{I}$ represents the rank-2 identity tensor, K_d stands for drained bulk modulus, ε_v represents the volumetric strain, and e is the deviatoric part of the strain tensor.

2.2.3 Governing Equations for Coupled Model

As we explained in the section above, the fixed-stress split scheme is chosen to be used for the coupled model in this study. Based on the fixed-stress approach, the rate of the total mean stress is assumed constant as on Eq. (23), and the full matrix inversion is not required for Eq. (19). Additionally, the constant rate of total mean stress can be used to derive the new strain relationship as on Eq. (24). This sequential coupled method is implemented by using the Galerkin Finite Element Method for the mechanics balance equations and the finite difference method for the mass balance equations, where fluid pressure (and saturation) and solid displacement are chosen as primary unknown variables.

For the finite difference method, the primary variables, such as fluid pressure, are assumed to be located at the center of grid block. For the finite element method, the displacement vector is computed in three directions at each node of grid block. Therefore, for a grid block on two-dimensional mesh domain, there are one pressure (and saturation) variable and eight displacement variables.

By multiplying the weighting function with Eq. (20), the weak form for Finite Element Method is firstly obtained as Eq. on (25). Then the standard Galerkin procedures are applied to discrete the weak form, which leads to a system of linear equilibrium equations for each grid block as on Eq. (26). By assembling the stiffness matrix and displacement vector of each grid block together, a global equation for displacement is reached as on Eq. (27). After the discretization on time and space, the final coupled equations for fluid flow and geomechanics are presented as Eq. (28) and (29), which is an example for one-dimensional single-phase flow-geomechanics system. The gravity force was ignored and the fluid properties were stress-dependent for the derivation of these equations. Eq. (28) represents the mechanics balance, and Eq. (29) stands for the fluid mass balance. Both equations include the primary variables, pressure and displacement.

$$\delta\dot{\sigma_v} = 0 \tag{23}$$

$$\Delta\varepsilon^n = \frac{\alpha}{K_d}(\Delta P^n - \Delta P^{n-1}) + \Delta\varepsilon^{n-1} \tag{24}$$

$$\int_\Omega w \cdot (\nabla(C_{dr}\delta\varepsilon - \alpha\delta P\boldsymbol{I}) + \rho_b g)d\Omega = 0 \tag{25}$$

$$K_{grid}u_{grid} = F_{grid} \tag{26}$$

$$K_{global}u_{global} = F_{global} \tag{27}$$

$$k_d\left(-\frac{1}{\Delta x}u_{i-1}^{n+1}+2\frac{1}{\Delta x}u_i^{n+1}-\frac{1}{\Delta x}u_{i+1}^{n+1}\right)-\alpha(P_{e-1}^{n+1}-P_e^{n+1})=0 \quad (28)$$

$$\left(\phi c_f+\frac{\alpha-\phi}{K_s}+\frac{\alpha^2}{k_d}\right)\frac{P_e^{n+1}-P_e^n}{\Delta t}\Delta x-\frac{\alpha^2}{k_d}\frac{P_e^n-P_e^{n-1}}{\Delta t}\Delta x+\frac{\alpha}{\Delta t}\Big((-u_i^n+u_{i+1}^n)-(-u_i^{n-1}+$$

$$u_{i+1}^{n-1})\Big)-\left(\frac{k}{\mu}\frac{P_{e-1}^{n+1}-2P_e^{n+1}+P_{e+1}^{n+1}}{\Delta x}\right)=0 \quad (29)$$

Where σ_v represents the total mean stress, K_{grid} stands for the local stiffness matrix for each grid block, u_{grid} denotes the local displacement vector for each grid block, F_{grid} represents the local force vector for each grid block, K_{global} stands for the global stiffness matrix for entire mesh, u_{global} denotes the global displacement vector for entire mesh, F_{grid} represents the global force vector for entire mesh, k_d denotes drained bulk modulus, the superscript $n-1, n, and\ n+1$ denote time step, the subscript $i-1, i, and\ i+1$ represent displacement node number, and the subscript $e-1\ and\ e$ mean the grid block number.

The schematic of fully coupled and iteratively coupled method for single-phase fluid and mechanics is shown on Fig. 6, where P represents fluid pressure, u stands for displacement of reservoir rock, the superscript n and $n+1$ denotes time step. For the fully coupled scheme, the large nonlinear equations system of flow and mechanics are solved simultaneously, where pressure and displacement are solved together at each time step. In other words, Eq. (28) and Eq. (29) are solved together as one large matrix for each time step. Based on the iteratively (sequential) coupled method with the fixed-stress split approach, the flow mass balance Eq. (29) is firstly solved for the pressure variable. Based on the just solved pressure, the momentum balance Eq. (28) is then solved for the displacement variables. There are two separate calculations for each time step. The

obtained values of pressures and displacements at current time step will be delivered to next time step, where the same calculations will be repeated. More details about a general system of coupled equations using the fixed-stress split method can be found in Kim (2010). In addition, since the change of pore volume, volumetric strain, and stress change have been calculated in the coupled model, reservoir properties, such as porosity and permeability, can be updated based on the observed laboratory or field data and reservoir condition.

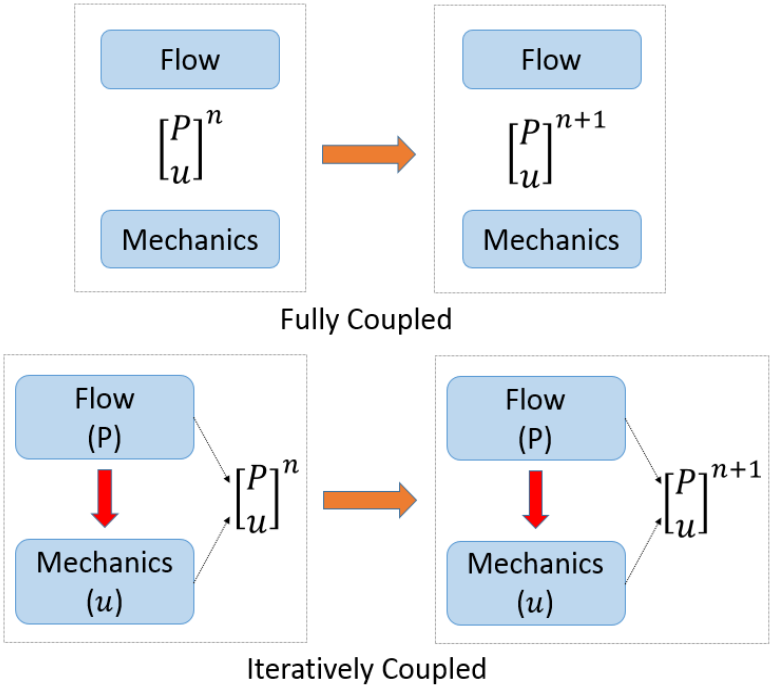

Figure 6: Schematic of fully coupled and iteratively coupled method for fluid flow and mechanics.

2.3 Coupled Model Validation

2.3.1 The Terzaghi Problem

The Terzaghi's consolidation problem is often used to verify the accuracy of the coupled model. The typical problem was formulated by Terzaghi (1925) to analyze the pressure and displacement distribution when compressing clay layers. The schematic of one dimensional Terzaghi problem is shown on Fig. 7, where a constant stress is loaded on the top surface of the sample. The top surface is regarded as drainage boundary with displacement change, while there are no flow and displacement change on the bottom surface of the sample. Additionally, no flow and no displacement occur on the both sides of the sample. The analytical solution of this one-dimensional (1D) Terzaghi consolidation problem can be found from many literature (Kim, 2000; Verruijt, 2013), while the different initial condition should be specified when applying it. The equations of analytical solution used in this study are displayed as on Eq. (30) and Eq. (31).

$$\frac{P}{P_i} = \frac{4}{\pi}\sum_{k=1}^{\infty}\frac{(-1)^{k-1}}{2k-1} cos\left[\frac{(2k-1)\pi}{2}\frac{z}{h}\right] exp\left[-\left(\frac{(2k-1)\pi}{2}\right)^2 \frac{c_v t}{h^2}\right] \tag{30}$$

$$c_v = \frac{k}{\mu(\phi c_f + b^2/K)} \tag{31}$$

Where, P denotes pressure, P_i represents initial pressure, z stands for the sample hight from the bottom, h is the total hight of the sample, c_v denotes the consolidation coefficient, t represents time, k stands for permeability, μ is fluid viscosity, ϕ denotes sample porosity, c_f represents fluid compressibility, b stands for Biot's number, K is compression modulus of sample.

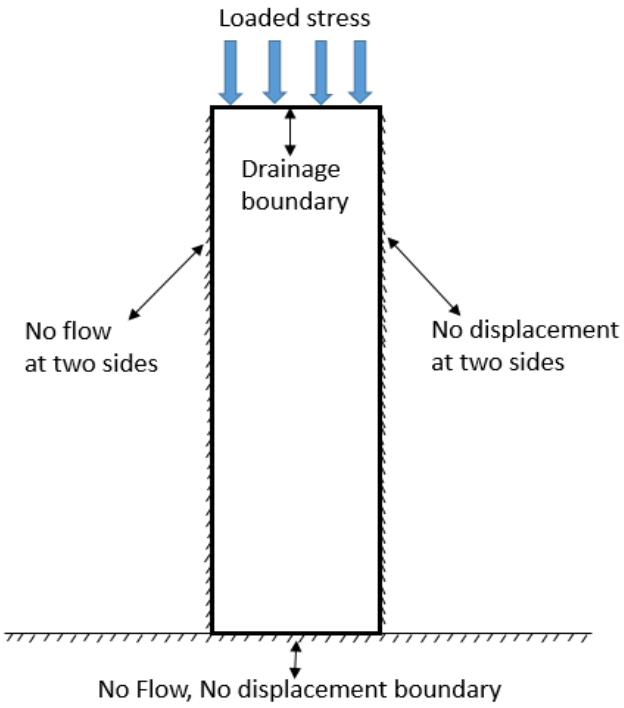

Figure 7: Schematic of Terzaghi's problem.

The fully coupled model and the sequential coupled model are separately built for the Terzaghi's problem, and their results are compared with the analytical solution. The initial condition of this one-dimensional Terzaghi problem is shown on Table (1), where all symbols uses the standard internationally units and the Biot coefficient is assumed to one. By applying Eq. (30) and (31) with the initial conditions above, the analytical solution can be obtained. The results about pressure distributions along with the sample height are presented on Fig. 8, where x axis is normalized pressure and y axis is normalized sample depth. In addition to analytical solution, two different numerical schemes are conducted: fully coupled method and sequential coupled method.

It should be highlighted that the sequential coupled method is what we apply in this study, which is also what we want to validate in here. The reasons we show the results

from the fully coupled method are: a) the fully coupled model provides true solution which is great for validation; b) it is much easier to build and solve the 1D fully coupled model by numerical method and programming. Two different simulation times are selected to express the results from the coupled models: $t1 = 1.5 \times 10^5\ (s), t2 = 2.5 \times 10^5\ (s)$. The numerical results of sequential coupled method is perfectly matched with the analytical solution and the results of the fully coupled method on both selected times, which validates the accuracy of this sequential coupled method.

Table 1: Input parameters for the Terzaghi consolidation problem.

Parameters	**Value**		**Parameters**	**Value**
Porosity	0.25		Time (s)	$1.5/2.5 \times 10^5$
Biot coefficient	1		Timestep (s)	5
Permeability (m^2)	4.935×10^{-14}		Grid size (m)	1
Viscosity ($Pa \cdot s$)	1×10^{-3}		Sample height (m)	50
Initial pressure (Pa)	0		Loaded stress (Pa)	2×10^6
Fluid compressibility (1/Pa)	4×10^{-10}		Sample compression modulus (Pa)	1×10^8

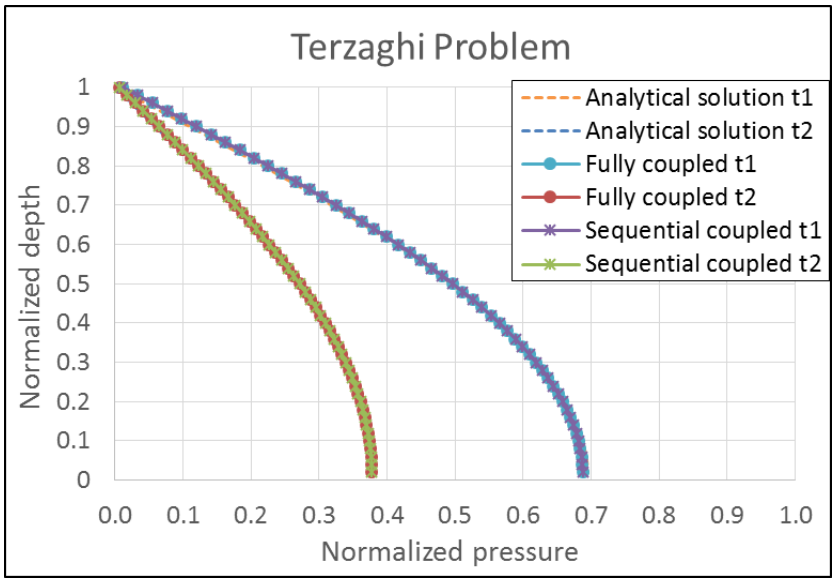

Figure 8: Results of pressure distributions for Terzaghi's problem.

2.3.2 The Mandel Problem

With the analytical solution provided by Mandel (1953), Mandel's consolidation problem has been extensively widely used to validate the coupled flow-geomechanics model. Fig. 9 shows the schematic of original Mandel's problem. An infinitely long rectangular sample is subjected between two rigid, frictionless and impermeable plates. The deformation of the sample is constrained to be plane strain condition, which means no deformation in the direction perpendicular to the plane. At time $t = 0^+$, a uniform vertical stress is applied on the top and bottom of the sample. Skempton (1954) predicted a uniform pore pressure increase can be detected among the entire sample at the instant of loading stress. Since the two side boundaries are open to the ambient pressure, drainage process will occur at that two side boundaries, and the pore pressure will be gradually decreased to the ambient pressure. Due to the geometrical symmetry of the sample, only

an upper-right quarter of the domain is chosen as the computation domain in this poroelasticity model for simplicity. As Fig. 10 shows, no horizontal displacements occur on the left boundary, and no vertical displacement occurs on the bottom boundary. With the constant loaded stress on the top boundary, the pore fluid will only drain out from the right-hand side boundary.

The original Mandel's solution (1953) only provided the analytical formulation for pore pressure, while both the fluid and solid particles are considered incompressible. Cheng and Detournay (1988) and Abousleiman et al. (1996) expanded the analytical solution to the more general cases with compressible pore fluid and compressible solid constituents, as well as transversely isotropic materials. Based on these references, the equations of analytical solutions for Mandel's problem are showed from Eq. (32) to Eq. (40).

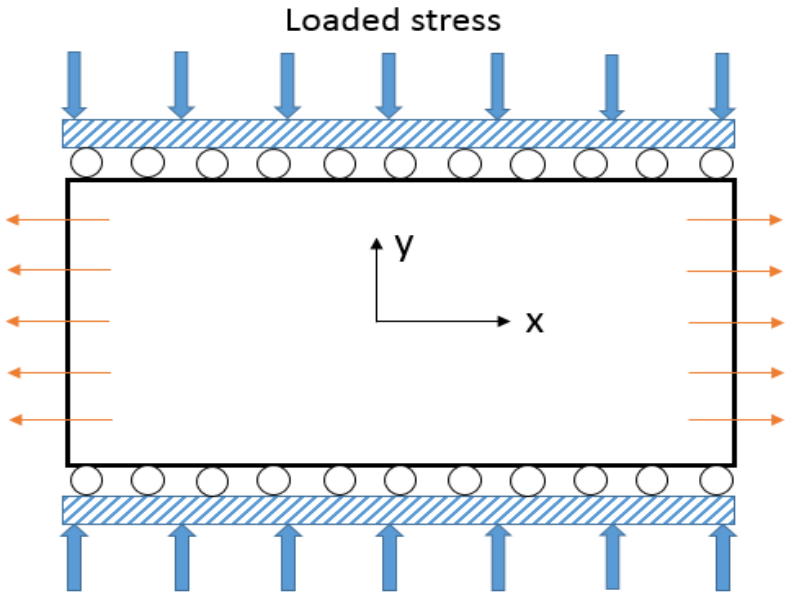

Figure 9: Schematic of original Mandel's problem.

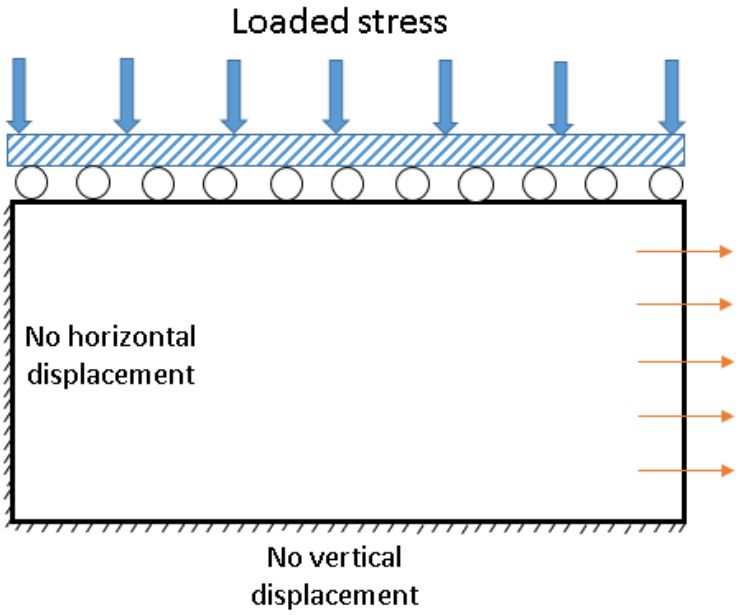

Figure 10: Schematic of simplified domain for Mandel's problem.

$$p = \frac{2FB(1+v_u)}{3a}\sum_{i=1}^{\infty}\frac{sin\beta_i}{\beta_i - sin\beta_i cos\beta_i}\left(cos\frac{\beta_i x}{a} - cos\beta_i\right)\exp\left(-\beta_i^2\frac{c_v t}{a^2}\right) \tag{32}$$

$$u_x = \left[\frac{Fv}{2Ga} - \frac{Fv_u}{Ga}\sum_{i=1}^{\infty}\frac{sin\beta_i cos\beta_i}{\beta_i - sin\beta_i cos\beta_i}\exp\left(-\beta_i^2\frac{c_v t}{a^2}\right)\right]x +$$

$$\frac{F}{G}\sum_{i=1}^{\infty}\frac{cos\beta_i}{\beta_i - sin\beta_i cos\beta_i}sin\frac{\beta_i x}{a}\exp\left(-\beta_i^2\frac{c_v t}{a^2}\right) \tag{33}$$

$$u_y = \left[-\frac{F(1-v)}{2Ga} + \frac{F(1-v_u)}{Ga}\sum_{i=1}^{\infty}\frac{sin\beta_i cos\beta_i}{\beta_i - sin\beta_i cos\beta_i}\exp\left(-\beta_i^2\frac{c_v t}{a^2}\right)\right]y \tag{34}$$

$$B = 1 - \frac{\phi K(K_s - K_f)}{K_f(K_s - K) + \phi K(K_s - K_f)} \tag{35}$$

$$v_u = \frac{3v + B(1-2v)(1-K/K_s)}{3 - B(1-2v)(1-K/K_s)} \tag{36}$$

$$c_v = \frac{2k_f B^2 G(1-v)(1+v_u)^2}{9u_f(1-v_u)(v_u - v)} \tag{37}$$

$$G = \frac{E}{2(1+v)} \tag{38}$$

$$tan\beta_i = \frac{1-v}{v_u-v}\beta_i \tag{39}$$

$$p_i(0^+) = \frac{BF(1+v_u)}{3a} \tag{40}$$

Where, p is pore pressure, F is loaded stress, B is Skempton's pore pressure coefficient which is the ratio of induced pore pressure to variation of confining pressure under undrained conditions, v_u is undrained Poisson's ratio, v is drained Poisson's ratio, a is sample length, β_i is the roots of equation (39), K is bulk modulus of the solid skeleton, K_s is the bulk modulus of the solid grains, K_f is bulk modulus of the pore fluid, ϕ is media porosity, t is time, G is shear modulus, E is Young's modulus, k_f is media permeability, u_f is pore fluid viscosity, u_x is displacement in horizontal direction, u_y is displacement in vertical direction, x is horizontal coordinate, y is vertical coordinate, $p_i(0^+)$ is the initial induced pore pressure at the instant of loading, which is used to calculate the normalized pressure $p/p_i(0^+)$.

Table 2 displays the main input parameters of Mandel's problem for the coupled flow-geomechanics model, where all symbols use the standard internationally units. With the initial conditions above, the analytical solution can be obtained by applying Eq. (32) to (40). Fig. 11 presents the pore pressure results about the comparisons between numerical simulation and analytical solution. The x axis is normalized length, which is the ratio of horizontal coordinate to the total sample length of Fig. 10. The y axis is normalized pressure, which is the ratio of pore pressure to the initial induced pressure $p_i(0^+)$. On Fig. 11, the legend 'analytical' stands for analytical solution, and the legend 'simulation' represents the numerical simulation results from the coupled model. Two different

simulation times are selected for the Mandel problem: 1×10^4 (s) and 2×10^4 (s). The simulation results show a great agreement with analytical solution on both model times, which again verifies the accuracy of the coupled flow-geomechanics model.

On the other hand, the Mandel-Cryer effect has been demonstrated and validated for the sequential coupled model on Fig. 12. The central point on Fig. 9 was chosen to monitor the pressure change along with time. The Mandel-Cryer effect, where the pore pressure increases beyond the initial value (predicted by the Skempton effect) and then decreases after a sudden stress load on the domain boundary, has been well documented on both numerically and experimentally (Cryer 1963; Gibson et al. 1963). Since the diffusion solution is characterized by a monotonic decline of pore pressure, the Mandel-Cryer effect is a unique phenomenon to demonstrate and validate the poroelastic theory for the coupled model. On Fig. 12, the results from coupled simulation are matched well with the analytical solution, which validates the accuracy of the sequential coupled method we used. Overall, the accuracy of the sequential coupled model has been validated by comparing with the analytical solution of the Terzaghi problem and Mandel problem. In other words, the flow process through porous media under compaction stress has been proved, which provides us more confidence to apply the developed sequential coupled model as a solid modeling tool for various reservoir applications in the next chapters.

Table 2: Input parameters for Mandel's problem.

Parameters	Value		Parameters	Value
Porosity	0.25		Sample length (m)	50
Permeability (m^2)	4.935×10^{-14}		Sample hight (m)	0.01
Viscosity $(Pa \cdot s)$	1×10^{-3}		Poisson's ratio	0
Fluid compressibility $(1/Pa)$	4×10^{-10}		Young's modulus (Pa)	2×10^{9}
Initial pressure (Pa)	0		Loaded stress (Pa)	1×10^{6}

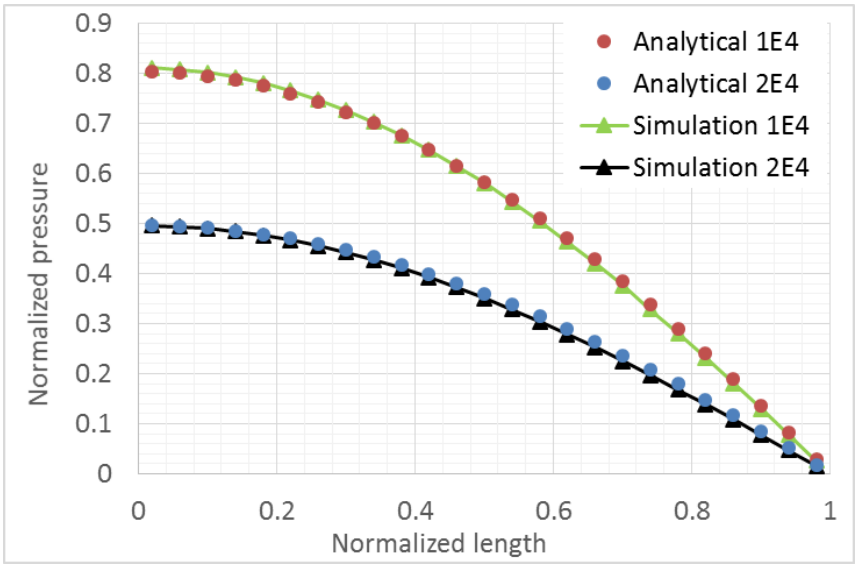

Figure 11: Comparisons between numerical results and analytical solution: normalized pressure versus normalized length.

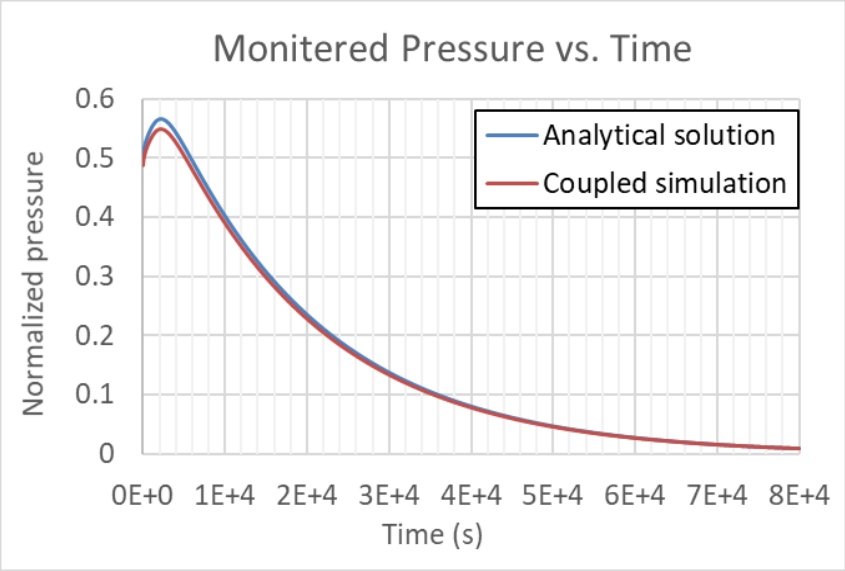

Figure 12: Mandel-Cryer effect in the coupled model.

CHAPTER III

STRESS-DEPENDENT PERMEABILITY CORRELATIONS*

3.1 Introduction

Effective stress is gradually increased and permeability is gradually reduced during reservoir depletion caused by hydrocarbon production, while the organic-rich matrix might experience a shrinkage process that will boost the permeability. The main objective of this chapter is to apply the developed coupled model for investigating the effects of different stress-dependent permeability correlations and matrix shrinkage on permeability change and production performance for organic-rich shale gas reservoirs.

Coalbed methane is stored as adsorbed gas on the internal surface area of the microporous coal. During the reservoir depletion and the decrease of reservoir pressure, two physics processes will occur and affect the reservoir permeability for coal beds: a) the increase of effective stress under uniaxial stain condition; b) the coal matrix shrinkage caused by gas desorption. However, this two phenomenon bring inverse impacts to reservoir permeability. The increase of effective stress will decrease the rock permeability, but the shrinkage of coal matrix could increase the apertures of surrounding fracture network and enhance the permeability. Fig. 13 presents a conceptual schematic of matrix shrinkage, where the left part is for before shrinkage, and the right part is for after

* Part of data reported in this chapter is reprinted with permission from "Stress-dependent Permeability of Organic-rich Shale Reservoirs: Impacts of Stress Changes and Matrix Shrinkage" by An, C., Killough, J., Mi, L., 2019. Journal of Petroleum Science and Engineering, Volume 172, Pages 1034-1047, Copyright 2019 by Elsevier.

shrinkage. After the matrix shrinkage, the volume of matrix (blue grid) decreases, and the volume (width) of surrounding fractures increases. A number of researchers have already studied the effect of coal matrix shrinkage on cleat permeability, where different correlations between stress change and permeability change are proposed to describe this phenomenon (Gray 1987; Durucan and Edwards 1986; Seidle and Huitt 1995; Palmer and Mansoori 1996; Shi and Durucan 2004; Connell 2009; Liu and Harpalani 2013).

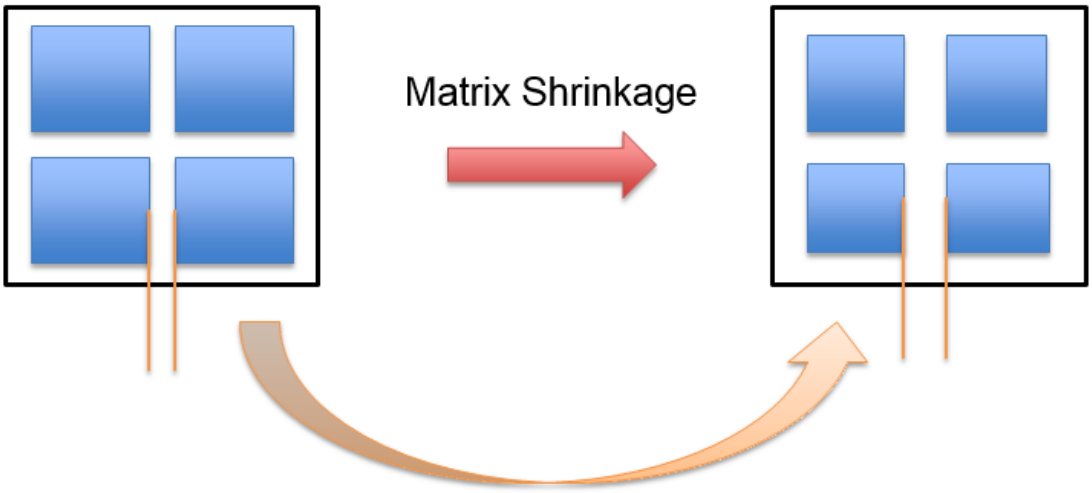

Figure 13: A conceptual schematic of matrix shrinkage.

Since gas desorption from organic matter is similar with the process of coalbed matrix shrinkage and the organic matter is also soft material like coal matrix, we will apply both the shrinkage process and correlations of coal shrinkage for the organic matter of shale gas reservoirs. In other words, when certain amount of gas desorb from organic matter, we assume the matrix volume of organic matter will shrink, which in return leads to a volume (width) increase of surrounding natural fractures. Due to the shrinkage only

affects the permeability of the natural fractures around the organic matters (not for all natural fractures network), the permeability change caused by matrix shrinkage will be only added to the organic matter grid blocks (not to the natural fracture blocks) in our reservoir model. This approach is different with the original coal matrix shrinkage. For coal bed reservoir, the entire matrix will shrink at the same time because of its typical dual porosity structure. However, the shrinkage process is only considered for the organic matter in the organic-rich shale gas reservoir in our reservoir model.

In the study of this chapter, the reservoir matrix is divided into three different sub-pore media: non-organic matter, organic matter, and natural fractures. Based on the different media properties and flow mechanisms, various stress-permeability correlations are separately applied to these three different porous medium. Furthermore, matrix shrinkage is considered only for organic matter because of gas desorption. The structure for the rest of this chapter is organized as follows. Firstly, the stress-dependent permeability correlation for each sub-porous medium is introduced and explained in details. Secondly, with considering different stress-dependent permeability correlations and matrix shrinkage, a micro two-dimensional reservoir model is built to display the gas flow process and cumulative production. Thirdly, the sensitivity analyses are investigated for Total Organic Carbon (TOC), matrix permeability, Young's modulus, Poisson's ratio, and bottom hole pressure. Finally, some conclusions and discussions are provided to summarize this study.

3.2 Stress-dependent Permeability Correlations

Non-organic matter, organic matter, and natural fractures are three major components in shale reservoir. In order to better describe the permeability change along with the pressure change, the shale matrix is divided into the three different pores media. In addition, based on different media properties and behaviors under compression, dissimilar permeability correlations are separately applied to the three pores media. To be noted, matrix shrinkage is only applied to organic matter. The correlation mechanism and equations for each pore medium will be explained in details as follows.

3.2.1 Non-organic Matter

Non-organic matter is the major component in the shale gas reservoirs, and they typically exhibit low porosity and extra-low permeability. Additionally, for non-organic matter, the dependence of hydraulic properties (mainly porosity and permeability) on stress change is not as strong as the fractures (natural fractures and hydraulic fractures) and organic matter. Davies and Davies (1999) identified cemented sandstone reservoirs into three different rock types and they proposed different stress dependent permeability equations for each type. Based on their laboratory data and curve match, the rock with tiny pore diameter belongs to rock type three, where porosity is related to the mean effective stress and permeability is correlated to the porosity change, as on following Eq. (41) and (42). In the study of this chapter, these two equations are applied to describe the stress dependent permeability relationship for the non-organic matter. The parameters values of a, c, and ϕ_r are adapted from Rutqvist et al. (2002), which are shown on Table (3). Some

main parameters of the stress-dependent permeability correlations are shown for the sub-pore media (non-organic matter, organic matter, and natural fractures) on Table (3).

It should be noted that the porosity change is supposed to be calculated based on the change of displacement and volumetric strain on each grid block for the coupled flow-geomechanics model. However, since we need to use the empirical Eq. (42) to calculate the change of permeability for non-organic matter, we decided to apply the Eq. (41) for the porosity change, instead of the mathematical equation from the coupled method. By applying this approach, no issues have been observed for the coupled model in terms of stability and convergence. Fig. 14 shows one example of the permeability reduction along with the decreased pressure for non-organic matter, where x axis is reservoir pressure, and y axis is normalized permeability. When the pressure is reduced from 3000 psi to 500 psi, the permeability is reduced into about 40% of the initial value.

$$\phi = \phi_r + (\phi_i - \phi_r)e^{(a\sigma'_m)} \tag{41}$$

$$k = k_i e^{-c\left(1-\frac{\phi}{\phi_i}\right)} \tag{42}$$

Where ϕ is the media porosity, ϕ_r is the residual porosity at high stress, ϕ_i is the initial porosity, $a\ and\ c$ are the media properties determined by laboratory measurements, σ'_m is the mean effective stress, k is the media permeability, k_i is the initial permeability.

Table 3: Main parameters of stress-dependent permeability correlations for sub-pore media.

Sub-pore media	Parameter	Value
Non-organic Matter	$\alpha\ (1/pa)$	5×10^{-8}
	c	2.22
	ϕ_r	0.01
Organic Matter	$c_f\ (1/pa)$	2.9×10^{-5}
	ε_l	5.06×10^{-2}
	$p_\varepsilon\ (pa)$	7.0×10^{6}
Natural Fractures	$b\ (1/pa)$	1.5×10^{-7}

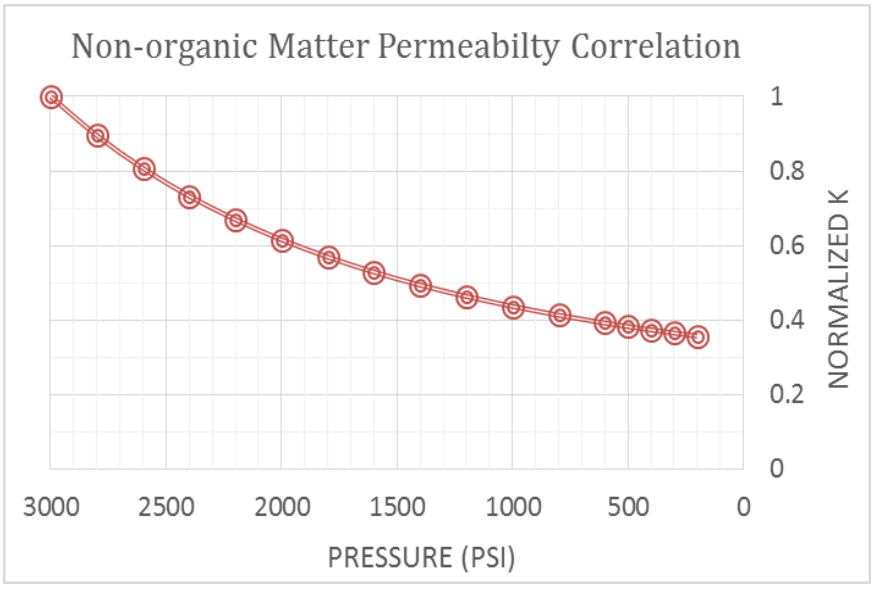

Figure 14: The correlation of normalized permeability versus pressure for non-organic matter.

3.2.2 Organic Matter

Organic matter is quite common in shale gas reservoirs, and the content of organic matter is often expressed as Total Organic Carbon (TOC). Organic matter is different with non-organic matter in shale reservoir, because it could be both source rock and porous media for hydrocarbon. In other words, methane is stored not only as free gas but also as adsorbed gas in organic matter. When the pressure drop below a certain value, gas will start to be desorbed from kerogen surface and become free gas. Consequently, organic matter plays important roles in terms of petrophysical properties, hydrocarbon reserve, and gas flow mechanisms. Typically, a higher TOC brings a larger gas adsorption or desorption capacity. The process of shale gas desorption is quite similar with the desorption of methane in coalbed. Organic matter is also soft material as coal. Therefore, researchers have proposed to apply the shrinkage permeability model of coal beds for describing the permeability change of organic matter.

When methane is desorbed and produced from the coal, the coal pressure is reduced. The reduced pressure will result in two aspects of influence on permeability. On one hand, the reduced pore pressure brings an increase of net effective stress, which will compress rock to decreases its permeability. On the other hand, the decreased coal pressure could lead the volume of coal matrix to reduce in size because of gas desorption, which is called matrix shrinkage. As we described on Fig. 13 above, the volume shrinkage mainly occurs at coal matrix, and it does not happen to fracture network. As a result, the fracture's width is enlarged, and its permeability is increased. Seidle and Huitt (1995) conducted experimental measurements to investigate the coal matrix shrinkage and

permeability increase caused by gas desorption. They derived the equations relating the matrix shrinkage, porosity, and permeability by using a matchstick geometry model. Later on, Palmer and Mansoori (1998), Gilman and Beckie (2000), and Shi and Durucan (2002) have also developed various relationships to describe the matrix shrinkage and the change of porosity and permeability along with pressure. Table (4) displays main equations and some important notes for the relationships above. More details about these equations and their applications can be found in their papers.

Table 4: Four main coal permeability relationships related to matrix shrinkage.

Authors	Equations	Notes
Seidle and Huitt (1995)	$\frac{\phi}{\phi_i} = 1 + \left(1 + \frac{2}{\phi_i}\right) C_m 10^{-6} V_L \left(\frac{p_i}{p_L + p_i} - \frac{p}{p_L + p}\right)$ $\frac{k}{k_i} = \left(\frac{\phi}{\phi_i}\right)^3$	Matrix shrinkage proportional to the amount of desorbed gas; A matchstick geometry
Palmer and Mansoori (1998)	$\frac{\phi}{\phi_i} = 1 + \frac{c_m}{\phi_i}(p - p_i) + \frac{\varepsilon_l}{\phi_i}\left(\frac{K}{M} - 1\right)\left(\frac{\beta p}{1 + \beta p} - \frac{\beta p_i}{1 + \beta p_i}\right)$ $\frac{k}{k_i} = \left(\frac{\phi}{\phi_i}\right)^3$	Appropriate for uniaxial strain condition
Gilman and Beckie (2000)	$k = k_i \exp\left(\frac{3v}{1 - v}\frac{\Delta p}{E_F}\right) \exp\left(-\frac{3\alpha E}{1 - v}\frac{\Delta S}{E_F}\right)$	Dual porosity system; E_F is Young's modulus of fracture
Shi and Durucan (2002)	$k = k_i e^{-3c_f \Delta\sigma}$ $\Delta\sigma = -\frac{v}{1 - v}(p - p_i) + \frac{E}{3(1 - v)}\varepsilon_l \left(\frac{p}{p + p_\varepsilon} - \frac{p_i}{p_i + p_\varepsilon}\right)$	Stronger matrix shrinkage and permeability rebound

In the study of this chapter, the mathematical model of Shi and Durucan (2002) is chosen to calculate the variation of permeability for organic matter. The main equations are shown on Eq. (43) to Eq. (45). There are mainly three reasons why the mathematical model of Shi and Durucan was chosen. Firstly, the model has been validated by comparing the results with the published pore pressure dependent permeability changes from the coalbeds methane wells in the San Juan basin. Many other's models have not been history-matched with field production data. Secondly, an obvious permeability rebound with pressure drawdown has been observed in the San Juan basin, which was well predicted by the model and was exactly what we expect for organic matter. Thirdly, the volumetric matrix shrinkage in this model is proportional to the volume of desorbed gas, rather than to the reduction of equivalent sorption pressure, which we believe could better represent the process of gas desorption and matrix shrinkage. On the right hand side of Eq. (44), the first term stands for normal change of effective stress, and the second term represents the change of effective stress due to gas desorption. In other words, only when the pressure is below the critical desorption pressure, the second term will come into effect.

By using the Langmuir equation, the volumetric matrix shrinkage strain ε_s is related to pressure as shown on Eq. (45). On Eq. (43) to (45), the values of coefficient $c_f, \varepsilon_l, p_\varepsilon$ are selected based on Shi and Durucan (2002), which are shown on Table (3). ε_l is regarded as the maximum volumetric strain when the coal is fully saturated with gas, and p_ε is the pressure when the matrix strain is equal to half of ε_l. Fig. 15 presents one example of organic matter permeability correlation curves for two different values of ε_l, where the other parameters are kept constant. On the vertical axis of Fig. 15, the

normalized permeability is the ratio of permeability over initial permeability. When the pressure decreases from 3000 to 1000 psi, the permeability significantly reduces for both curves. However, for the curve with large value of ε_l (5.06×10^{-2}), the permeability starts to rebound at the low-pressure range, where the matrix shrinkage dominates the change of permeability. For the curve with small value of ε_l, the permeability rebound is not obvious. Therefore, the input value of ε_l plays a significant important role on the impact of matrix shrinkage on permeability change and that if the impact is large enough to be observed. The input value of ε_l should be obtained based on experimental measurement data.

$$k = k_i e^{-3c_f \Delta\sigma} \tag{43}$$

$$\Delta\sigma = -\frac{v}{1-v}(p - p_i) + \frac{E}{3(1-v)}\varepsilon_l \left(\frac{p}{p+p_\varepsilon} - \frac{p_i}{p_i+p_\varepsilon}\right) \tag{44}$$

$$\varepsilon_s = \frac{\varepsilon_l p}{p+p_\varepsilon} \tag{45}$$

Where, k is media permeability, k_i is initial media permeability, c_f is media compressibility which is usually obtained by fitting the correlation curve with laboratory test data, $\Delta\sigma$ is the change of effective stress, v is Poisson's ratio, p is media pressure, p_i is the initial media pressure, E is Young's modulus, $\varepsilon_l \, and \, p_\varepsilon$ are referred as the Langmuir-type organic matter shrinkage constants, ε_s is the macroscopic volumetric matrix shrinkage strain.

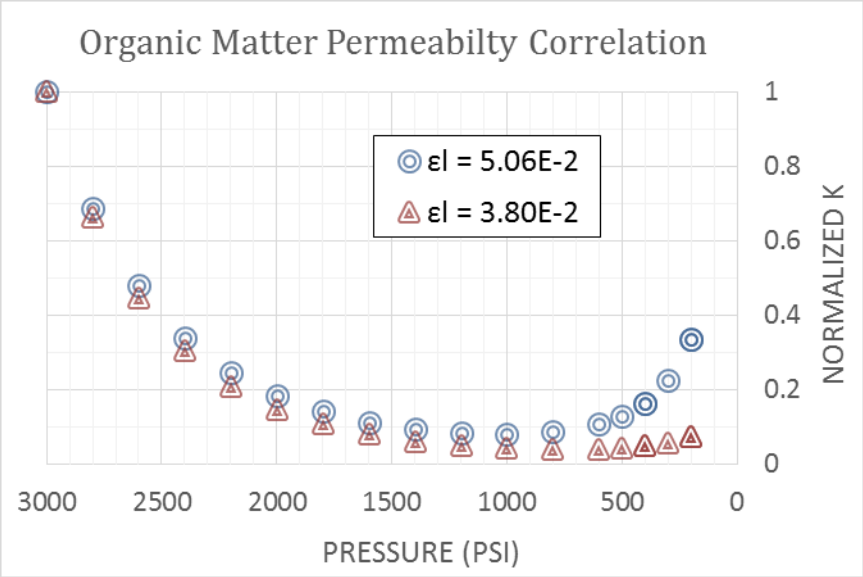

Figure 15: The correlations of normalized permeability versus pressure for organic matter.

3.2.3 Natural Fractures

Gale et al. (2014) have investigated many shale core samples and images logs, and they found natural fractures are widely existed in shale reservoirs. By interacting with hydraulic fracture treatments and creating a complex fracture network, natural fractures are regarded as one important factor to enhance the overall permeability and production performance (Mi et al. 2016; An et al. 2017c). When reservoir is continuously being depleted, the reservoir pressure including natural fractures pressure is reduced. With the constant overburden stress, the net effective stress is increased. The larger net effective stress will compress the fracture to reduce its aperture and conductivity.

Many different pressure-dependent correlations for natural fractures could be found from the literature, while we choose to use the correlation model proposed by Raghavan and Chin (2004) for the natural fractures in the study of this chapter, where the

main equation is shown as on Eq. (46). There are two main reasons why we chose the correlation model from Raghavan and Chin. Firstly, Gutierrez et al. (2000) presented the laboratory results about the hydro-mechanical behavior of an extensional fracture in shale. Their measured data was fitted with an equation form, which is exactly the same with the correlation model proposed by Raghavan and Chin. Secondly, Cho et al. (2013) have conducted experimental studies and validated the relationship of Eq. (46) with their experimental data for unconventional reservoirs.

$$k_f = k_{fi} \times e^{-b\sigma'_m} \tag{46}$$

Where k_f is the natural fracture permeability, k_{fi} is the permeability at zero effective stress ($\sigma'_m = 0$), b is the rock characteristic parameter, σ'_m is the effective mean stress and a positive value represents rock compaction.

The coefficient b could be evaluated by fitting the correlation curve with the experimental data. Adapted from Gutierrez et al. (2000), the default value of b we will use in this chapter is 1.5×10^{-7} as shown on Table (3). Fig. 16 presents the natural fracture permeability correlation curves for two different values of coefficient b, where x axis is pressure and y axis is normalized permeability. For the curve with the default value of $b = 1.5 \times 10^{-7}$, the permeability is reduced into about 12% of initial permeability when the pressure is reduced from 3000 to 1000 psi. Comparing this two curves, the permeability reduction is much severer with a large value of b. Therefore, the coefficient b is extremely critical to determine how much the permeability will change along with the change of pressure. To choose an approximate value of b highly governs the impacts of pressure-dependent natural fracture permeability on shale gas production performance.

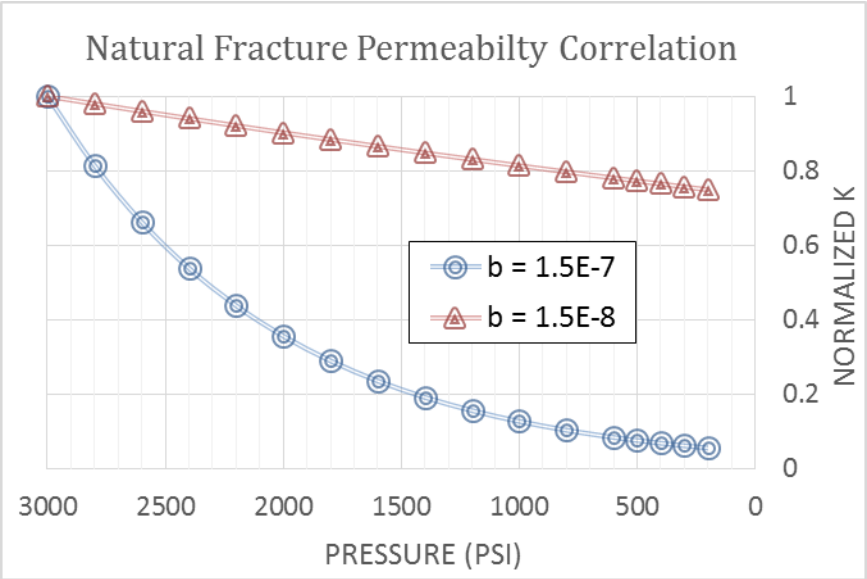

Figure 16: The correlation of normalized permeability versus pressure for natural fractures.

3.3 Numerical Simulation Results

Hydraulic fracturing treatments are always required to increase overall productivity and economically produce shale gas from extra-low permeability shale reservoirs. Due to various rock properties and the interaction between hydraulic fractures and natural fractures, a complex fracture network is usually created, which can be typically observed from microseismic mapping data. On left image of Fig. 17, an example of multi-stages hydraulic fractured network with one horizontal well is displayed. Due to extra-low permeability, stimulated reservoir volume (SRV) is the major area for gas production, and the shale matrix outside of SRV does not contribute much for production in first few years. Therefore, we only focuses on stimulated reservoir volume for shale gas flow simulation in the study of this chapter. On the other hand, due to the geometrical symmetry, partial SRV including only one hydraulic fracture is selected for reservoir simulation, which

could also save computational time. To better describe the stress-dependent permeability correlations and investigate the impacts of each sub-pore media on gas production, the reservoir mesh is divided into four different sub-pore media: non-organic matter, organic matter, natural fractures, and hydraulic fractures.

As on right image of Fig. 17, the central red block represents the producing well, the vertical gray grids stand for hydraulic fracture blocks, the green grids indicate natural fracture blocks, the white grids represent non-organic matter, and the blue grids stand for organic matter. Different stress-permeability correlations introduced on the above section are separately applied to each of sub-pore media: non-organic matter, organic matter, and natural fractures. For hydraulic fracture grids, we assume their permeability is stress-independent. There are three reasons about why we assume the permeability is constant for hydraulic fractures in our model. Firstly, hydraulic fractures have significantly larger permeability than natural fractures and shale matrix grids. Secondly, proppants can support the aperture of hydraulic fracture and maintain the permeability to a great extent. Thirdly, even though the aperture of hydraulic fracture is compressed by the increased effective stress, the permeability is still large enough to transfer all the gas from natural fracture and matrix grids into wellbore. In other words, hydraulic fracture is not the restraint factor in terms of overall flow performance when comparing with natural fractures and shale matrix.

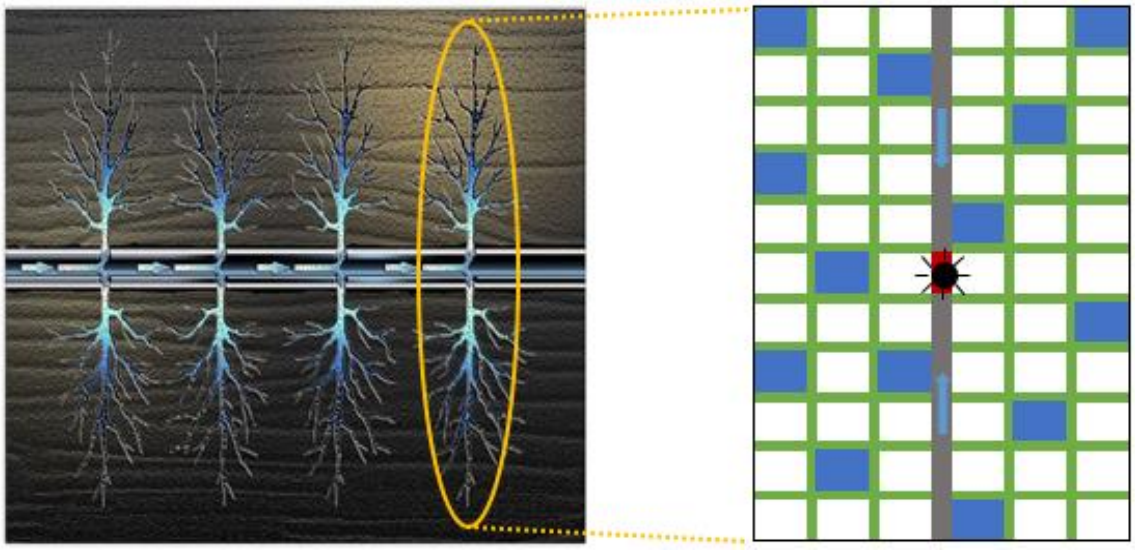

Figure 17: Mesh grid design for complex fracture network (the left image is adopted from FracFocus).

According to the governing equations introduced on the sections above, the coupled flow-geomechanics system can be solved along with producing time. At each time step, the flow equations are firstly solved for the primary variable pressure, and then the mechanics equations are solved for the displacements on each node. Next, the change of porosity and permeability are updated at each time step by the stress-dependent permeability correlations introduced on the section above. The mesh dimension of the synthetic reservoir model is $21(vertical) \times 11(horizontal) \times 1$. The domain length of horizontal direction is 6.09 meter, and the domain length of vertical direction is 11.1 meter. The size for the natural fracture, shale matrix including organic and non-organic matter, and hydraulic fracture grid are separately 0.01, 1.0, 0.05 meter. The reservoir mesh is built based on the structure (stimulated reservoir volume) of left image of Fig. 17, but it is in relative small size in order to capture the transient behavior near the fracture network.

Table (5) presents the main initial parameters of flow module for these three sub-pore media. The initial reservoir pressure is 3800 psi for all sub-pore media, and the constant bottom hole pressure is 800 psi. The initial permeability is 100 millidarcy for natural fracture, 420 millidarcy for hydraulic fracture, and 500 nanodarcy for shale matrix (non-organic and organic matter). Organic matter has larger porosity than non-organic matter, and the porosity of natural fracture is assumed to one. The gas diffusion and desorption are only consider for organic matter, and 20% TOC is assumed, which can be used to calculate the total number of organic matter grid block in the reservoir mesh. The initial water saturation is equal to irreducible water saturation 0.2, so water will not flow anywhere because of zero relative permeability, which makes the coupled flow simulation into a single phase flow simulation under stress compaction. The reservoir temperature is assumed constant, so no heat transfer and waste are happening.

For the input parameters of geomechanics module, the combined stress and displacement boundary conditions are used. Same with Fig. 10, the horizontal displacement is not allowed for the left boundary, and the vertical displacement is not allowed for the bottom boundary. In other words, u_h of left boundary and u_v of bottom boundary are equal to zero all the time. Constant overburden stress is applied on the top boundary and right boundary, which is main driver to produce displacements when the reservoir pressure is decreased. Biot's coefficient $b = 1.0$, Young's modulus $E = 5 \times 10^8\ pa$, Poisson's ratio $v = 0.3$, and the loaded overburden stress is equal to initial reservoir pressure. The vertical and horizontal displacement are solved for each node of every grid block at each time step.

Table 5: Initial parameters of flow module for the synthetic reservoir model.

Pore Medium	Natural Fracture	Non-organic	Organic
Density (kg/m^3)	--	2.6×10^3	1.35×10^3
Porosity	1.0	0.04	0.08
Permeability (nD)	1.0×10^8	500	500
Water Saturation	0.2	0.2	0.2
Pressure (Pa)	2.62×10^7	2.62×10^7	2.62×10^7
Diffusivity (m^2/s)	--	--	7.09×10^{-5}
Langmuir pressure (MPa)	--	--	10.34
Langmuir volume (m^3/kg)	--	--	1.17×10^{-2}
Temperature (K)	355	355	355

Due to the initial pressure difference between well bottomhole and reservoir matrix, gas will flow from the shale matrix into hydraulic fracture, and then into the wellbore, which in return causes reservoir pressure gradually reduce. Fig. 18 displays the pressure distribution of the reservoir mesh for two different times. Based on the color value bar, the red color represents high pressure, and the blue color represents low pressure. At the early producing time, the pressure of hydraulic fracture and natural fracture rapidly decreases because of large flow conductivity. On the right image of Fig. 18, the grid blocks with red color stands for organic grids with high pressure. Different with non-organic matter, the gas desorption could maintain the pressure for organic grid blocks.

Fig. 19 shows the numerical results of cumulative production mass along with time for four different reservoir cases. The case one is for the coupled model with constant permeability, which is the blue curve. The second case is for the coupled model considering the permeability change, where the entire shale matrix is considered as only non-organic matter. The red curve stands for the second case. The case three is for the coupled model considering the permeability change, where both non-organic matter and organic matter are regarded as shale matrix. However, the matrix shrinkage mechanism is not considered for organic matter in the third case. The green curve stands for the case three. The fourth case is almost the same with the third case, except the matrix shrinkage mechanism is considered for organic matter. The black curve stands for the fourth case.

On Fig. 19, the cumulative production mass is plotted along with time for four different reservoir cases, where x axis represents simulation time, and y axis represents cumulative production mass. By comparing these four cases, the cumulative production is apparently the largest for the first case because the reservoir permeability is not decreased at all. When the stress-dependent permeability is considered, the cumulative production is obvious declined. Comparing with case one, the cumulative production of case two is 12% smaller. This is because the reservoir permeability is reduced during reservoir depletion, where pore pressure is decreased and net effective stress is increased. Organic matter plays an important role in shale gas production, where gas desorption mechanism can boost the production rate at late stage. However, by comparing case two and case three, the cumulative production of case three is less, where even though organic matter is counted. This is because the permeability decline of organic matter is much larger than the decline

of non-organic matter based on the permeability correlations we chose. Therefore, for organic matter, the effects from reduced permeability on gas production is larger than the effects from gas desorption on production.

By comparing case three and case four, the impacts of matrix shrinkage on cumulative production should be observed and identified. However, no obvious difference of cumulative production between case three and case four is observed in Fig. 19. Initially, we thought it might be because of the high bottom hole pressure (800 psi), which did not provide much opportunity for matrix to shrink and boost the production rate. However, when we tried a lower bottom hole pressure 500 psi, the same result was obtained. After the results were carefully analyzed, two main reasons are provided below to explain why the effect of matrix shrinkage cannot be obviously observed on the cumulative production plots for case three and case four. The first reason is about TOC amount, the correlation coefficients, the desorption pressure, and the bottom hole pressure. The more TOC, the larger contribution from organic matter. The higher desorption pressure, the more the matrix can shrink and the higher the permeability could rebound.

The second reason is about reservoir pressure condition and relative value. Let us use the bottom hole pressure 500 psi as one example. Remember that the initial reservoir condition is 3800 psi, and the permeability rebound pressure is around 800 psi. The first stage of reservoir depletion was the reservoir was produced from initial pressure 3800 psi to the rebound pressure 800 psi, where the entire reservoir has been almost produced up and a large amount of hydrocarbon has been generated. For the second depletion stage of pressure from 800 psi to 500 psi, the matrix shrinkage did boost the permeability to some

degree, which improved the flow rate and total production. However, the relative low permeability, only 20% TOC, and the small pressure range (from 800 psi to 500 psi) could not provide large enough production boost to be obviously observed on the cumulative production curves. Above is the main reason why we couldn't observe an obvious increase on cumulative production plots for both BHP cases (800 and 500 psi) when we have considered the matrix shrinkage mechanism. But actually, the cumulative production was increased about 0.5% for the case of 800 psi after we compared the two final cumulative productions, which is just relatively too small to be observed. Overall, this numerical results demonstrate the impact of matrix shrinkage on cumulative production is quite limited.

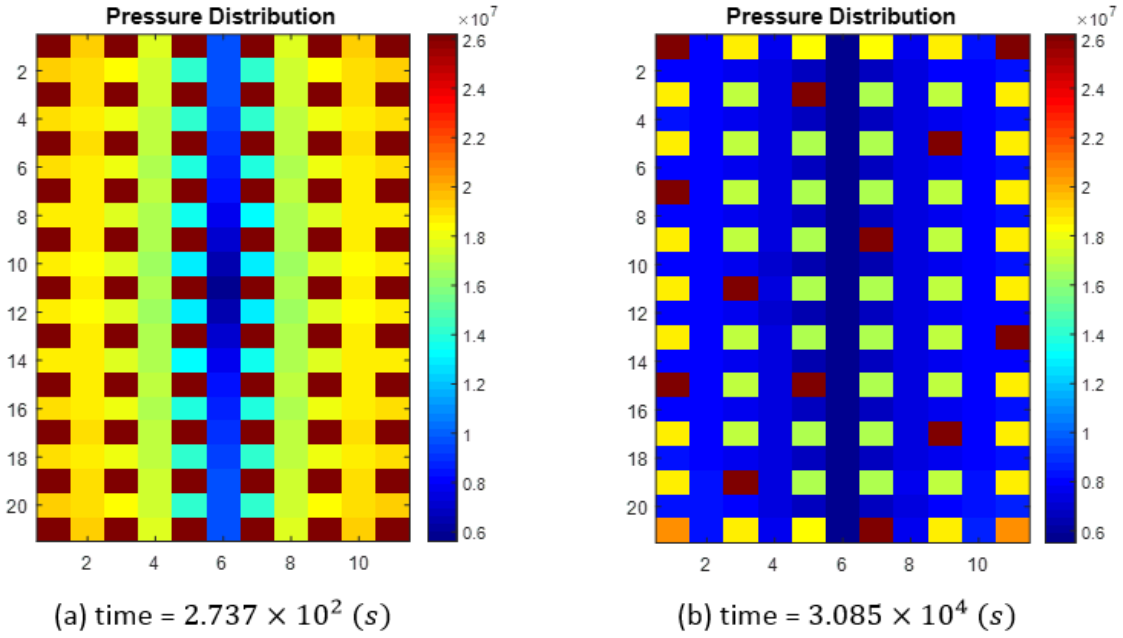

Figure 18: Pressure distribution of the reservoir mesh at two different times.

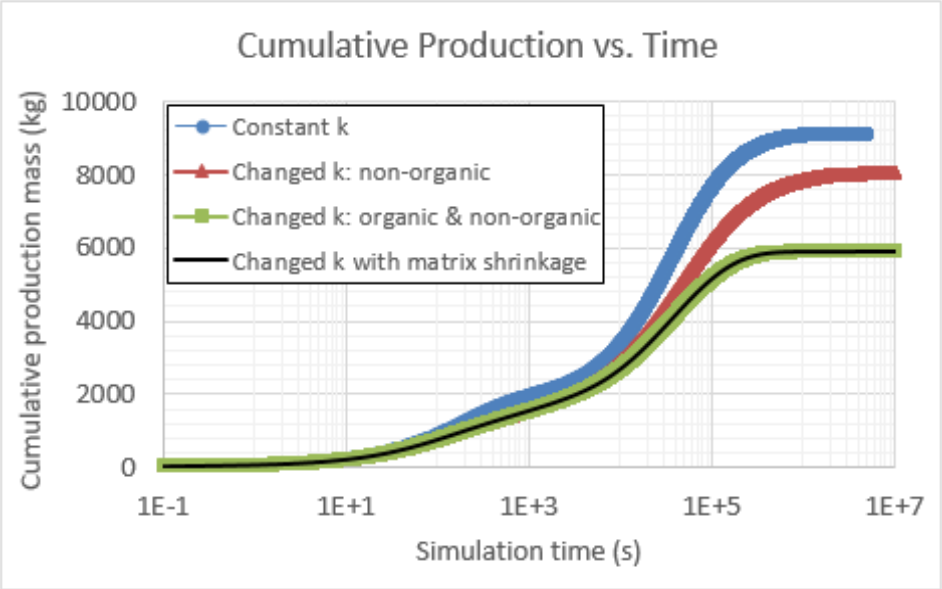

Figure 19: Results of cumulative production mass along with time for four different reservoir cases.

3.4 Sensitivity Study

As we mentioned above, the reservoir properties and geomechanics properties play an important role on affecting stress state, gas flow, and final production performance. In order to investigate the sensitivity, five parameters are chosen to study their impacts on cumulative production: Total Organic Carbon (TOC), matrix permeability, Young's modulus, Poisson's ratio, and bottom hole pressure. When the value of one parameter is changed, the others parameters keep the same value with the default model above. On Fig. 20, the mesh sketches of three TOC scenarios are shown for sensitivity analysis: 10%, 20%, and 30% TOC. The blue grids represent organic matter, which are randomly distributed on the mesh. The red grid block on the center represents the production well. As we introduced above, organic matter has been widely observed in shale reservoirs.

Based on extensively study of organic matter, the results show the increase of TOC could boost the gas production rate because of gas desorption mechanism. Fig. 21 displays the cumulative production versus time for three reservoir cases with different TOC, where the reservoir permeability is assumed constant. The results are the same with what we expect: the higher TOC brings higher cumulative production.

However, when the stress-dependent permeability is considered, different results will be obtained for the cases with different TOC, because non-organic matter and organic matter have different stress-permeability relationships described above. On Fig. 22, the results of cumulative production versus time are presented for three reservoir cases with different TOC, where the stress-dependent permeability has been considered. The bottom hole pressure we used in the models above is 800 psi. The results show the reservoir case with higher TOC brings lower cumulative production mass, which is inverse with the results on Fig. 21. The main reason is organic matter has larger permeability decline than non-organic matter under a same pressure drop based on the permeability relationships we chose. On the other hand, even though matrix shrinkage on organic matter could rebound permeability and boost production rate at low pressure range, the bottom hole pressure we used (800 psi) is not low enough for obvious rebound in terms of permeability. Therefore, a higher TOC didn't bring a larger cumulative production on the results of Fig. 22.

In order to investigate how much production will increase at certain amount of TOC when the matrix shrinkage is considered, Fig. 23 displays the simulation results for three cases with different TOC. The cumulative production increase value is obtained by comparing two cases: a) consider matrix shrinkage for organic matter; b) do not consider

matrix shrinkage. At 10% TOC, the cumulative production is increased 0.64% with the considering of matrix shrinkage. When TOC is increased from 10% to 30%, the production boost is improved. However, even though at 30% TOC, the cumulative production increase is about 2.24%. Of course, the simulation results are highly related to the permeability relationship we chose and other reservoir parameters, such as bottom hole pressure. To summarize, if the stress-dependent permeability is considered, a larger TOC cannot bring a higher cumulative production. A high TOC can contribute permeability rebound and production boost because of matrix shrinkage. However, the impacts of matrix shrinkage on cumulative production is quite limited.

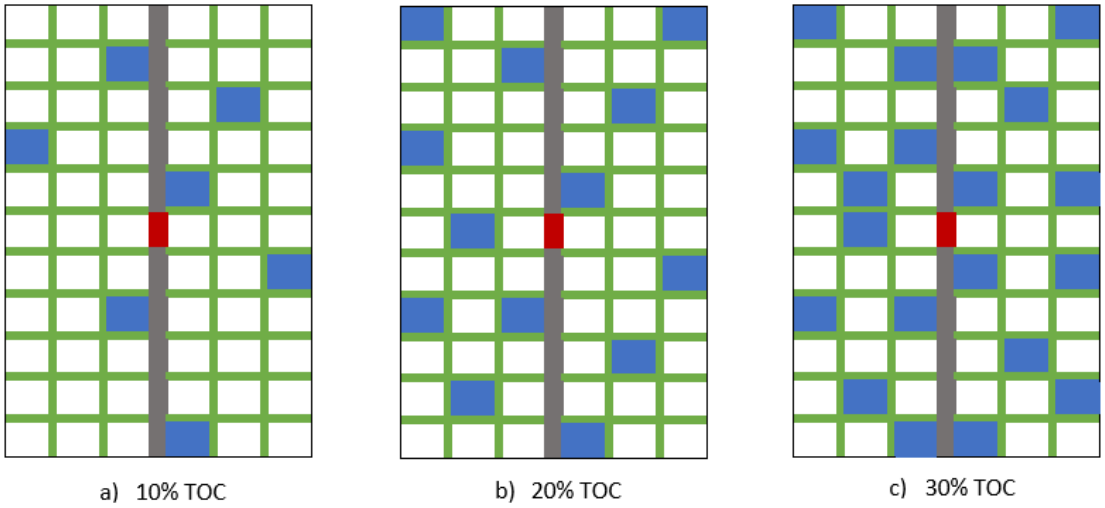

Figure 20: The mesh sketches of three TOC scenarios for sensitivity analysis.

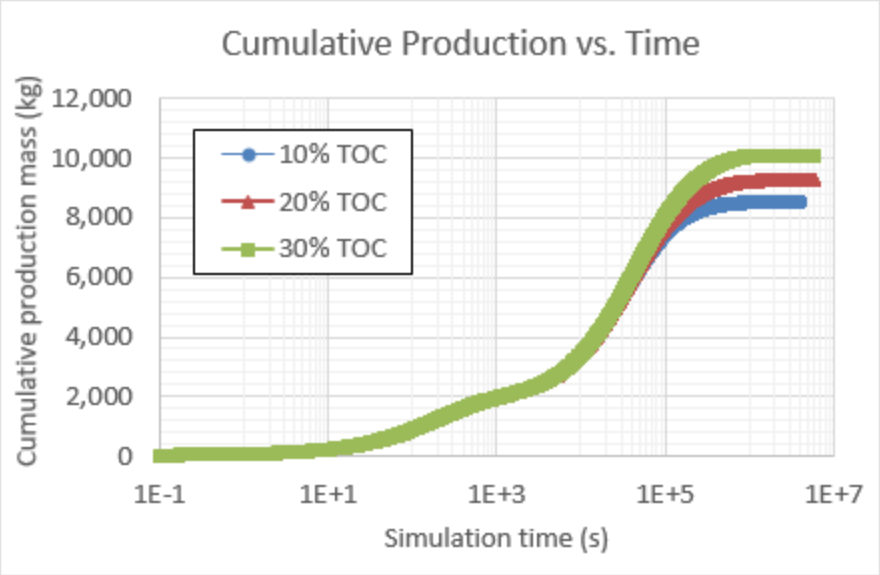

Figure 21: Cumulative production versus time for different TOC cases with constant permeability.

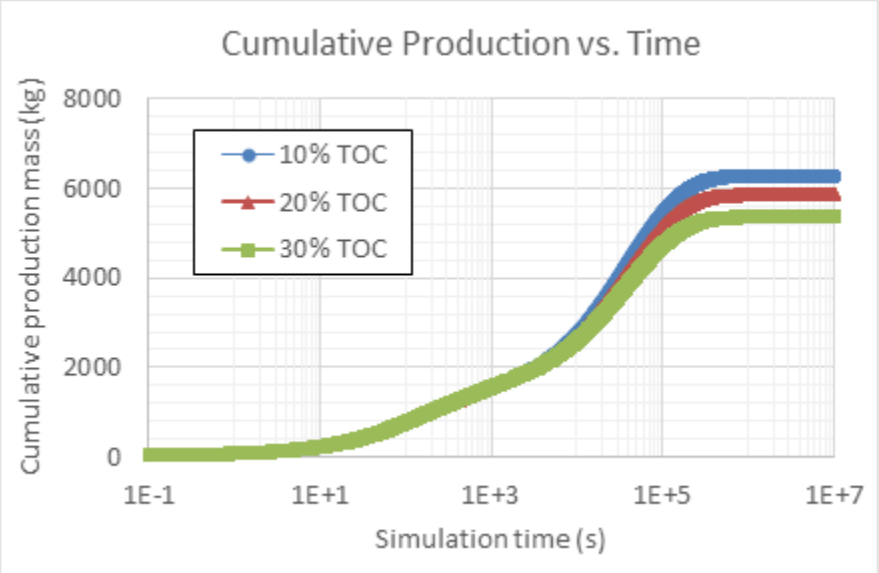

Figure 22: Cumulative production versus time for different TOC cases with stress-dependent permeability.

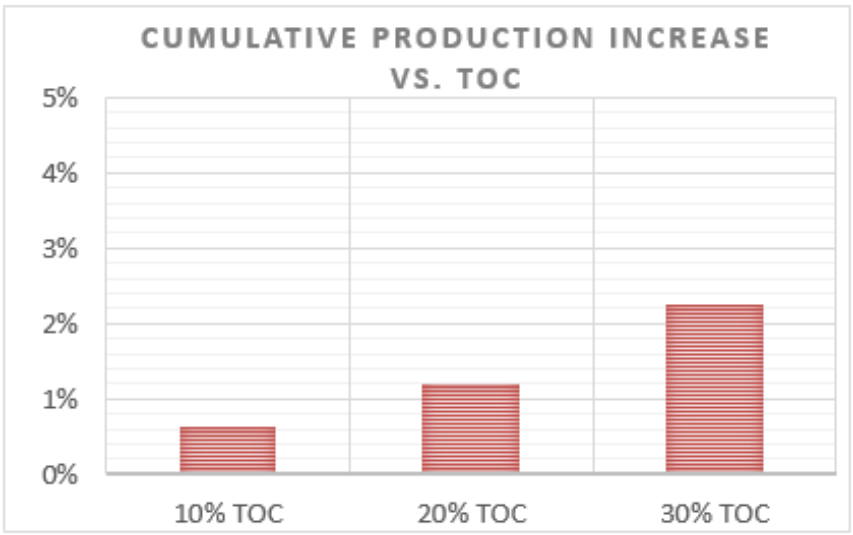

Figure 23: The cumulative production increase versus TOC when matrix shrinkage is considered.

Fig. 24 presents the cumulative production versus time for three cases with different matrix permeability, where the permeability is not dependent with the stress change. The results show the final cumulative production is the same for the three cases of different permeability. However, the case with larger matrix permeability provides a higher production rate at most producing time, and it reaches the final stage much earlier. When the stress-dependent permeability is considered for the three cases, the results of cumulative production are shown on Fig. 25. The results of Fig. 25 look similar with that of Fig. 24, while two different points are noted. Firstly, the final cumulative production of Fig. 25 is much smaller than the results of Fig. 24, because the reservoir permeability is reduced along the drop of reservoir pressure. Secondly, at a certain time range from 1E+3 to 1E+5 second, the cumulative production gap between different permeability curves on Fig. 25 is smaller than the gap on Fig. 24. Let us explain the reasons as follows.

Fig. 26 displays the results of cumulative production loss versus permeability at the time of 1E5 seconds, where the stress-dependent permeability is considered. For example, when the matrix permeability is 250 nanodarcy, the cumulative production loss is 30% on the y axis, which means the cumulative production from the case considering permeability change is 30% less than the case with constant permeability. When the matrix permeability rises, the cumulative production loss is increased. The cumulative production loss is 35% for the case of 1000 nanodarcy. Therefore, the case of 1000 nanodarcy has a larger loss than the case of 500 nanodarcy in terms of cumulative production, which makes the gap between them reduced. This is why the cumulative production gap between different permeability curves is reduced on Fig. 25. To be clear, the final cumulative production is the same between different permeability cases no matter the stress-dependent permeability is considered or not, as shown on Fig. 24 and Fig. 25. The cumulative production loss we are talking above is just for at a certain time, which is mainly caused by the decline of production rate. Overall, the case with higher matrix permeability encounters a larger loss of production rate at a certain time range when the stress-dependent permeability is considered.

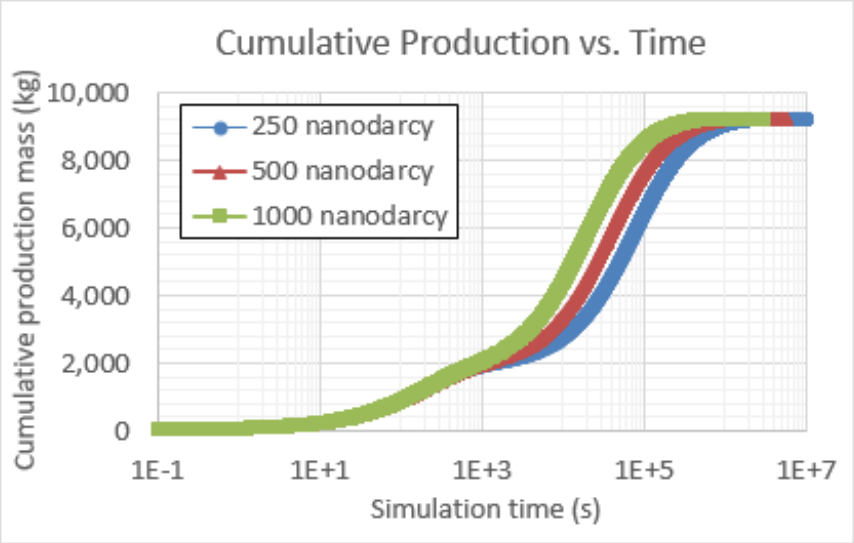

Figure 24: Cumulative production versus time for different permeability cases with constant permeability.

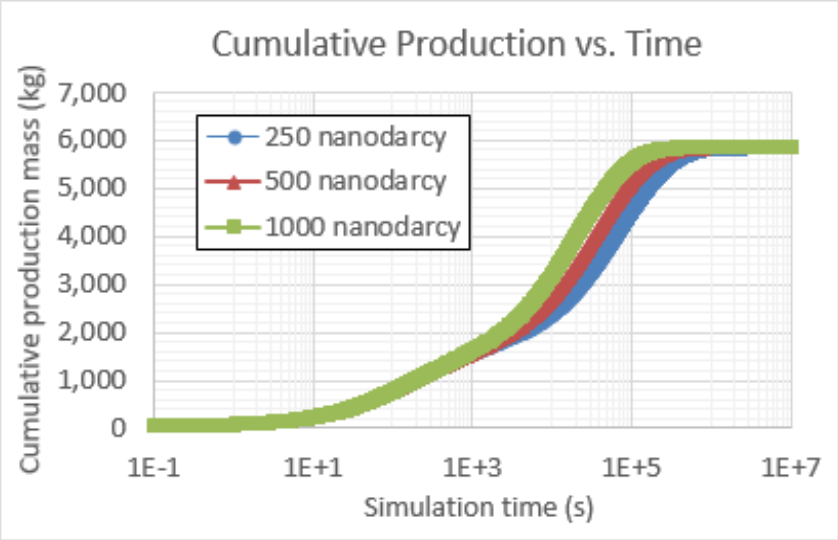

Figure 25: Cumulative production versus time for different permeability cases with stress-dependent permeability.

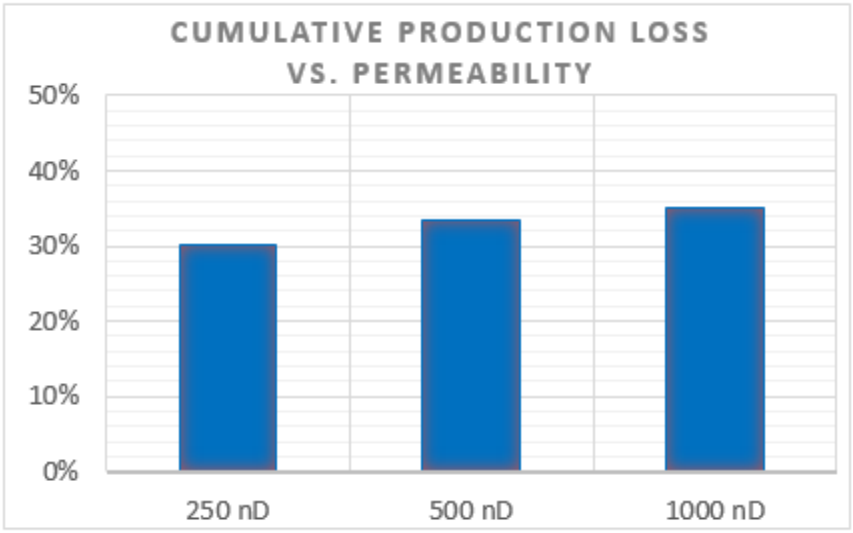

Figure 26: Cumulative production loss versus permeability at 1E5 seconds.

Fig. 27 presents the sensitivity analysis results for three different Young's modulus E: $5 \times 10^8, 10 \times 10^8, 15 \times 10^8$ pa, where the cumulative production mass is plotted along with simulation time. The results show a smaller Young's modulus brings a higher cumulative production mass. When Young's modulus is increased, the cumulative production mass is reduced. Young's modulus is a measure of the stiffness of a solid material. Typically, hard materials have larger Young's modulus, and soft materials have small value. On the other hand, compaction drive plays an important role in production performance for coupled flow-geomechanics system, while a larger Young's modulus could offset the impacts of compaction drive on production. Therefore, the cumulative production is declined when Young's modulus is increased. Another important note is observed for the results related to Young's modulus on Fig. 27. When Young's modulus is increased, the drop of cumulative production gradually becomes small. In other words, at a level with large Young's modulus, the increase of Young's modulus will not bring

large drop of cumulative production. When Young's modulus reaches a certain large value, the change of Young's modulus will not have obvious effects on the cumulative production.

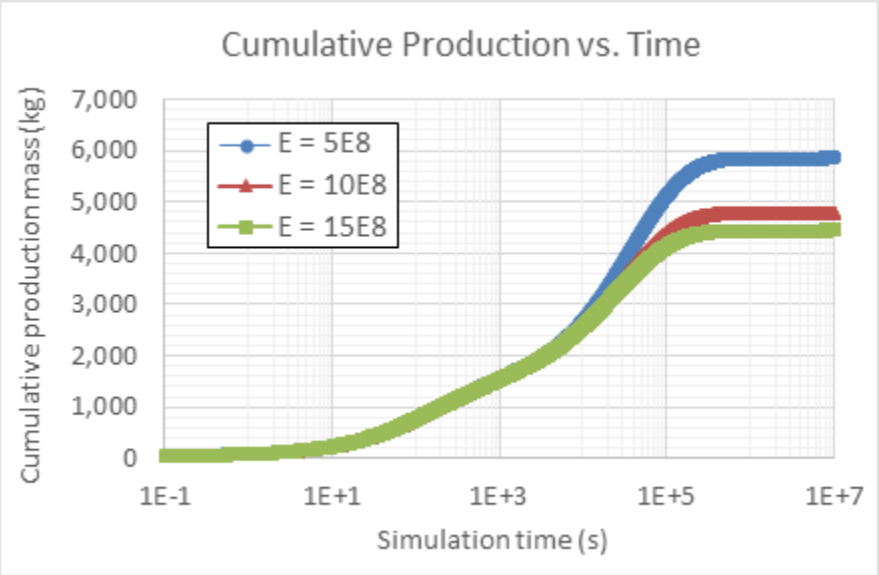

Figure 27: Results of sensitivity analysis for Young's modulus.

Fig. 28 illustrates the simulation results of cumulative production obtained from different Poisson's ratio. A higher cumulative production is obtained from a smaller Poisson's ratio. When Poisson's ratio is increased, the cumulative production is decreased. Poisson's ratio is the ratio of transverse strain to axial strain. A larger Poisson's ratio means a bigger transverse strain, which could in return offset the compaction impacts on reservoir production. On the other hand, based on Eq. (43) and (44), when Poisson's ratio is increased, the change of effective stress is boosted and the permeability is reduced. Therefore, an increase of Poisson's ratio leads to a decrease of cumulative production.

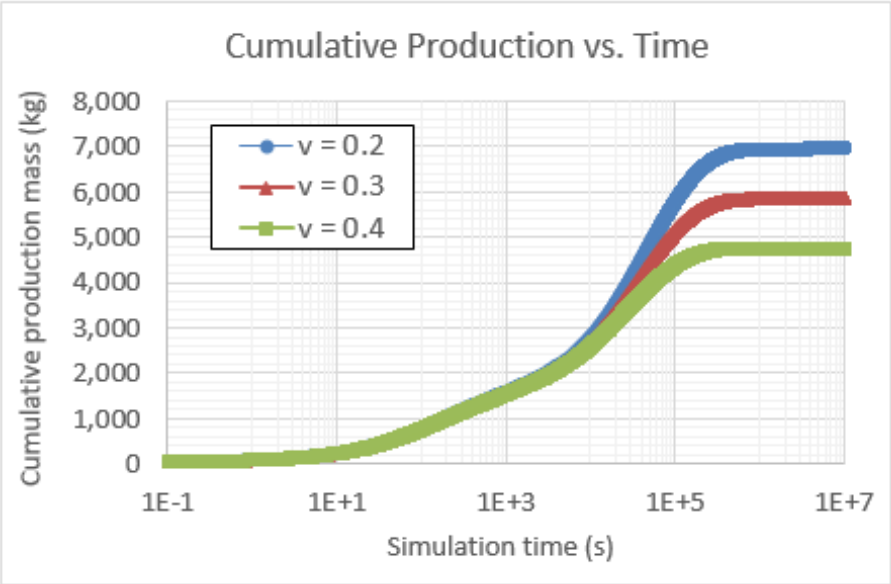

Figure 28: Results of sensitivity analysis for Poisson's ratio.

Fig. 29 and Fig. 30 display the sensitivity analysis results about Bottom Hole Pressure (BHP), which could be controlled by field operator to adjust reservoir production performance. Four cases with different values of BHP are chosen: 400 psi, 600 psi, 800 psi, and 1000 psi. Fig. 29 shows the results for the cases considering the stress-dependent permeability. Fig. 30 shows the results for the cases with constant permeability. For both cases with and without stress-dependent permeability, a lower bottom hole pressure brings a higher cumulative production. When BHP is increased, the cumulative production is reduced. By comparing the results of Fig. 29 and Fig. 30, we observe the cumulative production gap between different bottom hole pressures is reduced when the stress-dependent permeability is taken into account. Fig. 31 presents the reduced cumulative production ratio results changes along with bottom hole pressure. The reduced cumulative production ratio is defined as the ratio of the production loss when considering stress-

dependent permeability to the cumulative production with constant permeability. For example, when BHP is equal to 800 psi, the cumulative production mass is 9236 kg for the constant permeability case and 5850 kg for the changed permeability case. Therefore, based on the constant permeability case, the cumulative production loss is 36.7% when the stress-dependent permeability is considered. On Fig. 31, the results of reduced ratio are presented for four different BHP, where a lower bottom hole pressure leads to a larger reduced ratio. When BHP is increased, the relative production loss is decreased. However, even though increasing BHP could offset certain production loss caused by the permeability decline, it is not a good strategy for a long-term production view. Overall, no matter the stress-dependent permeability is considered or not, bottom hole pressure has a large impacts on the cumulative production. A lower bottom hole pressure bring a higher cumulative production.

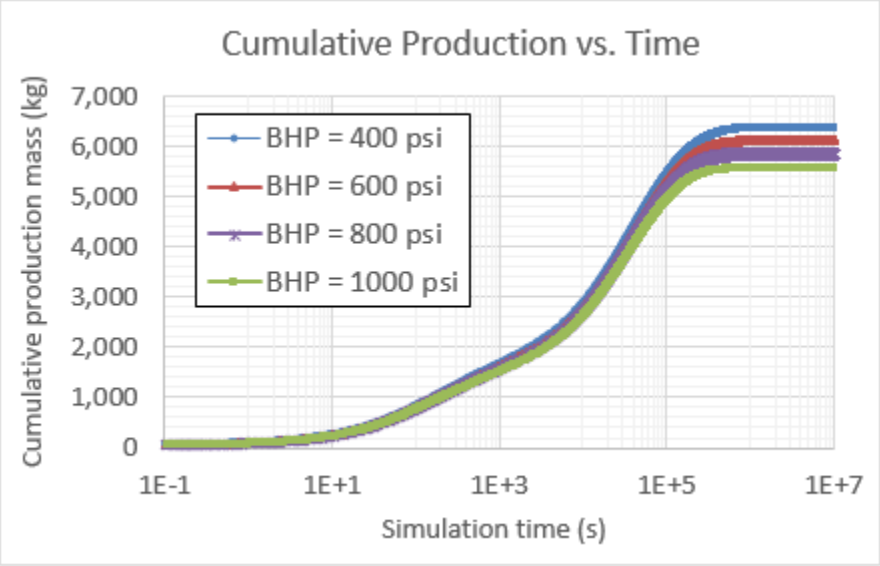

Figure 29: Results of sensitivity analysis for BHP with stress-dependent permeability.

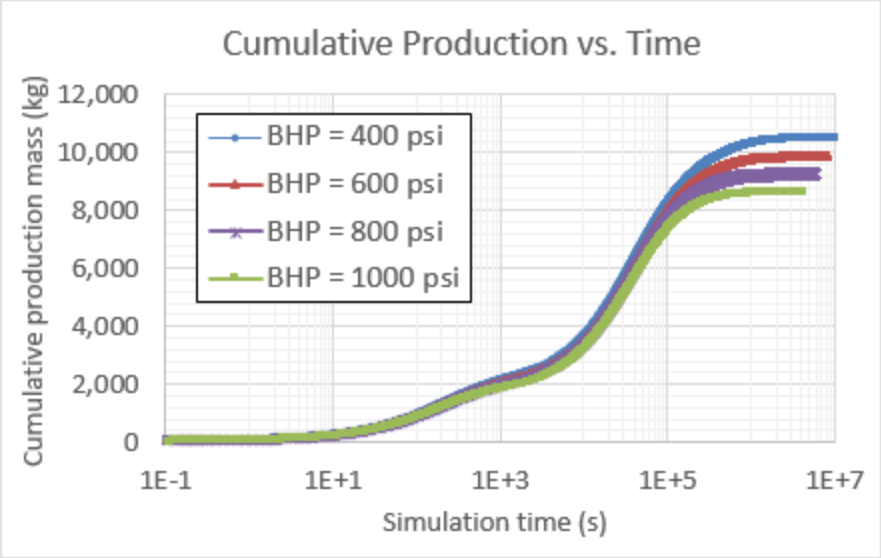

Figure 30: Results of sensitivity analysis for BHP with constant permeability.

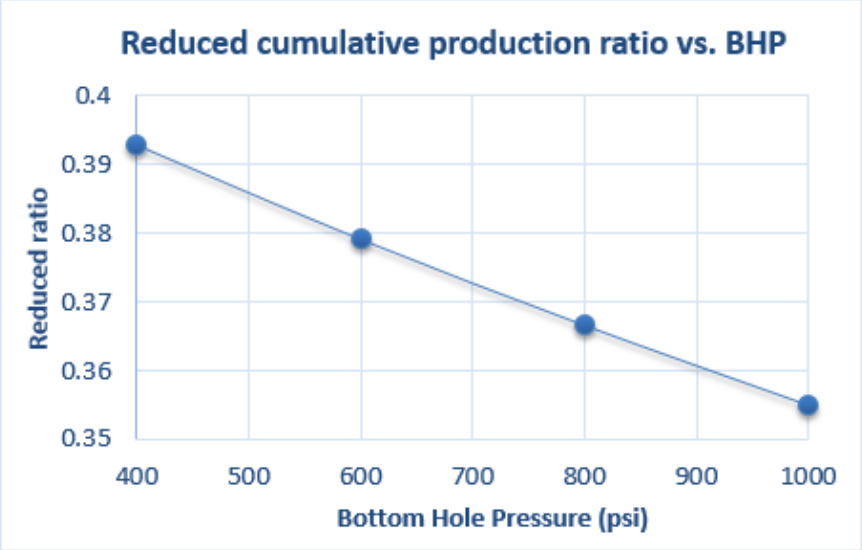

Figure 31: Reduced cumulative production ratio changes along with BHP.

3.5 Conclusions and Discussions

3.5.1 Conclusions

In the study of this chapter, the coupled flow-geomechanics simulator is applied to investigate the impacts of stress changes and matrix shrinkage on reservoir permeability and gas production performance for organic-rich shale reservoirs. The reservoir mesh is divided into non-organic matter, organic matter, and natural fracture. In addition to stress-dependent permeability, matrix shrinkage has been considered for organic matter because of gas desorption phenomenon. Different stress-permeability correlations are chosen to separately apply into the three sub-pore media based on their rock properties and compaction behaviors. The mass-balance equations and stress-equilibrium equations are solved by the fixed-stress iteratively sequential method, where the flow equations are solved first, followed by the mechanics equations. A synthetic reservoir model has been built to investigate the impact of the stress-dependent permeability on gas production performance. In addition, the sensitivity analysis were conducted for Total Organic Carbon (TOC), matrix permeability, Young's modulus, Poisson's ratio, and bottom hole pressure. Overall, several main conclusions as following are obtained from this study:

- If the stress-dependent permeability is considered, the permeability and cumulative production will be significantly reduced. Additionally, the production loss is highly dependent on the selected permeability correlations and their coefficients.
- The matrix shrinkage on organic matter could rebound the permeability and improve the cumulative production at the low reservoir pressure stage. However,

the impact of matrix shrinkage on cumulative production is quite limited, which is largely related to Total Organic Carbon, the correlation coefficients, gas desorption pressure, and bottom hole pressure.

- Due to large permeability decline, a higher Total Organic Carbon does not necessarily bring a higher cumulative production, which is inverse with the results from regular reservoir simulation without considering the stress-dependent permeability.
- When the stress-dependent permeability is considered, a higher matrix permeability encounters a larger loss of production rate.
- When Young's modulus reaches a certain value, the change of Young's modulus will not make obvious differences on the cumulative production any more.
- A higher cumulative production is predicted from a smaller Poisson's ratio.
- A higher bottom hole pressure could offset certain production loss caused by the permeability decline, while it is not the best strategy in terms of Estimated Ultimate Recovery.

Overall, based on the provided bottom hole pressure, Total Organic Carbon, and permeability correlations, the matrix shrinkage on organic matter has not made obvious differences on the cumulative production. When the stress-dependent permeability is taken into account, the cumulative production is undoubtedly reduced because the permeability is decreased along with the decline of reservoir pressure. Therefore, to maintain reservoir pressure, such as water injection, could prevent the permeability from

declining. On the other hand, the production loss caused by the stress-dependent permeability highly depends on the selected correlation and their coefficients. Selecting appropriate permeability correlation for different pores media is critical to better describe the compaction behaviors and the permeability change. After the permeability correlation was selected, the coefficients are mainly obtained by matching the experiment data with the equation curve. Different core samples could behavior dissimilarly under the same compaction stress, which in return provides different experimental results and permeability coefficients. Therefore, to choose appropriate permeability correlation and obtain correct coefficients plays a significant role on investigating how the permeability changes during reservoir depletion and how much the impact of stress-dependent permeability on production performance will be.

3.5.2 Discussions

The study of this chapter was about investigating the effects of stress-dependent permeability and matrix shrinkage on permeability change and production performance for organic-rich shale reservoirs. The motivation was mainly from the observations of many experiment measurement data of shale reservoirs: 1) rock permeability significantly decreases along with the increase of effective stress; 2) different porous media, such as organic matter and natural fracture, present dissimilar compaction behaviors. The results and conclusions of this study are mainly obtained from numerical modeling of a synthetic reservoir model and some sensitivity analysis. The Permian Basin is providing excellent resources including shale and other unconventional rocks for oil and gas production to

satisfy the growing energy demand. Even with the current low oil price market, the drilling and production activities in both conventional and unconventional plays are the most active in the Permian Basin. Therefore, if the stress-dependent permeability and matrix shrinkage are applicable to the Permian Basin, how much effects they will make on production, and how we can use the results of this study for field development are attracting much attention and interests.

Briefly speaking, if the proposed triple-porosity coupled model can be used for the Permian Basin unconventional reservoirs or not highly depends on the rock composition and the formation lithology. The percentage and distribution of organic matter and natural fractures firstly need to be understood. More importantly, rock permeability should be measured with core samples under different effective stresses, where the permeability change and related coefficients should be monitored and recorded. Then, we can determine if the proposed model with different stress-dependent permeability correlations should be applied to the Permian Basin reservoirs.

Let us assume here if the mechanisms of stress-dependent permeability and matrix shrinkage are required for the Permian Basin reservoirs based on the obtained information, the proposed triple-porosity model can offer great benefits to production evaluation and economic assessment by providing a more accurate and realistic prediction. If the stress-dependent permeability has not been considered for the reservoir which experienced the permeability decline, the hydrocarbon production will be significantly overestimated which might lead to unwise management decisions.

Based on the proposed model, we can better understand the effects of Young's modulus, matrix permeability, bottom hole pressure, Total Organic Carbon on the cumulative production. That sensitivity analysis could provide guide to field development for operating the formation with different rock properties. To maintain reservoir pressure could slow down the permeability decline and improve the production rate and producing time. For example, water injection might be an available option. The proposed model is also helpful to decide when, how and where for the water injection. In addition, choosing approximate production rate and bottom hole pressure could minimize the decrease of reservoir permeability and take advantage of matrix shrinkage as well.

CHAPTER IV

ADAPTIVE TIME STEPPING METHOD*

4.1 Introduction

Coupled flow-geomechanics model is needed for investigating the stress change, rock-compaction behavior, and stress-dependent properties in many practical reservoir scenarios. However, the coupled model of large-scale simulation problems usually encounters large matrix system and high computational expenses, where the time stepping is a crucial factor for numerical stability and computational efficiency. The local error or the residual are usually calculated and compared with a given tolerance at each time step to decide if a desired solution accuracy has been reached or the time step needed to be modified. One typical option for optimizing the simulation is to choose the largest time step size that can lead to both an acceptable error and relative accurate solution at the same time. Comparing with the constant time step size, variable time step-sizes can be very valuable for controlling the local truncation error and improving the computational efficiency of stiff problems (Shampine 2004; An et al. 2017d). Watts (1984) proposed to use the locally optimal step size strategy to control the errors for solving the ordinary differential equations. Sinkin et al. (2003) studied the efficiency of different implementations of split-step Fourier method for solving the nonlinear Schrödinger

* Part of data reported in this chapter is reprinted with permission from "A Modified Local Error Method for Adapting Time Step-size in Coupled Flow-geomechanics Problems" by An, C., Wang, Y., Wang, Y., Killough, J., 2018. Journal of Petroleum Science and Engineering, Volume 162, Pages 763-773, Copyright 2018 by Elsevier.

equations. Their results showed the local error method performs best for modeling optical solutions and single-channel transmission systems. Minkoff and Kridler (2005) compared three adaptive time stepping methods on a simple loosely-coupled simulator modeling single-phase flow and linear elastic deformation. They stated the local error method is the best able to significantly cut down the total numerical error among the three methods.

In the study of this chapter, an adaptive time stepping method with the modified local error technique is proposed to reduce the total iteration time and improve the computational efficiency for the coupled flow-geomechanics simulator. Firstly, the adaptive time stepping method is explained in details. Since updating geomechanics module consumes most of the computing time of the coupled system, the adaptive time stepping method is mainly used for geomechanics module to adapt the time step size based on the change of displacement. Secondly, a synthetic two-dimensional coupled production problem is built to apply the modified local error method for investigating its accuracy and computational efficiency. The numerical results are compared with the fully-coupled method and the regular iteratively method. Finally, the sensitivity about the local error tolerance on the numerical results is investigated. Some conclusions and discussions are provided as well.

4.2 Methodology for Adaptive Time Stepping

Adaptive time stepping methods are widely used to control the step size and improve the computationally efficient in ordinary differential equation solvers (Gear 1971), such as Runge-Kutta-Fehlberg method. Sinkin et al. (2003) introduced a local error

method to solve the optical-fiber communications systems, where the error is bounded in each time step by applying the step-doubling and local extrapolation techniques. Minkoff and Kridler (2005) compared three different time stepping methods in terms of computation cost and accuracy for a simple loosely-coupled simulator, where the local error method and the pore pressure method are explained.

The detailed procedures about the regular local error method are described as following. Suppose the fluid flow simulation initially starts with a time step t and an error tolerance of displacement ε_u. Firstly, the flow and mechanics equations are sequentially solved for the time step t twice as shown on right side of Fig. 32, where the pressure variable is always solved firstly on the flow balance equation, followed by the displacement variable at each time step. After two time steps, the displacement u_f is obtained and regarded as fine displacement solution. Secondly, the same flow and mechanics equations are sequentially solved for the time step $2t$ once as shown on left side of Fig. 32, where the displacement u_c is calculated and regarded as coarse displacement solution. By calculating the relative difference between the coarse and fine displacements, the relative local error δ can be defined and calculated by Eq. (47), where the L2 norm is used. We can then determine whether the current time step t needed to be modified or not by comparing the relative local error with the error tolerance of displacement.

$$\delta = \frac{\|u_f - u_c\|}{\|u_f\|} \tag{47}$$

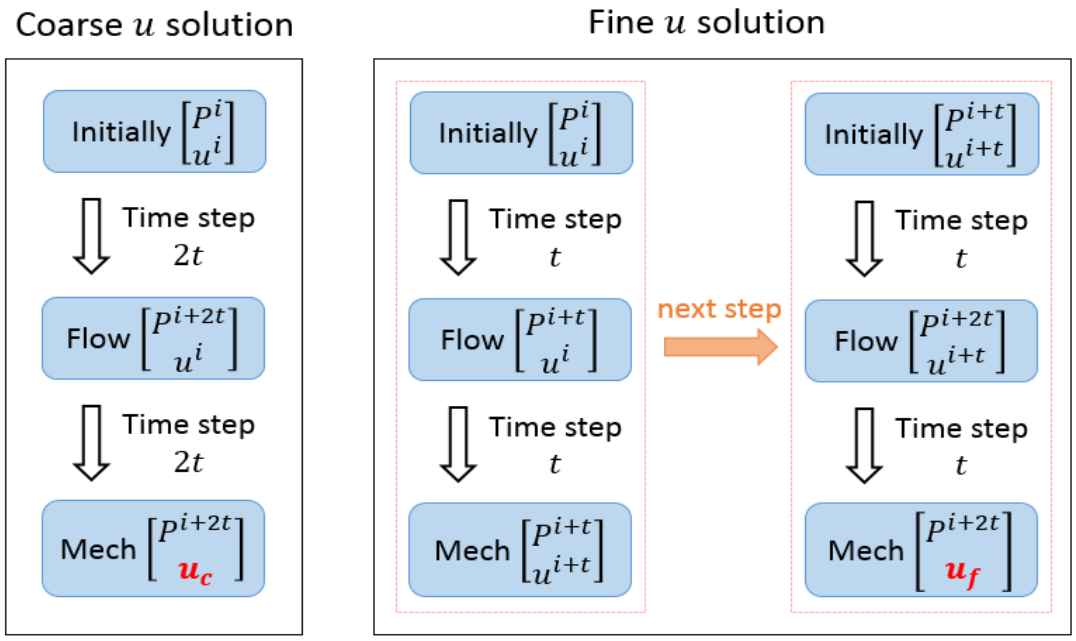

Figure 32: Schematic of local error method for iteratively coupled scheme.

For the local error method used in the paper of Minkoff and Kridler (2005), only the time step size of mechanics equation is adapted while the time step of flow is assumed to be fixed. However, in addition to the time step in mechanics module, the time step of flow is also simultaneously adapted based on the relative local error in this study. This is because the change of displacement is mainly caused by the change of pressure. If the change of displacement is really small, which means the change of pressure is little, we can choose to increase the time step size for the flow equation at that moment. Due to both step size of flow and mechanics will be adapted, we call this approach as the modified local error method. The main algorithm about our modified local error method is described as Eq. (48). After obtaining the relative local error δ, we compare it with the error

tolerance of displacement ε_u in order to decide if we need to adapt the step size for next time step. As shown on Eq. (48), Δt is the current time-step size and t_{next} represents the size of next time step.

If δ is smaller than half of ε_u, which means the relative error of displacement is significantly small and the model computation is really accurate, the time step size will be doubled for next time step. If δ is between half ε_u and ε_u, the step size will be kept the same for next time step. If δ is between ε_u and $2\varepsilon_u$, the step size will be divided by $\sqrt{2}$. Finally, if δ is larger than $2\varepsilon_u$, which means the relative local error is too large, the time step size will be halved in order to increase the accuracy for next time step. In order to optimize the computing process, the relative local error is checked every five time steps to determine if the step size need to be adapted. For example, when the step size is modified once at current time step, the updated step size will be used for the next four iteration running. Then on the fifth time step, the algorithm is applied again to check if the step size need to be modified for next time step.

$$\begin{cases} \delta \le \frac{1}{2}\varepsilon_u & t_{next} = 2 \times \Delta t \\ \frac{1}{2}\varepsilon_u < \delta \le \varepsilon_u & t_{next} = \Delta t \\ \varepsilon_u < \delta < 2\varepsilon_u & t_{next} = \frac{\Delta t}{\sqrt{2}} \\ \delta \ge 2\varepsilon_u & t_{next} = \frac{\Delta t}{2} \end{cases} \tag{48}$$

4.3 Numerical Results for Coupled Model Application

A synthetic two-dimensional reservoir problem is introduced to apply the modified local error method. In this coupled model, we assume the isothermal single liquid flow,

stress-independent fluid properties, and no gravity. Fig. 33 shows the schematic of 2D coupled model including one production well. Left side and bottom side of this 2D model are no flow boundaries. The horizontal displacement is not allowed for the left boundary, and the vertical displacement is not allowed for the bottom boundary. In other words, u_h of left boundary and u_v of bottom boundary are equal to zero all the time. Constant overburden stress are applied on the top boundary and right boundary, which could force the solid frame to shrink. One production well exists in the center of the reservoir model, which is the main driver source for the drop of pressure and happening of displacements along with time.

Table (6) presents the fluid and rock properties for the 2D coupled model, where the international unit system is used. The mesh of this 2D model is divided into 21×21 grid blocks for simplicity and the grid size is assumed one meter. The overburden pressure is equal to the initial reservoir pressure, so the fluid drainage will not happen on both top and right boundaries. Since the bottom hole pressure is less than the initial reservoir pressure, the fluid will flow into the wellbore and the pressure of reservoir will be reduced, which leads to the solid displacements. Peaceman (1983) developed a general well formulation on rectangular grids for single phase flow, which relates the computed grid pressure with the flowing bottom hole pressure. Based on that, the well equation used in this study is shown as on Eq. (49), where q denotes flow rate, P_{wf} represents the flowing bottom hole pressure, P_{well} stands for the pressure of the block containing the well, WI is the well index relating to well geometric and fluid properties. More details about this well formulation can be found in Dake (1983) and Ertekin et al. (2001).

$$q = WI \times (P_{wf} - P_{well}) \quad (49)$$

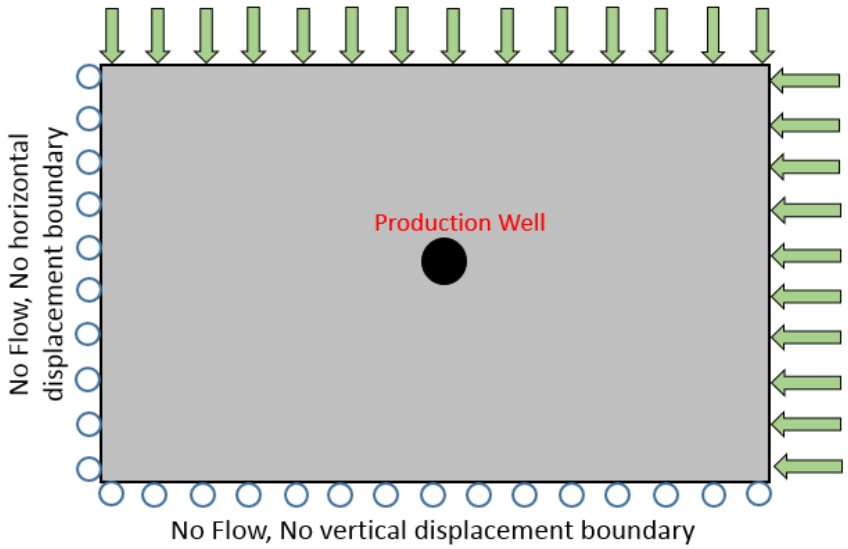

Figure 33: Schematic of 2D coupled Model including one production well.

Table 6: Fluid and rock properties for the 2D coupled model.

Parameters	Values (unit)
Grid size (Δx)	$1\ (m)$
Porosity (ϕ)	0.25
Permeability (k)	$4.9346 \times 10^{-14}\ (m^2)$
Fluid viscosity (μ)	$1 \times 10^{-3}\ (Pa \cdot s)$
Fluid compressibility (c_f)	$4 \times 10^{-10}\ (1/Pa)$
Initial Pressure (P)	$1 \times 10^{7}\ (Pa)$
Bottom hole pressure (P_{wf})	$8 \times 10^{6}\ (Pa)$
Young's modulus (E)	$5 \times 10^{8}\ (Pa)$
Poisson's ratio (v)	0.3
Biot's coefficient (b)	1.0
Overburden stress (σ_F)	$1 \times 10^{7}\ (Pa)$

Fig. 34 shows the results of pressure of well block and production rate versus time for three different numerical cases: the fully coupled model, the sequential coupled model, and the model with adaptive time step method. In this section, the sequential coupled denotes the normal iteratively coupled method without adapting time step size, while the adaptive time step method stands for the normal iteratively coupled method applying the modified local error method to adapt the time step size. Both the fully coupled and sequential coupled method use the fixed time step size. For all these three different numerical schemes, the initial time step is 0.1 second and the simulation is set to only run 1000 seconds. Because the time step size is fixed for the fully-coupled and sequential-coupled models, both models need to be run 1×10^4 times to reach the final time 1000 seconds. However, for the adaptive time step method, the running iteration time is much shorter because the size of time step is always adapted based on the algorithm mentioned above. The key parameter, error tolerance of displacement, is 5×10^{-3} for this 2D coupled model. On Fig. 34, the normalized pressure is calculated through dividing the pressure of well block by the initial pressure. Additionally, a decrease of well block pressure leads to a drop of production rate. The results of pressure and production rate show a really good match among these three different models on Fig. 34, which validates the accuracy of our sequential coupled model with the application of the adaptive time stepping method.

Image (b) of Fig. 35 shows the visualization results of the 2D pressure distribution from the adaptive time step method. The yellow color represents high pressure, and the dark blue represents low pressure. Since the simulation is only performed 1000 seconds, the pressure wave has not reached the domain boundary yet. The grids close to the well block obviously have lower pressure than the other grids because the fluid is drained into the wellbore. To validate the accuracy of the finite element method, especially for the calculation of displacements, the results of displacements on one selected layer are compared among this three different models. The vertical displacements of the eleventh layer (we count from top to bottom layer based on image (b) of Fig. 35) are plotted as on image (a) of Fig. 35. Both the pressure distribution and the vertical displacement results are obtained at the end of simulation time. The vertical displacements on these 22 nodes show a great match among the three different models, which cross-validates the accuracy of displacement when the sequential coupled model is used with the adaptive time-step method. Additionally, due to the presence of the producing well, the middle nodes apparently have larger displacement than that of two side's nodes. A larger pressure drop leads to a bigger displacement change. It is worthy to note that the displacement results are not entirely symmetric because of non-symmetry boundary conditions (we used the combined displacement and stress boundary conditions).The displacements on two sides of well vary differently depending on the distance to the well block. Overall, the adaptive time step method with sequential coupled scheme provides an accurate enough solution for the coupled problem. In other words, the accuracy is not sacrificed when we apply this adaptive time step method for the coupled model.

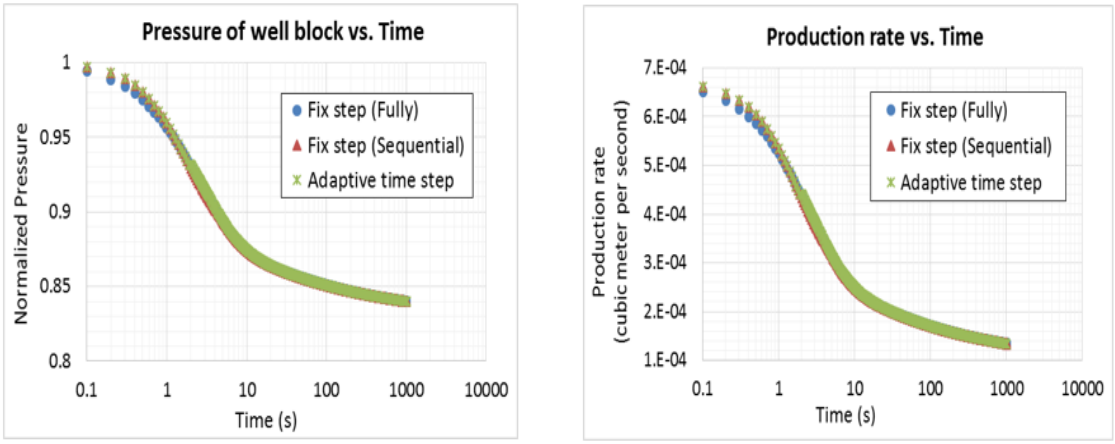

Figure 34: Comparison of pressure and production rate for three different numerical schemes.

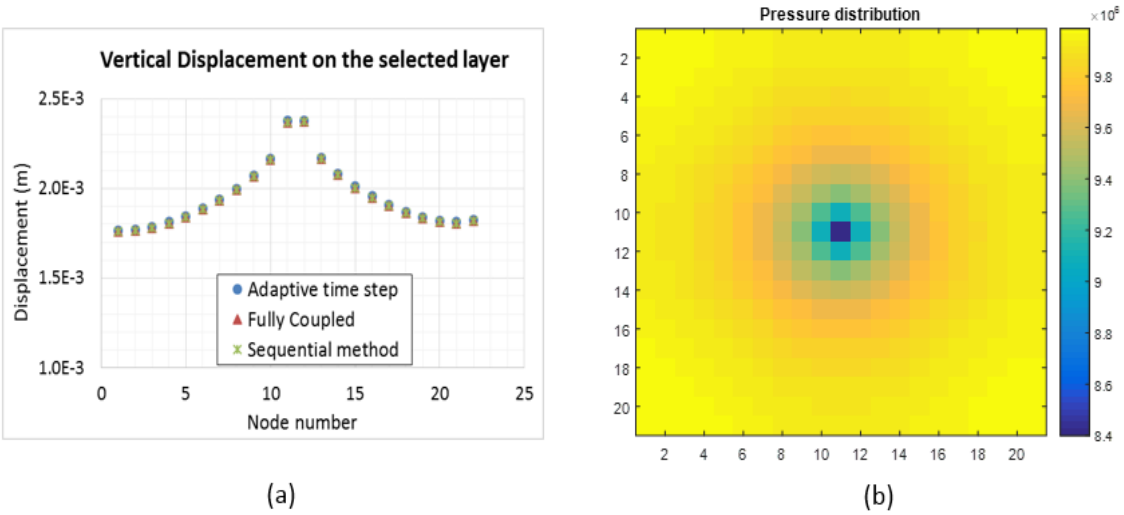

Figure 35: (a) Comparison of vertical displacements for three different numerical schemes; (b) Results of pressure distribution from adaptive time step method.

Fig. 36 shows the size of time step changes along with the number of time steps for adaptive time-step method. The initial time step size is 0.1 seconds, and then it is reduced two times into 0.035. After about 60 times iteration running, the size of time step starts to be increased. When the time step size is boosted every time, it usually lasts a

while before next time's change. The time step size is kept being boosted until into 36 second, where the simulation ends. At the early stage of the production problem, the changes of pressure and displacement are very sensitive to time step, so the step size was repeatedly cut to ensure the accuracy. However, at the late production period, the pressure and displacement do not vary much at each time step, so the algorithm of local error method was triggered to adapt the size of time step. Fig. 37 displays the results of pressure and production rate with a larger initial time step size (2 seconds) for fully coupled and adaptive time step method. The results from the adaptive time step method are not well matched with the results from the fully coupled model, especially at the early stage of production. Different with the results on Fig. 34, when the large initial time step size is used, the numerical results from the adaptive time step is not accurate enough. Therefore, a relative small value of initial time step is required for the sequential method, which in return could enhance the advantage of adaptive time step method.

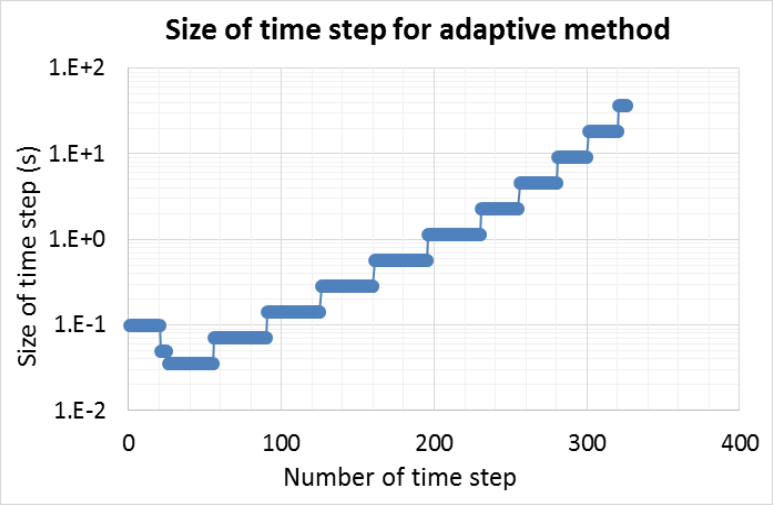

Figure 36: The change of size of time step for adaptive time step method.

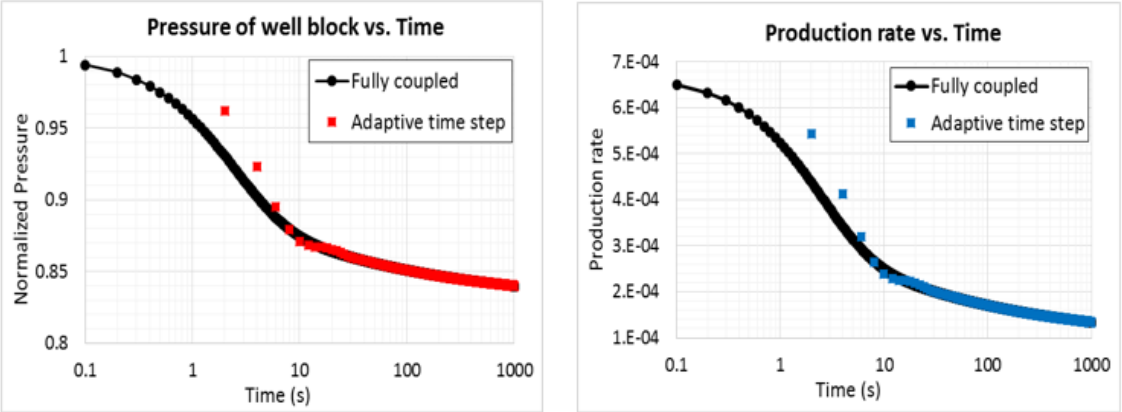

Figure 37: Comparison of results of pressure and production rate at larger initial time step size.

The accuracy of adaptive time step method has been already validated by comparing with the results of the fully coupled mode on Fig. 34 and 35. Next, we will investigate how much computing time the adaptive time step method can save when compared with the regular sequential method and the fully coupled method. Fig. 38 compares the results of computing time and the iteration number among the adaptive time step method, the regular sequential method, and the fully coupled method. For the fully coupled method, the total computing time is 17,319 seconds for 10000 steps running. For the regular sequential method, the total computing time is 11,806 seconds for 10000 steps running. For the adaptive time step method, the total computing time is only 481 seconds for 326 steps running. Apparently, when the adaptive time step is used, the computing time is significantly reduced, and the iteration number is considerably decreased because of the automatic adaptation of time step size. The regular sequential method can also save about one third time when compared with the fully coupled method. On the other hand, when the grid number of mesh becomes larger, the sequential method will save the

computing time more and more than the fully coupled method. This is mainly because a large grid number (huge node number) will form a significantly large matrix for the fully coupled model, which certainly consumes high computing time.

To sum up, the adaptive time step method needs extremely less computation time than the regular sequential method, and the regular sequential method consumes much less computation time than the fully coupled method. This is a major advantage and motivation about why we choose to apply the adaptive time step for the coupled problems. By the way, the local error method, which is proposed in the study of this chapter and described on Fig. 32, is temporarily designed only for the sequential coupled models, because the sequential coupled approach is more efficiency than the fully coupled method. However, the local error method is absolutely available for the fully coupled model, while the procedures just need to be modified. In this study, the sequential coupled model is applied for various reservoir applications. Furthermore, the main objective of this chapter is to demonstrate the computational efficiency is significantly improved when the adaptive time-step method is used for the sequential coupled method. Therefore, this is why we only showed the results from three different cases on Fig. 38, while the results from the fully coupled case with the local error method was not displayed.

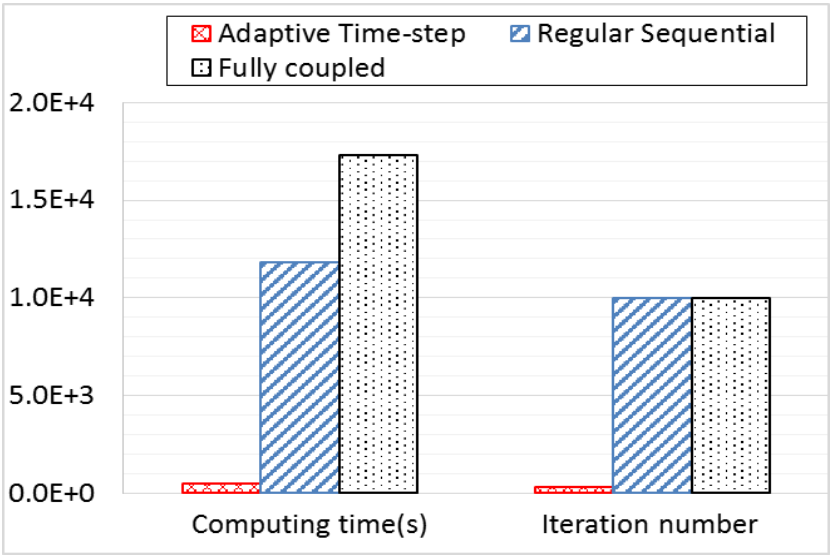

Figure 38: Comparison of computing time and iteration number.

On Fig. 39, the total number of time steps are presented for different error tolerances of displacements (ε_u). For the 2D coupled model above, the default ε_u is 5×10^{-3}, and the final total step number is 326. When ε_u is changed from 1×10^{-3} to 1×10^{-2}, the total step number decreases. As we see on Fig. 39, the curve's trend is nonlinear, and the required total step number will be significantly increased if the error tolerance of displacement becomes very small. On the other hand, Fig. 40 shows the results of total simulation time for different error tolerances of displacement. The change trend of total time is similar with the change trend of total number of step. When a tiny error tolerance of displacement is used, a much large computing time is required because much more iterations of calculation are needed. However, the bottom line is, no matter how small the ε_u is, the total number of step from the adaptive time step method is always much less than that from the fixed time-step size scheme. On the other hand, even though a large ε_u could largely reduce the computing steps, it will lead to large numerical error and less

accurate solution. Therefore, to choose an appropriate error tolerance, which could both save computing time and maintain the accuracy, plays a critical role on optimizing the application of the modified local error method for the coupled model.

Fig. 41 displays the size of time step changes along with the number of time steps for different error tolerances of displacement. Three different values of error tolerance are chosen: $1 \times 10^{-3}, 5 \times 10^{-3}\ (default), 20 \times 10^{-3}$. Obviously, when the error tolerance is smaller, the time-step size need to be reduced more in order to satisfy the more accurate error criteria. Among all the three numerical cases, the time-step size stays in a low value range for a while until the pressure change and displacement change of reservoir becomes small. In addition, if the time-step size need to be reduced or not is highly dependent on the initial time-step size. If the initial time-step size is considerably small, there is no need to cut the time step. Typically, the maximum time-step size for the flow equations could be derived from von Neumann stability analysis, and the result should be limited by both grid block size and properties of fluid and rock. Eq. (50) presents an example of the stability requirement for the explicit formulation of one-dimensional single phase flow system.

$$\Delta t \leq \frac{1}{2}\left(\frac{\phi \mu c_f}{k}\right)(\Delta x)^2 \tag{50}$$

Therefore, the recommended procedures for how to choose an appropriate error tolerance for the coupled problem are described as follows. Firstly, obtain the max time-step size by using von Neumann stability analysis. Secondly, divide the max time-step size by ten as the initial time-step size we will use for the coupled model. Thirdly, apply the default error tolerance (5×10^{-3}) and run the coupled program with the modified local

error method. Finally, plot the results of the size of time step. If the time-step size is enlarged at the beginning, choose the five times smaller error tolerance and run the coupled program again. Inversely, if the time-step size is largely reduced at the early stage, but then it is increased at the later stage, choose and apply that error tolerance for the coupled model. That is the approximate error tolerance we need for the adaptive time stepping method.

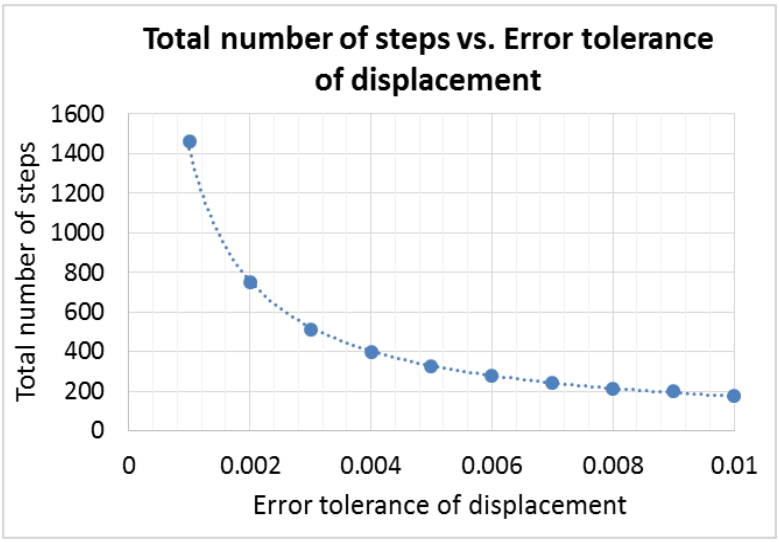

Figure 39: Total number of steps for different error tolerances of displacement.

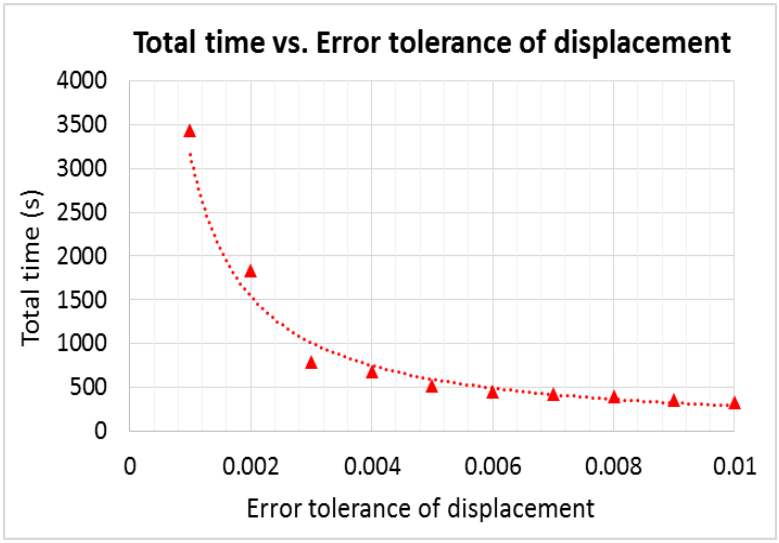

Figure 40: Total simulation time for different error tolerances of displacement.

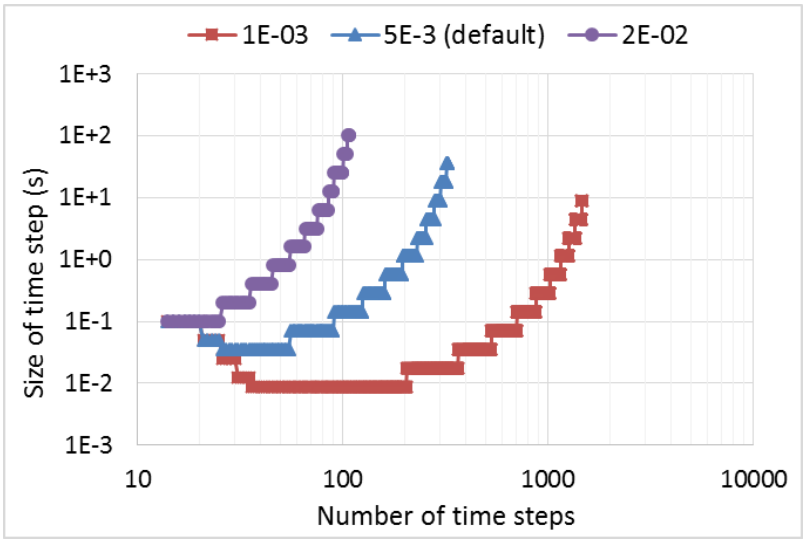

Figure 41: The change of size of time step for different error tolerances of displacement.

4.4 Conclusions and Discussions

An adaptive time stepping method with the modified local error approach is introduced to improve the computational efficiency and reduce iteration time for the coupled flow-geomechanics problems. A synthetic two-dimensional coupled production problem is introduced to apply the modified local error method, where the pressure and displacement change are presented at each time step. The numerical results of adaptive time step method show a very good match with the results from the regular sequential method and the fully coupled method, which verifies its accuracy. The required computing time and total iteration number for adaptive time step method is significantly less than that of regular sequential method and fully coupled method, which shows its computational efficiency. Since the change of pressure and displacement mainly occurred in the early stage of this production problem, the step size was firstly reduced for a while and then it was kept being increased. To ensure the accuracy of numerical results, regular reservoir simulators usually start with a small constant time step, even though it takes a long computing time. Apparently, that small time step is not the most efficient time-step size for the entire flow process in terms of computational efficiency. Therefore, if this adaptive time step method is implemented, the step size can be automatically adapted based on the change of displacement, which is a major advantage, especially for the cases with low truncation error requirement and tiny initial time-step size. For example, at the late stage of the coupled production problem, the small step-size is not required because the pressure change becomes relative tiny at each time step, so the step-size can be enlarged to save the computing time without sacrificing the accuracy.

When the step size is changed is highly depending on the error tolerance of displacement. The small error tolerance can provide a very accurate solution while it needs very small time step-size and takes more computing steps. On the other side, the large error tolerance only requires less computing steps while the accuracy is not guaranteed. Therefore, choosing a proper error tolerance is really important to optimize the time step size for the modified local error method. Since no specific technique can be employed to find the optimal error tolerance so far, trial and error method is probably needed. By using von Neumann stability analysis, the maximum step-size can be obtained. To start with a recommended error tolerance 5×10^{-3} and a small time step-size, the coupled program is performed and the results of time step size are plotted. By checking whether the initial time step is still largely reduced or not, we can determine if the recommended error tolerance is required to be modified. To start a significant small error tolerance is always recommended for the modified local error method. This is because even though the much small error tolerance is used, the total computing time will be still much less than the total time from the fully coupled and the regular sequential method. Meanwhile, the accuracy is also maintained.

In addition, how to modify the step size also plays an important role in the stability and computational efficiency for this modified local error method. For example, when the step size needs to be reduced, to choose divide by 2 or $\sqrt{2}$ could make a large difference. A large increase or decrease on one-step size could bring the oscillation effects. On the other hand, if the relative small coefficients are chosen, the step-size will be not effectively adjusted, which in return leads to low computational efficiency. Therefore, it is important

to find a balance between computational efficiency and oscillation effects, or choose an approach based on the priority of the project. Finally, even though the very simplest model (single-phase flow, linear elasticity, and backward-Euler method) was chosen to demonstrate this adaptive time step method in the study of this chapter, this technique is definitely flexible to be implemented to more sophisticated coupled problems, large-scale or three-dimensional model, where to reduce the computing time is always highly demanded.

CHAPTER V

GULF OF MEXICO DEEPWATER COMPACTION EFFECTS

5.1 Introduction

Reservoir compaction effects have caused considerably permeability loss and production decline for Gulf of Mexico (GOM) Deepwater turbidite reservoirs. Additionally, the permeability reduction derived from Pressure Transient Analysis (PTA) appears more severe than the permeability loss measured from core samples. Based on the provided laboratory and field data from one GOM Deepwater reservoir operator, this study presents a comparison between laboratory-measured and field-derived permeability decline under compaction effects. Additionally, irreversible compressibility and permeability hysteresis are proposed to explain the difference with the support of simulation results. The main procedures for the study in this chapter are described as follows.

Firstly, all the available laboratory data are analyzed, which include rock compressibility, thin section micrographs data, rock mineralogy, core-measured porosity and permeability at various effective stresses. Secondly, well buildup pressure tests are built to display the permeability results derived from different permeability correlations. Thirdly, history matching Bottom Hole Pressure (BHP) are conducted to show the difference of derived permeability among three cases with different compaction tables. Fourthly, the Brugge offshore field simulations have been developed to show the impacts of different compaction tables on the cumulative production. Different operating scenarios

in terms of bottom hole pressure, maximum production rate, and well shut-in period, are also investigated to provide practical recommendations for minimizing compaction issues.

The main objectives of this study could be mainly divided as: a) analyze existing laboratory data and field data to better understand the processes of dynamic formation compaction within Gulf of Mexico Deepwater turbidite reservoirs; b) explain the difference between the laboratory-measured and field-evaluated permeability loss trends with the rock compressibility hysteresis; c) build the coupled flow-geomechanics models with proposed compaction mechanism to validate and predict the compaction impacts on permeability decline and production performance; d) develop different operating scenarios with coupled geomechanics models to minimize formation compaction issues and provide recommendations for field operating strategies.

5.2 GOM Deepwater Reservoirs Overview

Field data provided by ENI are mainly from three different reservoirs, which locates in Green Canyon and Ewing Bank region of Gulf of Mexico (GOM). Due to the confidential agreement in terms of reservoir information, only some basic information is highlighted for the three different GOM Deepwater turbidite reservoirs on Table (7), and we called them as Reservoir A, Reservoir B, and Reservoir C for convenience. As on Table (7), a good range of reservoir information are shown, which includes hydrocarbon trapping mechanisms, water depth, formation depth, net sand thickness, initial porosity, initial water saturation, initial effective permeability, initial pore volume compressibility, initial effective net stress, and primary drive mechanism.

All of the three reservoir wells have cased-hole frac-pack completions, and their primary drive mechanism is compaction or depletion. Different with reservoir A and B, reservoir C has larger formation depth and initial effective stress, which in return leads to lower initial porosity and smaller initial pore volume compressibility. All of the three reservoirs have very high initial effective permeability and initial reservoir pore pressure. The high initial reservoir permeability is typical for many GOM reservoirs, while the quick decline is the difficult challenge to the production performance as well. The pre-production laboratory-measured pore volume compressibility and compactive permeability loss trend data have been obtained from core measurements.

For the reservoir A, core stress tests were performed on three core plugs. Air permeability has been measured by using the steady-state method at four different stress levels. Core porosity was determined by using the Boyle's Law method with helium. Additionally, some permeability data were obtained from the field data by using the Pressure Transient Analysis (PTA) method. For the reservoir B, hydrostatic pore volume compressibility was measured on six core plugs at eight stress levels, air permeability measurements were performed on four core plugs at eight stress levels, and absolute brine permeability measurements were conducted on two core plugs at eight stress levels as well. For the reservoir C, three core plugs were analyzed at seven stress levels by using the effective stress method and oil permeability measurements in laboratory.

Based on permanent DHPT gauges installed downhole, field-measured compaction permeability data was obtained from pressure transient analysis of a series of well buildup tests. The buildup tests were performed by using standardized shut-in

procedures and data-recording frequency to allow consistency of PTA evaluation over well life, which provides skin, the product of permeability and thickness, and reservoir pressure at various times.

Fig. 42 compares the field-evaluated and core-measured permeability loss trends for reservoir A. The lab-measured permeability data was from three core plugs, and the field-evaluated permeability data is from Pressure Transient Analysis (PTA) of a series of well buildup tests. The core samples of reservoir A were ideal candidates to investigate the compaction effects on rock properties, because no aquifer influx existed. On the x axis, net effective stress is defined as overburden pressure minus reservoir pore pressure. On the y axis, the permeability reduction factor is defined as the ratio of permeability at any pore pressure to the initial formation permeability, which is between zero to one. The solid curves stand for the permeability from core measurements, which are sort of different with each other on Fig. 42. The blue dash curve represents the trend of permeability reduction estimated from PTA. The comparison shows the permeability reduction estimated from PTA is much severe than the permeability loss from core measurements. For a certain pressure drop from initial reservoir pressure, the permeability derived from PTA is much smaller than the permeability measured from core samples.

Fig. 43 presents the comparison of field-evaluated and lab-measured compactive permeability loss trends for reservoir B. Both air and brine permeability measurements were conducted, and their values vary significantly. The blue and orange solid line stand for the permeability measured with brine as the flowing fluid, and the green solid line represents the permeability measured with air as the flowing phase. The results of air

permeability show a consistently less permeability loss than the results of brine permeability. The brine-measured permeability loss trend is very close to the permeability from PTA at low net effective stress. The permeability data estimated from PTA were obtained from three different producing wells. Field-evaluated permeability loss trends present similar behavior for the three different wells. The permeability estimated from PTA show more reduction than the results from core plugs, especially at high net effective stress.

The results from reservoir A and B are just two examples selected to display both the obvious permeability decline trend and the large difference between core-measured and PTA-derived permeability data. More data from other GOM fields including reservoir C show the similar trend, but they are just not displayed in here. As what we have already shown on Fig. 5, the generalized permeability loss trend derived from PTA is much severer than the permeability loss trend measured from core tests in the laboratory, which generally agrees with the published data by Chevron for their Deepwater GOM Genesis field (Pourciau et al., 2005). Therefore, it is critical to figure out why the permeability results are different from these two different methods and how to correctly predict the real permeability decline caused by compaction impacts for the Gulf of Mexico unconsolidated reservoirs.

Table 7: Description of GOM Deepwater turbidite reservoir sands.

	Reservoir A	**Reservoir B**	**Reservoir C**
Trapping mechanisms	Structural faulting and stratigraphic	Stratigraphic with localized faulting	Subsalt in three-way fault closures
Water depth (ft)	3,300	1,700	3,900
Formation depth (ft)	13,445	14,650	25,700
Net Sand thickness (ft)	96	74	156
Initial porosity	0.33	0.32	0.23
Initial water saturation	0.21	0.18	0.39
Initial effective permeability (md)	700	1,180	765
Initial pore volume compressibility (microsip)	45	30	2
Initial effective net stress (psi)	1,830	2,600	8,400
Primary drive mechanism	Compaction / depletion	Compaction / depletion	Compaction / depletion

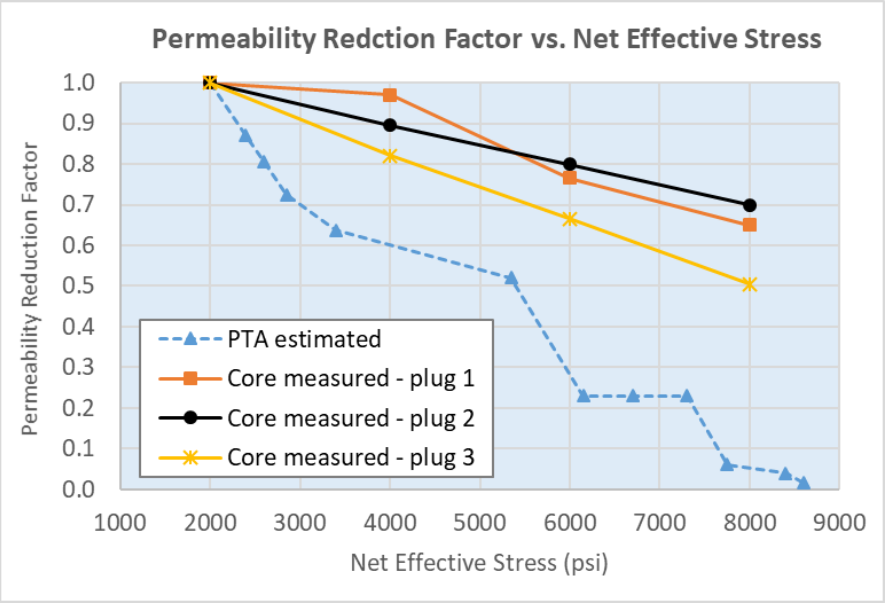

Figure 42: Comparison of field-evaluated and lab-measured compactive permeability loss trends for reservoir A.

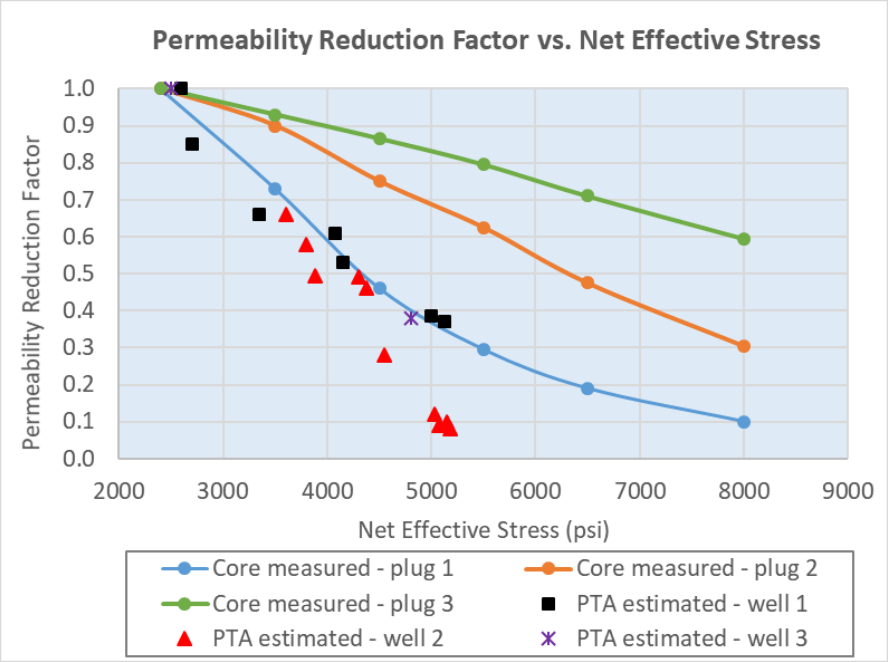

Figure 43: Comparison of field-evaluated and lab-measured compactive permeability loss trends for reservoir B.

5.3 Rock Compressibility Hysteresis

Reservoir rock is subjected to both internal fluid pressure and external overburden stress. With the depletion of fluids from reservoir, the pore pressure is reduced which in return leads to an increase of effective stress. This stress change results in changes in the matrix volume, pore volume, and bulk volume of rock. Compressibility is generally defined as the relative volume change of matter per unit pressure under isothermal condition. Three types of rock compressibility are typically mentioned in literature: matrix compressibility, pore compressibility, and bulk compressibility. However, since pore compressibility is much larger than matrix compressibility and the change of pore volume is a major interest to reservoir engineer, pore compressibility is typically the only compressibility what we usually talk about to investigate the relative change of rock volume under stress change, which is usually referred to as formation compressibility as shown on Eq. (51). Formation compressibility can be determined in laboratory. The porosity and permeability change can be predicted from formation compressibility. Eq. (52) and (53) are one example of empirical equations to calculate the porosity and permeability change from pressure p_1 to p_2 (Espinoza 1983).

$$C_f = \frac{1}{V_p}\left(\frac{\partial V_p}{\partial p}\right) \tag{51}$$

$$\phi_2 = \phi_1[1 + C_f(p_2 - p_1)] \tag{52}$$

$$k_2 = k_1\left(\frac{\phi_2}{\phi_1}\right)^m \left(\frac{1-\phi_1}{1-\phi_2}\right)^2 \tag{53}$$

where C_f is formation compressibility, V_p stands for pore volume, p represents pore pressure, ϕ is rock porosity, k stands for permeability, m is an adjustable parameter depending on the rock type, which is around 3.5 for unconsolidated sands.

Compressibility is a function of the rock composition, depositional history, and rock porosity, which is often measured in laboratory, such as the uniaxial strain compaction tests. The value of formation compressibility is highly related to rock behaviors under compaction stress as well. Fig. 44 shows various rock mechanics behaviors under compaction effect, such as grain rotation, grain deformation, and breakage. Due to these compaction behaviors largely depend on the stress stage, rock compressibility is a function of stress. The change of pore volume compressibility along with pressure change have been extensively demonstrated in literature (Fatt 1958 and Brace 1965). Based on the provided measurement results from laboratory, Fig. 45 displays rock pore compressibility and bulk compressibility profiles during depletion measured from core samples.

Compared to pore compressibility, bulk compressibility did not change much during the around 6000 psi drop of reservoir pressure. Pore compressibility is decreased from $55 \times 10^{-6} \frac{1}{psi}$ at 6500 psi of reservoir pressure to around $29 \times 10^{-6} \frac{1}{psi}$ at 1500 psi, which is a 47.3% change. When pore compressibility is changed, the computing trend of porosity and permeability change is altered as well. Therefore, it is incorrect to simply use constant formation compressibility to predict the change of rock porosity and permeability during the reservoir depletion. Before the prediction, the pore compressibility should be measured at different stress levels from laboratory tests.

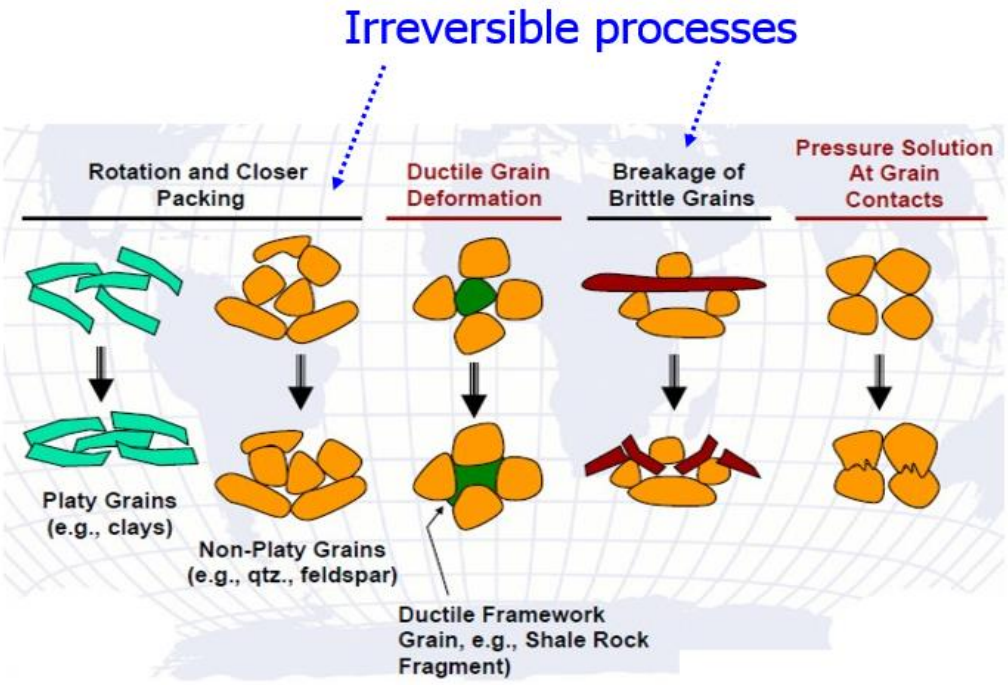

Figure 44: Various rock mechanics behaviors under compaction effect (modified from Jonas and McBride, 1977).

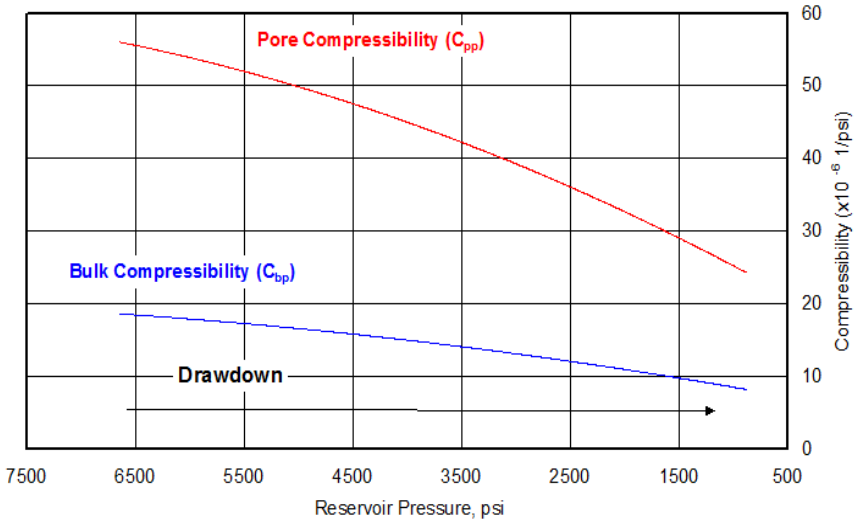

Figure 45: Rock compressibility profiles during depletion measured from core samples.

As shown on Fig. 44, some compaction behaviors are irreversible processes, which means they are permanent changes and they cannot go back to where they initially were. For example, if some brittle grains are broken down into small pieces under large compaction of effective stress, these small grain pieces will never be recovered into the original large piece, even though the high effective stress is removed later on. Fig. 46 displays the comparison of thin section micrographs before and after compaction effects. Both micrographs were obtained on the resolution of 500 micrometer. The left thin section micrograph was obtained before compaction, where the blue color represents the pore space within the rock. After compaction effects, the space of blue color (pore space) was clearly and largely reduced and in a non-uniform way.

In order to better investigate the compaction behaviors of pore space and grain particles, Fig. 47 presents thin section micrographs (A, B, C, D) of core sample from Ewing Bank at different resolutions. Micrograph A (top left image) is on the resolution of 500 micrometer, and micrograph B is on the resolution of 250 micrometer. Both micrograph C and D are on the resolution of 64 micrometer, which means more clear and accurate in a micro-scale. This core sample contains 27% total feldspars by thin section point count method, and 28% total feldspars by X-Ray Diffraction (XRD) analysis. Effective porosity appears as blue color because the sample were vacuum impregnated with blue epoxy before thin sections were cut. On the red dash circle of micrograph C (bottom left image), a collapsed orthoclase feldspar grain (F) along its cleavage planes is observed.

Similar collapse of feldspar is also observed on the bottom red dash circle of micrograph D. Additionally, on the upper red dash circle of micrograph D, a muscovite has been bent and ruptured by adjacent and harder grains, where a black solid arrow displays the direction of effective stress. These thin section micrographs show irreversible compaction processes have widely occurred within the pore structure under high compaction stress, which will in return change formation compressibility and affect the change trend of porosity and permeability. Even though the high compaction stress is removed from the core sample later on, the change of pore space and grain structures cannot be entirely restored to the original status.

The irreversible compaction processes result in the hysteresis effect on formation compressibility. The concept of hysteresis is used to describe the effects of path dependence and irreversibilities. The left image of Fig. 48 shows the schematic of rock compressibility hysteresis, where the compressibility change follows two different paths when the pore pressure is changed. For example, if reservoir pressure is reduced from initial condition, formation compressibility decreases. If reservoir pressure is then increased back to the initial pressure, formation compressibility does not increase all the way back to the initial value. This is because some permanent changes have happened during the compaction process, and they are not reversible. As shown on Eq. (53), the permeability change is related to the change of porosity and compressibility. Therefore, the permeability hysteresis could be derived from the hysteresis of formation compressibility, which is shown on the right image of Fig. 48.

Settari (2002) described the similar mechanism as well: when the compressive strength of rock is exceeded, plastic deformation occurs which leads to irreversible reduction of porosity and permeability. On the right image of Fig. 48, the permeability change follows two different paths when pore pressure is increased or decreased. At the same pore pressure, the permeability derived from reservoir depletion is higher than the permeability derived from well buildup process. Therefore, the reservoir permeability derived from well buildup test is smaller than the true permeability during reservoir depletion. Assuming that the core-measured permeability is the same with the reservoir permeability during depletion, there will be an obvious difference between the field-derived permeability and core-measured permeability. Overall, based on the observation of irreversible compaction processes, the permeability hysteresis is derived, which is then proposed to explain the difference between field-derived permeability and core-measured permeability. Above statement is mainly based on the theory derivation, while more field data and modeling results will be shown to support this proposal in the following section.

On the other hand, irreversible compaction processes do not happen at the entire compaction period, which depends on effective stress, pore volume, grain size and distribution, and core components. There is a general criterion for the occurrence of irreversible compaction in Deepwater unconsolidated reservoirs. Fig. 49 presents two different compaction phases observed from thin section micrographs of reservoir A and C, which are from Mississippi Canyon and Green Canyon of Gulf of Mexico reservoirs. The core sample from reservoir A has a rather larger pore volume and higher formation

compressibility than that of reservoir C. Blue zone stands for pore space, and the rest particles represent different rock components.

Along with the increase of net effective stress acted on core sample, the compaction process can be roughly divided into two processes: phase one consolidation and phase two deformation. During the phase one consolidation, the pore space is gradually compressed, and the interaction of grain particles are gradually converted from no-direct connection to point-point connection, and then to plane-plane connection. Irreversible compaction does not typically happen on the phase one consolidation period, where the main compaction behaviors are reversible. During the phase two deformation, there is not enough pore space to be compressed, which means the rock porosity will be not reduced too much. However, the primary plane-plane connection among particles will lead to some irreversible movements under high compaction stress, such as grain rotation, deformation, and breakage. Irreversible compaction mainly occurs at the phase two deformation period.

Due to large pore volume and rock compressibility, the sample of reservoir A will experience both the phase one and phase two compaction processes when the pore pressure is gradually decreased, and the compaction stress is gradually increased. However, the sample of reservoir C will mainly experience the phase two deformation period. That conclusion above observed from the thin section micrographs is pretty matched with the reservoir information shown on Table (7). Reservoir A has rather shallow formation depth and low initial effective stress, which indicates the phase two deformation process has not been started yet for the reservoir rock. Reservoir C has

significant deep formation depth and considerable initial effective stress, which indicates the phase one consolidation process has been already completed during the geological deposition. Whether to go through the phase two deformation process or not largely decides how many irreversible compaction behaviors will happen and how strong the formation compressibility and rock permeability hysteresis will be. Therefore, observing thin section micrographs of core sample is a good practical way to evaluate the future compaction behaviors and how strong the formation compressibility hysteresis will be, which in return correctly guides the prediction of permeability change along with the increase of net effective stress.

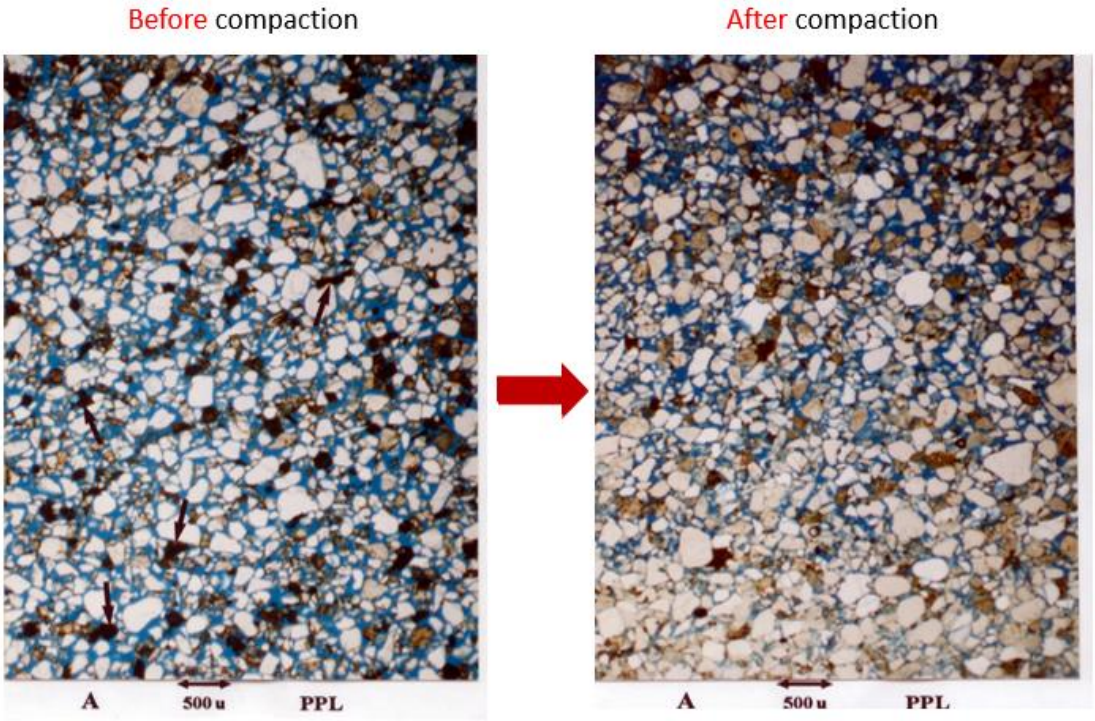

Figure 46: Comparison of thin section micrographs before and after compaction effects.

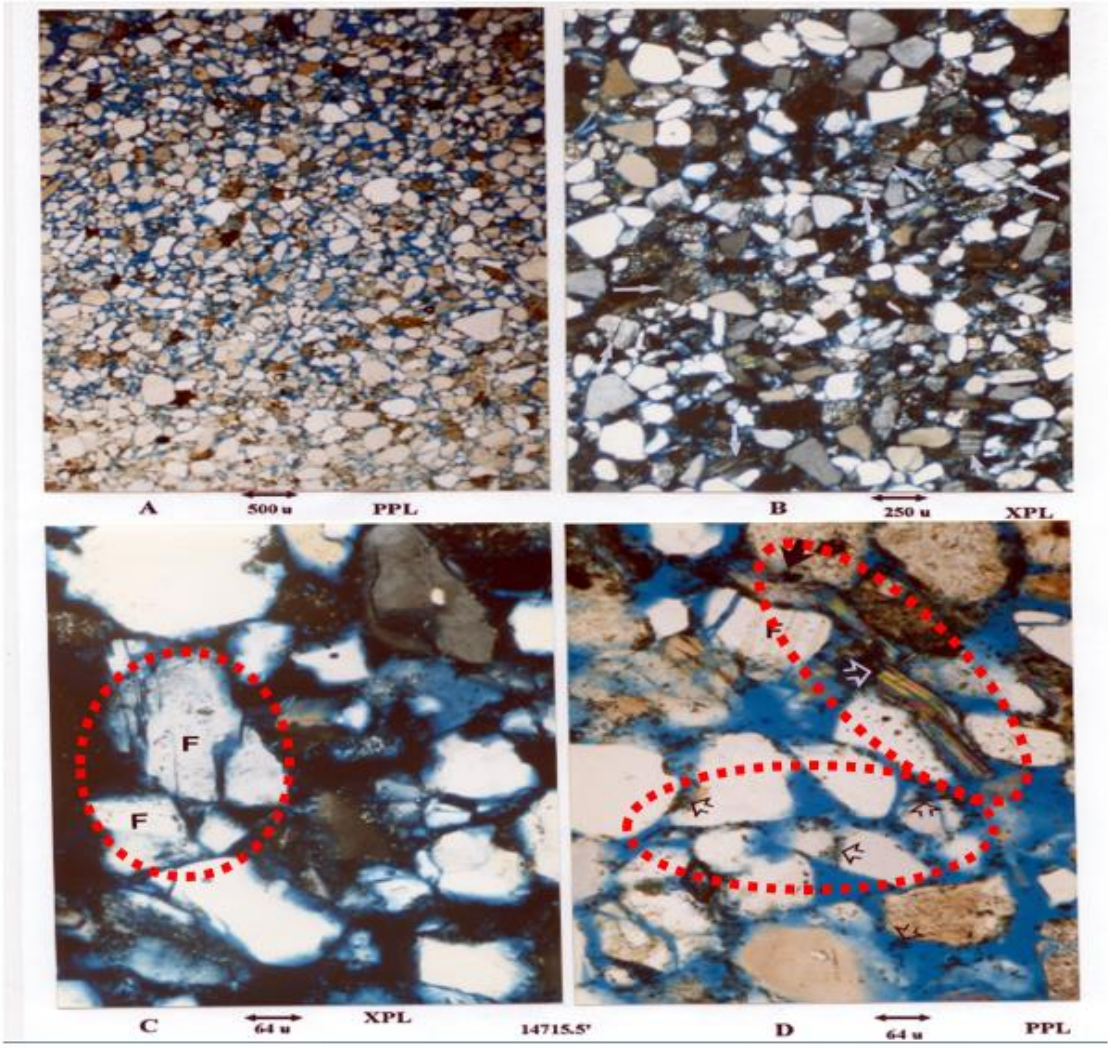

Figure 47: Thin section micrographs of core sample from Ewing Bank at different resolutions.

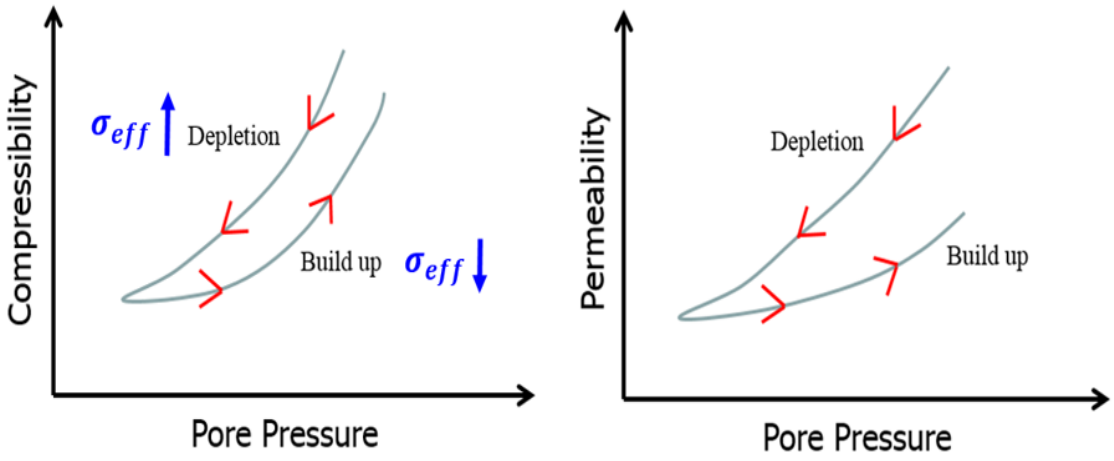

Figure 48: Schematics of rock compressibility hysteresis and permeability hysteresis.

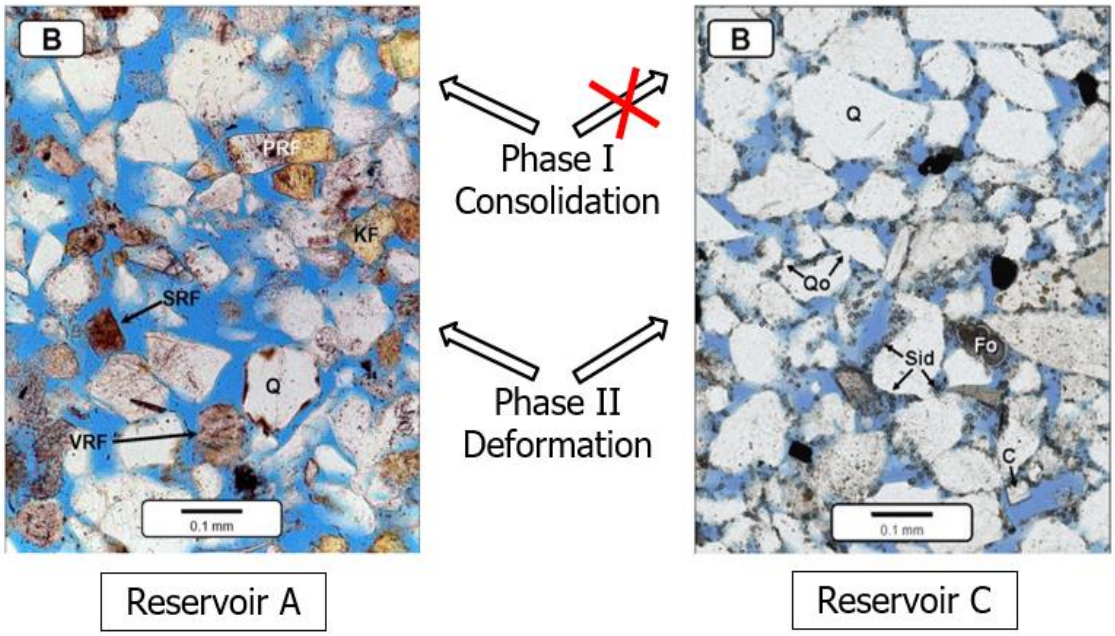

Figure 49: Two compaction phases observed from thin section micrographs.

5.4 Literature Experimental Data

Based on the observation of irreversible compaction behaviors from thin section micrographs, the pore compressibility and permeability hysteresis have been proposed and explained for the GOM Deepwater unconsolidated reservoirs in the previous section. Actually, the phenomenon of stress-dependent permeability hysteresis has been observed and demonstrated from experimental data for many reservoir rocks in literature (Warpinski and Teufel 1992; Norman et al. 2005; Liu et al. 2016; Wang et al. 2017). Before we show these literature experimental data evidences, let us firstly state the effective stress law we often used in this report. Terzaghi (1923) was the first to introduce the relationship of effective stress for soil analyses. Later, Biot (1941) derived the elasticity equations governing poroelastic behavior for calculating deformation. Effective stress law is usually described as Eq. (54) and (55). Biot coefficient α is typically close to one. In the study of this chapter, Biot coefficient is taken as one for all future explanation. Eq. (54) is used to calculate the net effective stress as on Fig. 42 and 43.

$$\sigma_e = \sigma - \alpha p \tag{54}$$

$$\alpha = 1 - \frac{K_d}{K_s} \tag{55}$$

Where σ_e is the effective stress, σ is the applied stress on the rock surface, p is the internal pore pressure, α is the poroelastic parameter which is also called Biot's coefficient, K_d is the dry rock bulk modulus, K_s is the mineral rock modulus.

Fig. 50 show the permeability measurement during loading and unloading cycles for low-permeability tight rocks from Warpinski and Teufel (1992), where the permeability hysteresis can be obviously observed. The x axis stands for net effective stress, and the y axis represents rock permeability on this plot. When net effective stress is increased from low starting point as the upper blue arrow shows, the permeability reduces. Then when net effective stress is decreased from 7000 psi to 400 psi, the permeability gradually increases. These two permeability change curves under stress loading and unloading follow different paths, and the rock permeability cannot be recovered to the initial value when the net effect stress came back to the original low point.

Assuming we take a certain net stress from the x axis of the plot, the permeability derived from the increasing stress (loading) path is larger than the permeability derived from the decreasing stress (unloading) path. The experimental results can be well explained by the irreversible compaction behaviors and permeability hysteresis theory. During the first loading processing, some irreversible compaction behaviors have already occurred, which results in the permeability difference between first loading and first unloading paths. However, during the second and third loading and unloading processes, the permeability hysteresis was not that obvious, because the core samples have been already compressed and not much new irreversible compaction behaviors happened.

Fig. 51 presents the core testing results of normalized permeability coefficient along with inferred reservoir pressure modified from Norman et al. 2005. The x axis stands for reservoir pressure, and the y axis represents normalized permeability coefficient, which is between zero and one. The blue arrows represent the changing direction of

effective stress. When reservoir pressure is decreased during reservoir depletion path, which means effective stress is increased, the permeability reduces. Then when reservoir pressure is increased as the re-pressurization path, the permeability does not rise much. The results from these experiments show the permeability loss caused by reservoir depletion is permanent, which cannot be recovered by the unloading path. In other words, during the reservoir depletion process, most compaction behaviors are irreversible, which we call the largest permeability hysteresis. Once the compaction process is completed, the drop permeability cannot be recovered. Therefore, to control the drawdown pressure during reservoir production is important for managing the compaction behaviors and stress-dependent permeability decline.

Fig. 52 shows the permeability changes along with the varying of confining pressure for two rock samples modified from Wang et al. 2017, where the mathematical models of fitting curves are also provided. One cycle experiment of loading stage (confining stress is increased) and unloading stage (confining stress is reduced) are performed for both core samples. Pore pressure was constant during these experiments, so the change of confining pressure can stand for the change of effective stress. The rock deformation caused by the increase of compaction stress is not elastic deformation, where the measured permeability is obviously path-dependent, and the permeability hysteresis is obvious observed.

The changing trend of permeability on Fig. 52 is quite similar with the results of Fig. 50, which will be used as references to model the permeability change during reservoir depletion and well shut-in for the following sections of this chapter. Based on

Eq. (54), both increasing confining stress and decreasing pore pressure can improve the net effective stress. Previously, Fig. 52 has already demonstrated the permeability hysteresis by changing the confining pressure. Actually, Liu et al. (2016) has conducted similar experiments to show the stress-dependent permeability by changing pore water pressure. On their experiments, confining pressure is constant and equal to 400 KPa. Pore pressure was firstly increased and then decreased for changing the net effective stress. An obvious permeability hysteresis was detected from the permeability data at different pore pressures. Based on the two experimental results above, the influence of different direction altering the net effect stress on the permeability hysteresis was excluded.

In this section, some experimental data were selected from literature to demonstrate and prove the existing of stress-dependent permeability hysteresis. The theory of irreversible compaction behaviors and pore compressibility hysteresis we observed and proposed in the previous sections, can perfectly explain these experimental permeability data. In the following sections of this chapter, the permeability hysteresis will be used with reservoir modeling to show its impact on the permeability derived from pressure transient analysis.

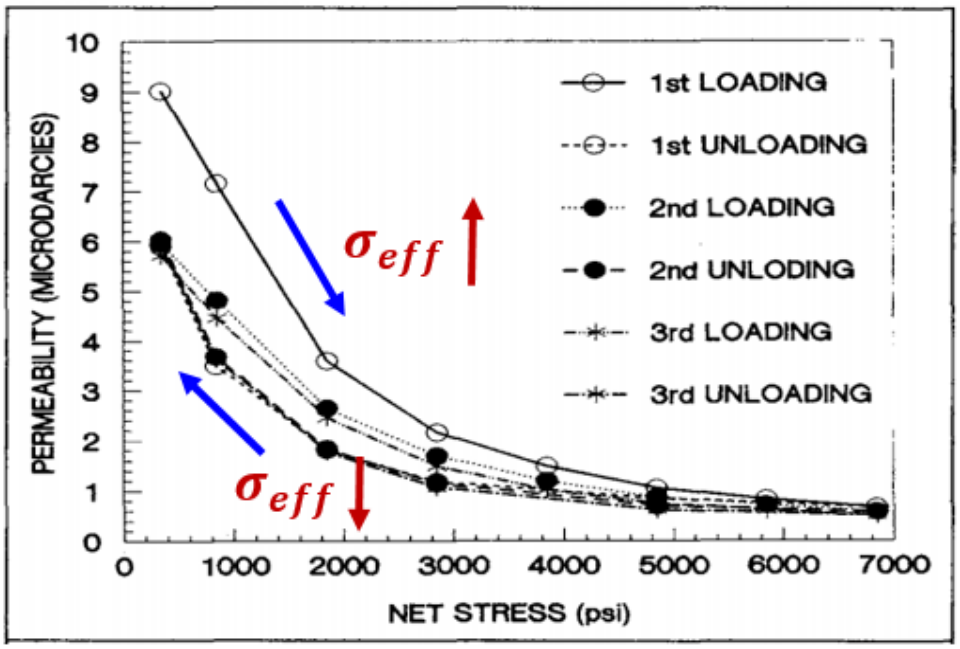

Figure 50: Permeability hysteresis and seasoning (modified from Warpinski and Teufel, 1992)

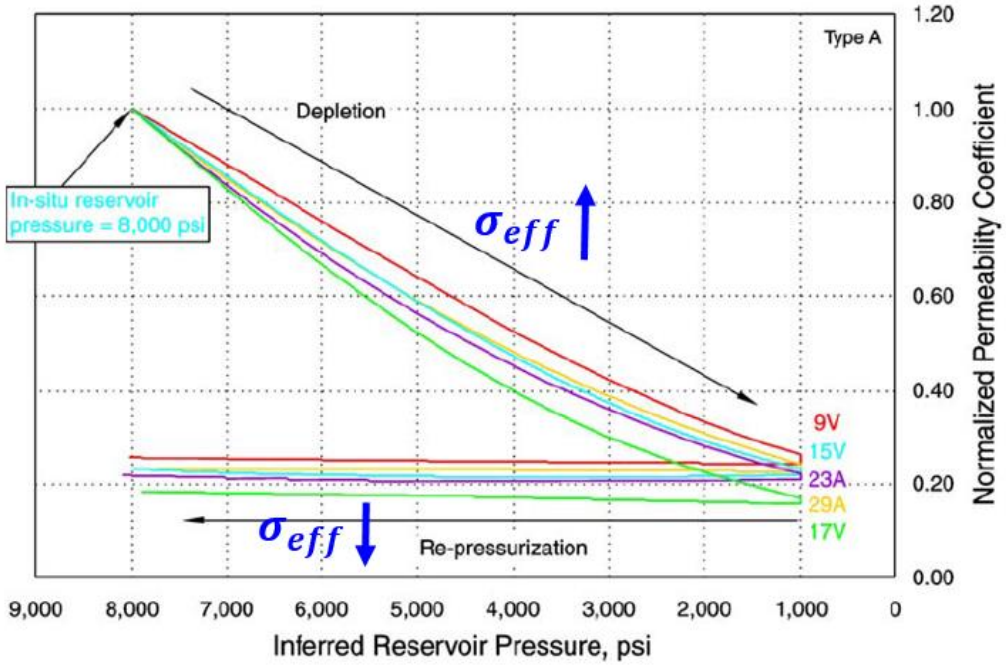

Figure 51: Core testing shows permeability hysteresis under compaction (modified from Norman et al. 2005).

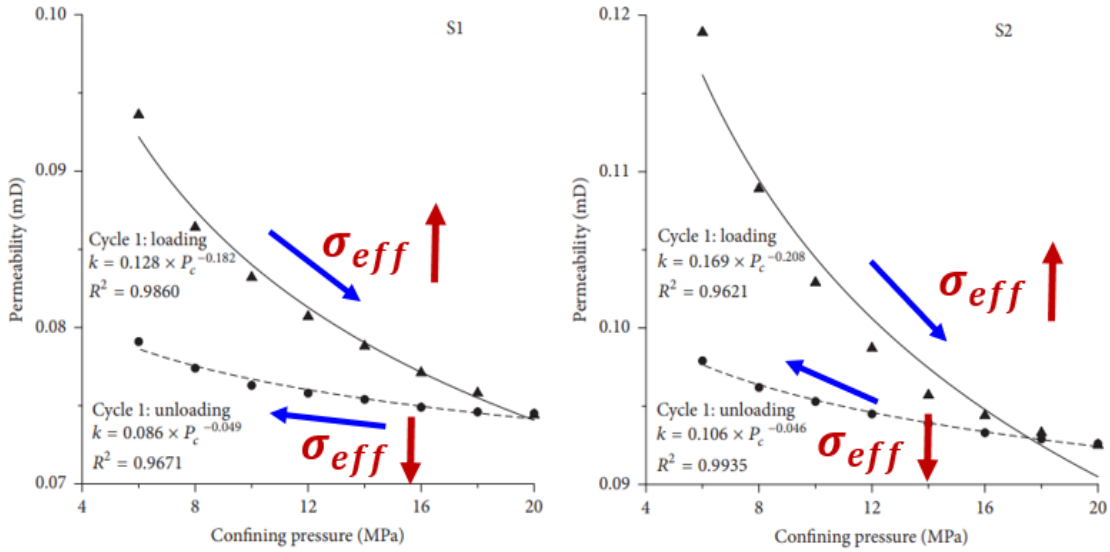

Figure 52: Fitting curves of permeability and confining pressure (modified from Wang et al. 2017).

5.5 Numerical Simulation Results and Analysis

5.5.1 Well Buildup Pressure Tests

A typical pressure buildup test was built with synthetic reservoir simulation. Fig. 53 shows the schematics of reservoir mesh for well buildup test, where a simple radial-grid mesh was built, a vertical production well is on the central of the reservoir mesh, and the color bar stands for reservoir pressure. Small grid size is designed for near wellbore zone in order to better describe transient flow process. As Fig. 54 presents, the production well was designed to firstly produce at constant flow rate $7000\ stb/day$ for 10 days (from August first to August tenth), and then the production well was shut in for one day to allow pressure to build up.

The initial input data for reservoir buildup test are displayed on Table (8). The initial reservoir permeability is 500 millidarcy (md), the initial reservoir pressure is 8000 psi, the total compressibility is $4.20 \times 10^{-6}\ 1/psi$, and the reservoir thickness is 9 ft. By running reservoir simulation with the provided initial reservoir condition, Bottom Hole Pressure (BHP) along with time is predicted and obtained. Next, the traditional Horner Plot method is used to interpret the obtained BHP for deriving reservoir permeability and skin factor. Two main equations of Horner plot method used in this section are shown on Eq. (56) and (57). More details about the Horner Plot method is referred to Dake (1978).

$$Horner\ ratio = \frac{t_p + \Delta t}{\Delta t} \tag{56}$$

$$k = \frac{162.6 \mu q B}{mh} \tag{57}$$

Where t_p denotes production time before shut-in, Δt stands for well shut in time, k represents reservoir permeability, μ is fluid viscosity, q denotes fluid production rate, B stands for formation volume factor, h represents formation thickness, m is the slope of the linear section of the buildup plot, unit in psi/log cycle.

To investigate the effects of permeability hysteresis on the result of field-derived permeability, three different cases of well buildup pressure test are conducted. The only difference among the three cases is about how the reservoir permeability will be treated: case 1) the permeability is assume constant; case 2) the permeability is stress-dependent and the permeability change is reversible along with the pressure change; case 3) the permeability change is irreversible along with the pressure change. Except for the different permeability correlations above, all other reservoir properties and initial condition are the

same for the three buildup cases. The numerical results will be analyzed by the Horner Plot method for the three different case, and the derived permeability will be compared among them.

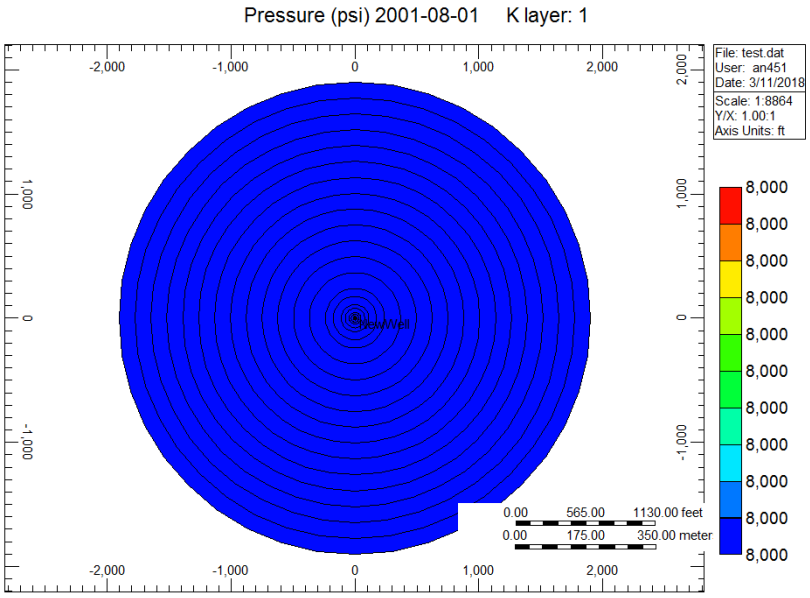

Figure 53: Schematic of reservoir mesh for well buildup test.

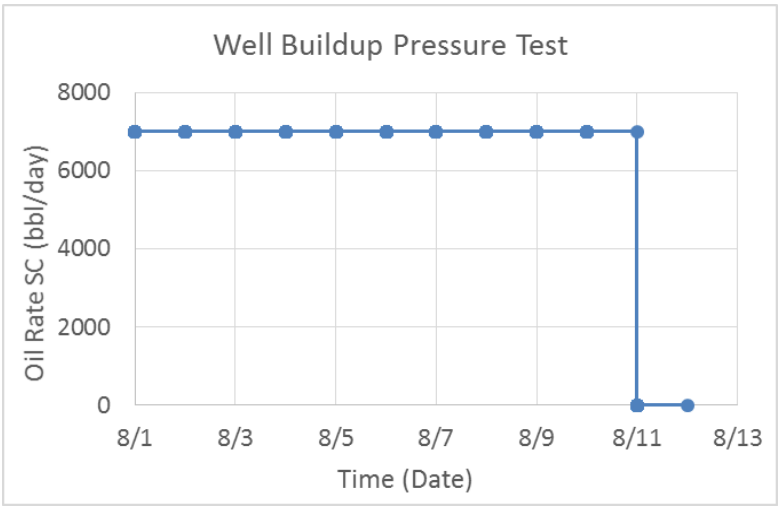

Figure 54: Oil rate schedule for well buildup test.

Table 8: Initial reservoir condition for well buildup test.

INPUT Data		
Q_oil	7000	stb/day
Height	9	ft
Initial pressure	8000	psi
Initial porosity	0.19	-
Initial permeability	500	md
Formation volume factor	1.07	rb/stb
Total compressibility	4.20E-06	1/psi
Well radius	0.375	ft
Viscosity	1.12E+00	cp

For the case one with constant porosity and permeability, the Bottom Hole Pressures (BHP) predicted from reservoir modeling are shown on Fig. 55, where x axis is time and y axis is pressure. BHP decreases along with time because of oil production, and then it rapidly increases after the well is shut in. By using Eq. (56) to calculate the Horner time ratio, the linear section of Horner plot is chosen and presented on Fig. 56, where the slope m and initial reservoir pressure can be obtained.

By using Eq. (57), the reservoir permeability is calculated and displayed on Table (9). Before running reservoir simulation, the initial reservoir permeability is 500 md shown on Table (8). After ten day's production and one day shut-in, the derived reservoir permeability is 502.7 md based on the Horner Plot method. The derived initial reservoir pressure (8003.9 psi) shown on Table (9) is quite close to the provided initial reservoir pressure (8000 psi). Both the derived reservoir permeability and initial reservoir pressure

validate the accuracy of reservoir simulation and Horner Plot method. Overall, if reservoir permeability does not change along with the pressure change, the permeability derived from bottom hole pressure with Horner Plot method is the same with the provided initial reservoir permeability.

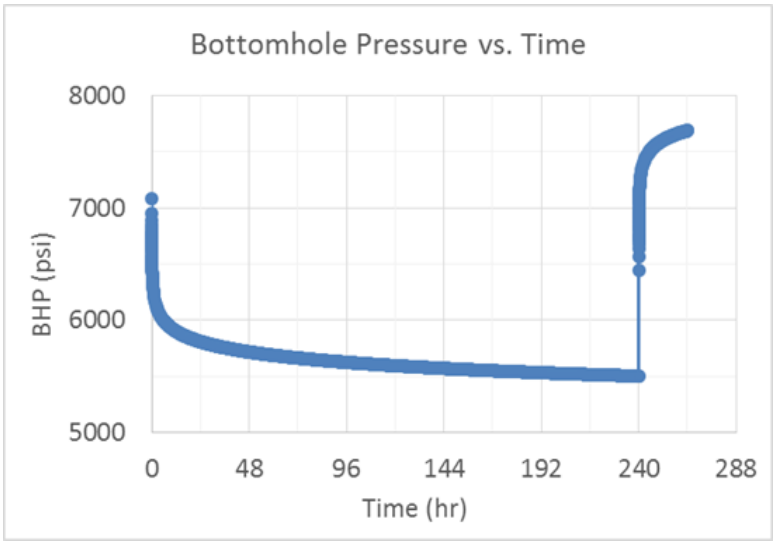

Figure 55: Bottom hole pressure produced from well buildup test.

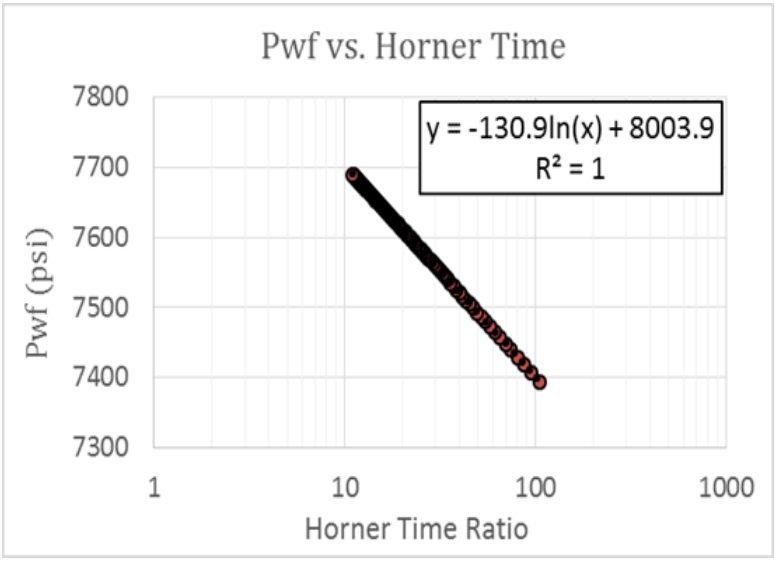

Figure 56: Bottom hole pressure along with Horner time ratio after well shut in.

Table 9: Reservoir permeability and initial pressure obtained from Horner Plot method.

PTA OUTPUT		
From LN fit on Horner Time Plot		
M	130.9	psi
Pi	8003.9	psi
M'	301.4	psi/cycle
K	502.7	md

For the case two, the permeability is stress dependent and the permeability change is reversible along with the pressure change. In other words, the permeability change follows the same curve path when the pressure is increased or decreased. Fig. 57 shows both porosity multiplier and permeability multiplier are changed along with pore pressure, where the multiplier is the ratio of current value to initial value. Therefore, the current permeability could be computed by multiplying initial permeability value with current permeability multiplier. The black arrows on Fig. 57 stand for the direction of pressure change. The stress-dependent porosity and permeability correlations on Fig. 57 are plotted based on an existing compaction table, where a porosity multiplier and permeability multiplier are provided at each certain stress level. For the rest of this chapter, we will use compaction table to represent the porosity and permeability change along with the pressure change.

Similar to the case one, Fig. 58 presents the results of bottom hole pressure along with time and Horner time ratio for case two. During the first ten day's oil production, the reservoir permeability is reduced along with the decline of reservoir pressure and the increase of effective stress. After the well is shut down, reservoir pressure is restored, which leads to an increase of reservoir permeability. Based on the Horner Plot method, the derived reservoir permeability is 465.7 md for case two, which is 7% smaller than the initial reservoir permeability (500 md). Additionally, the derived initial reservoir pressure is quite close to the original reservoir pressure as well.

For the case three, the permeability change is irreversible along with the pressure change, which means the permeability change follows different paths when the pressure is increased or decreased. To better show the difference between reversible permeability correlation and irreversible permeability correlation, we chose to use an extreme irreversible case: the porosity and permeability keep constant when the pressure is rebounded. Fig. 59 displays permeability multiplier changes along with pore pressure for case three. When pressure is reduced along with the black arrow, permeability multiplier follows the red curve. When pressure is increased later on, permeability multiplier stays constant and does not increase at all. The black and blue curves on Fig. 59 are two examples, which are largest permeability hysteresis.

Fig. 60 shows the results of bottom hole pressure along with time and Horner time ratio for case three. During the first ten day's oil production, the reservoir permeability is decreased along with the decline of reservoir pressure and the increase of compaction stress. However, after the well is shut down, the reservoir permeability keep constant when

reservoir pressure is rebounded, which is caused by irreversible compaction behaviors and permeability hysteresis. The reservoir permeability derived from Horner plot method for case three is 361.6 md, which is 27.7% smaller than the initial reservoir permeability.

The summary of derived rock permeability for the three different buildup tests are provided on Table (10). Comparing the three different cases, we found the permeability derived from Horner plot method is smaller when the stress-dependent permeability (compaction table) is considered. The case three with irreversible permeability change provides much smaller permeability than the case two with reversible permeability change. Therefore, if to consider the stress-dependent permeability or not plays an important role on the derived reservoir permeability. It is not wise to simply assume constant permeability without full study and investigation. One note is worthy to be pointed out: the permeability derived from buildup pressure and Horner plot method represents the average permeability of near wellbore zone, which stands for the flow conductivity from near wellbore reservoir zone to wellbore after well is shut-in.

Fig. 61 shows the pressure and permeability distribution at end of production time and before shut-in moment, where color bars stand for the value of pressure and permeability. The left figure is for reservoir pressure, which varies from 5215 psi to 8000 psi. The right figure is for reservoir permeability, which varies from 173 md to 500 md. Since the pressure is different at various locations of reservoir, the stress-dependent permeability is different at various reservoir locations. The closer to the wellbore, the lower to the reservoir pressure and permeability. However, the pressure buildup test only provides one average reservoir permeability derived from the Horner plot method.

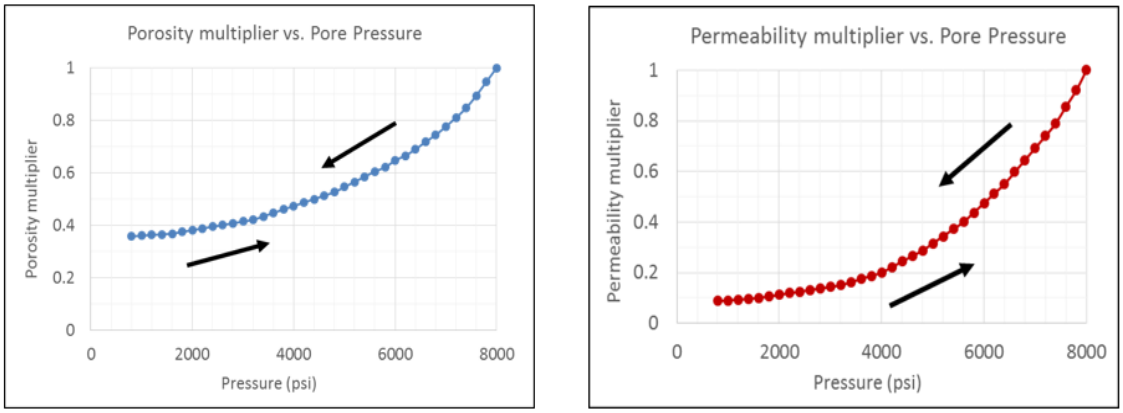

Figure 57: Porosity multiplier and permeability multiplier along with pore pressure for case two.

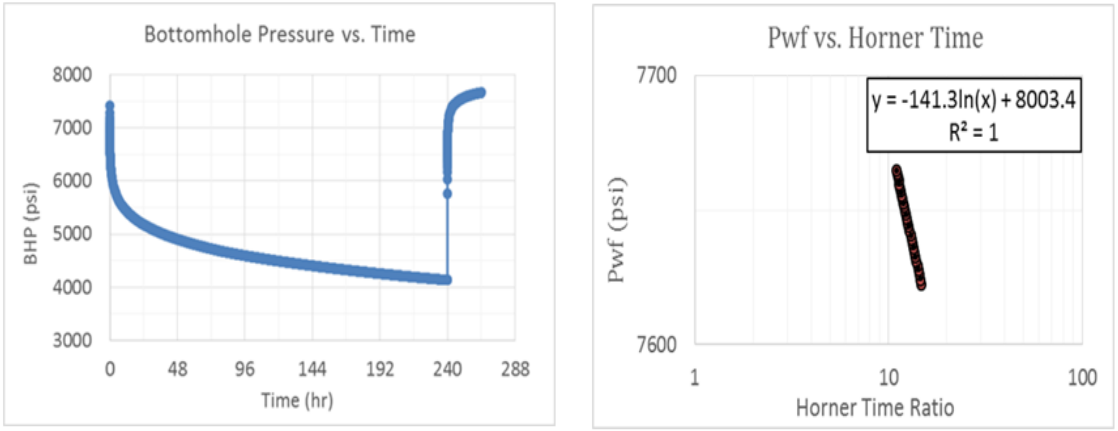

Figure 58: Bottom hole pressure along with time and Horner time ratio for case two.

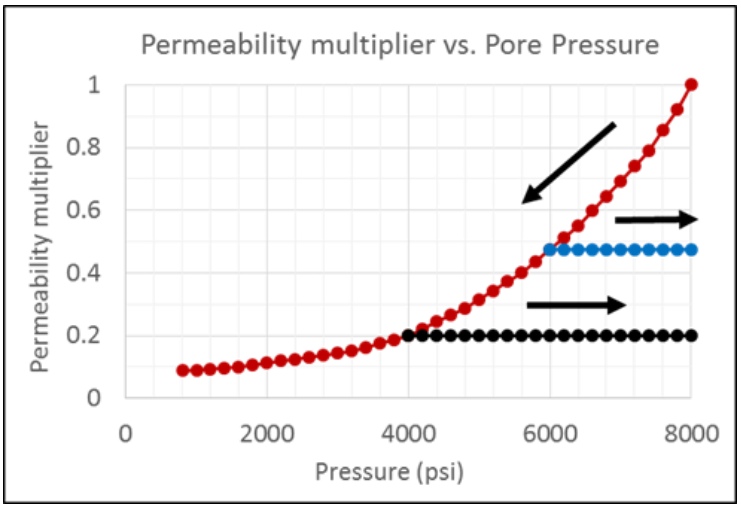

Figure 59: Permeability multiplier along with pore pressure for case three.

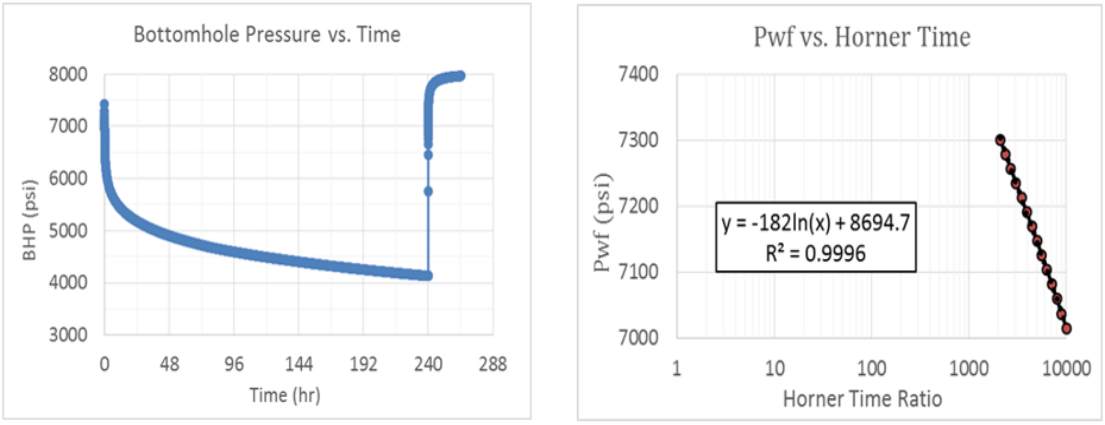

Figure 60: Bottom hole pressure along with time and Horner time ratio for case three.

Table 10: Summary of derived permeability from three buildup tests.

Constant rock compressibility	503 md
Reversible rock compressibility	466 md
Irreversible rock compressibility	362 md

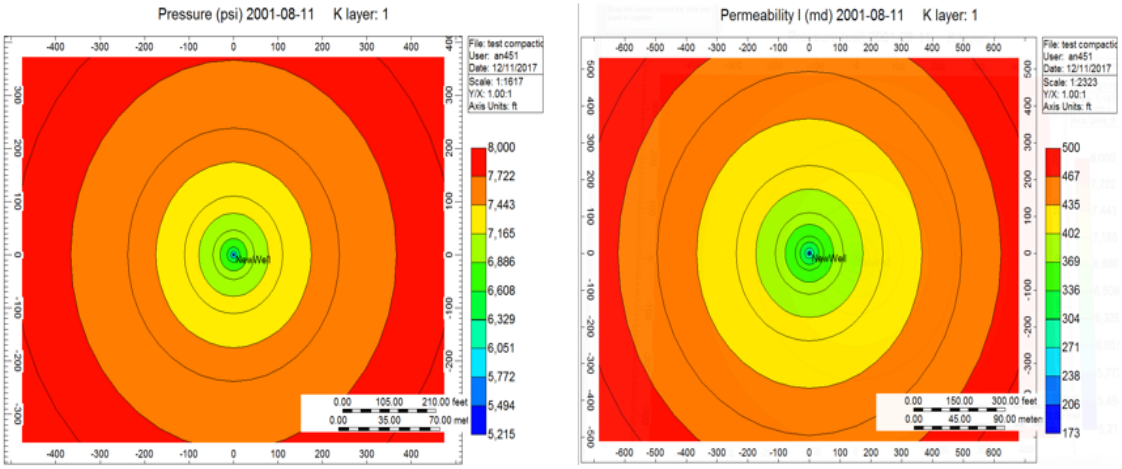

Figure 61: Pressure and permeability distribution at end of production time.

5.5.2 History Matching Bottom Hole Pressure

In this section, the reservoir models will be built based on the provided laboratory-measured and field-recorded data. History matching is a common approach to adjust reservoir model for reproducing the previous behavior of reservoir and increasing the

accuracy of reservoir simulation. The benefits of history matching include: improve and validate the reservoir simulation model, better understand the reservoir depletion processes, and recognize unusual operating conditions. Typically, in order to match the historical production and pressure data, the adjustments have to be made to the existing reservoir model. Meanwhile, these adjustments should be made under the consideration of geological and engineering consistent manner. The common adjusted parameters include aquifer size, reservoir permeability, and pay-zone thickness. In this section, we will mainly adjust reservoir permeability to match the historical bottom hole pressure data.

Fig. 62 shows the daily production rates of oil, gas, and water for three years from 2014 to 2017. The green curve stands for oil production, the red curve represents gas production, and the blue curve represents water production. The production rates of oil and gas were rapidly reduced during the first year, and they keep almost stable for the rest two years. Water start to be produced from October of 2015 to October of 2017. In addition to production data, some pressure results from buildup tests have been provided as well. Fig. 63 presents the historical data of Bottom Hole Pressure (BHP) from August to October of 2014, where the peaks stand for different buildup tests. Each buildup test is typically last one day. The BHP data during the buildup test around September 22 of 2014 are chosen for the numerical simulation of history matching, which is highlighted as red dash circle on Fig. 63. The time for the selected bottom hole pressure is from September 17 to September 23 of 2014, and the well shut-in was last about 22 hours.

Based on the provided production data and field data, reservoir modeling will be built, where the reservoir permeability will be adjusted to match the historical bottom hole

pressure data. Three different numerical cases will be built to match the same bottom hole pressure data: a) the reservoir permeability is assume constant; b) the permeability is stress-dependent and the permeability change is reversible along with the pressure change; c) the permeability change is irreversible along with the pressure change. Except for different permeability correlations above, all other reservoir properties and initial conditions are the same for the reservoir modeling of history matching. Based on the same bottom hole pressure, the permeability results derived from different numerical cases will be compared and analyzed.

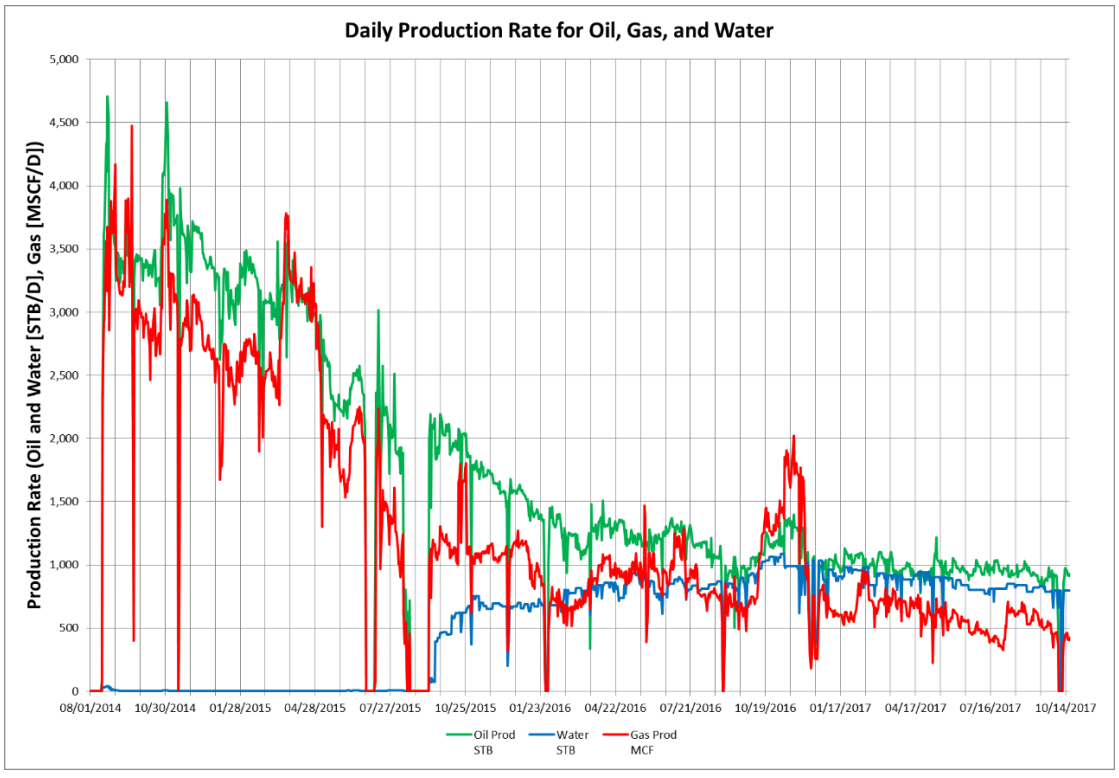

Figure 62: Daily production rates of oil, gas, and water for three years.

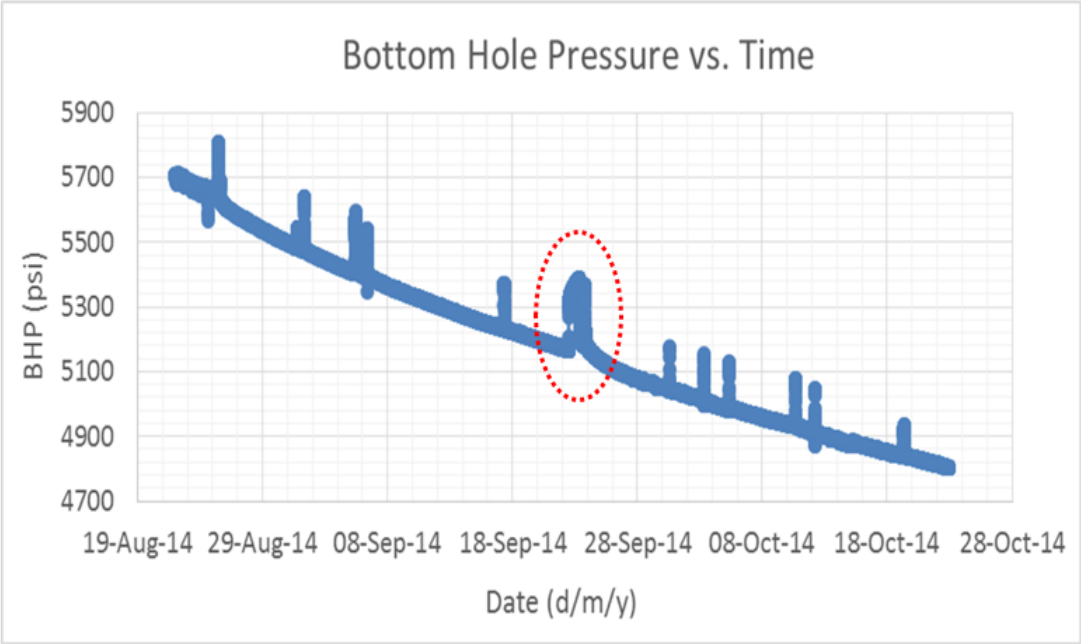

Figure 63: Bottom hole pressure along with time for a series of build-up tests.

As a critical part of reservoir model, PVT properties are required to evaluate the composition, phase behavior, and transport properties of reservoir fluid. Table (11) presents the summary of PVT data measured from core samples, where constant composition expansion and differential vaporization tests are conducted. The PVT table includes oil volume factor, oil viscosity, gas volume factor, gas-oil ratio, gas viscosity, and oil compressibility at different pressure levels. At the reservoir temperature of 149°F, the measured bubble point pressure was 4219 psia. The reservoir fluid viscosity was measured to be 1.56 cp at the reservoir condition, where the reservoir pressure was 6849 psia. The modeling time is settled as the same with the selected build up test: from September 17 to September 23 of 2014. Due to production rates are provided as daily base

and big difference exists among the production rates during these selected days, an average production rate is used as input for the reservoir modeling.

For the case one with the constant permeability, Fig. 64 shows the results of Bottom Hole Pressure (BHP) along with time, where x axis is time and y axis is well bottom hole pressure. The blue points are gauge-recorded BHP data from Gulf of Mexico reservoir field, and the red curve stands for the BHP results produced from reservoir simulation. The objective is to history match the BHP data from simulation with the gauge-recorded BHP by adjusting the reservoir permeability. More importantly, for this history matching, to match the BHP data after well shut-in (September 22) is much more significant than the data match before well shut-in. This is because it is the BHP data during reservoir buildup period (after well shut-in) that will be used to derive the reservoir permeability from Pressure Transient Analysis (PTA). Therefore, the priority is to match the BHP data during reservoir build up. On Fig. 64, the BHP data from reservoir modeling are well matched with the BHP from field-recorded, especially for the period after well shut-in. The reservoir permeability derived from the history matching BHP is 380 md for the case one with constant permeability.

Table 11: Summary of PVT measurements on core samples.

Pressure (psi)	Oil volume factor (bbl/STB)	Oil viscosity (cp)	Gas volume factor (RCF/SCF)	Gas-oil ratio (SCF/STB)	Gas viscosity (cp)	Oil compressibility ($* 10^{-6}$ 1/psia)
14.7	1.037	8	1.1639	0	0.00751	
515	1.116	3.73	0.0314	160	0.0117	
1115	1.162	3.04	0.0137	256	0.01364	
1615	1.197	2.4	0.0091	334	0.01518	
2115	1.224	2.1	0.0069	416	0.01678	
2615	1.262	1.8	0.0056	504	0.01855	
3115	1.296	1.59	0.0048	599	0.02044	
3615	1.332	1.38	0.0042	694	0.02249	
4219	1.388	1.28		823		10.64
4315	1.386	1.29				10.48
4517	1.383	1.31				10.15
5020	1.377	1.36				9.44
6025	1.364	1.47				8.34
6849	1.355	1.56				7.67
8017	1.344	1.7				6.95

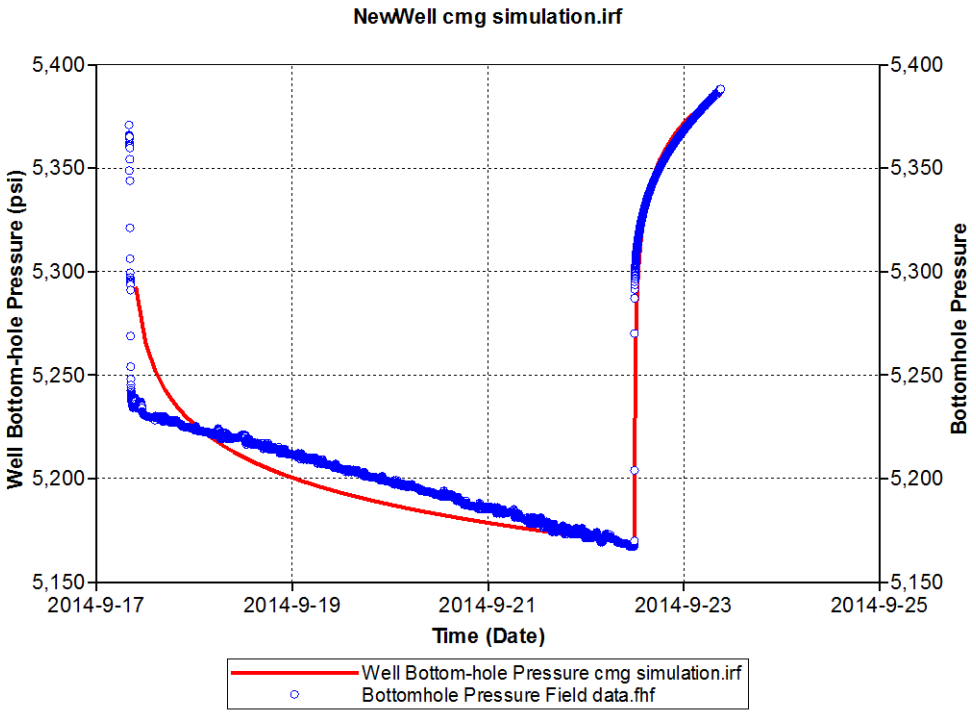

Figure 64: History matching bottom hole pressure for the case of constant permeability.

Fig. 65 shows the results of history matching Bottom Hole Pressure (BHP) for the case two with the reversible stress-dependent permeability. The permeability is stress-dependent and the permeability change follows the same path no matter the pressure is increased or decreased, which is similar with the right curve of Fig. 57. The procedures, objective, and priority of the case two are the same with the case one above. By matching the gauged-recorded BHP (especially for the pressure after well shut-in), the derived reservoir permeability is 420 md. When the reversible stress-dependent permeability is considered, the BHP data before well shut-in is better matched than the case of constant permeability by comparing Fig. 64 and 65.

On the other hand, in order to obtain a good enough match for the BHP after well shut-in, the permeability of near wellbore zone has been adjusted. This adjustment could be understood as consequence of skin effects, such as reservoir damage and formation fracturing, which are typically evaluated by a skin factor. The skin factor due to the presence of a zone of altered permeability near the wellbore is calculated by Eq. (58). For the case two with reversible stress-dependent permeability, the calculated skin factor is equal to -4.0, where negative value represents reservoir stimulation, an increase of formation permeability.

$$s = \left(\frac{k}{k_s} - 1\right) \ln\left(\frac{r_s}{r_w}\right) \tag{58}$$

Where s represents skin factor, k represents original formation permeability, k_s represents the permeability of damaged zone, r_s stands for radius of penetration damage zone include the wellbore, r_w stands for wellbore radius.

For the case three of history matching bottom hole pressure, the permeability change is irreversible along with the pressure change. Fig. 66 presents the permeability multiplier hysteresis along with the pressure change. The permeability multiplier, which is between zero to one, is defined as the ratio of current permeability to initial reservoir permeability. The black curve stands for the main path of the permeability change when pressure is decreased during reservoir depletion. The rest colorful curves represent different rebound paths when the pressure is increased from a low pressure level later on. Additionally, a linear interpolation method is used to calculate the permeability multiplier among these curves.

What Fig. 66 shows is a general permeability hysteresis case, which is different with the irreversible permeability case we used in the above section. For the irreversible case, the permeability stays constant when the pressure is rebounded later on. However, for the permeability hysteresis case, the permeability will be still gradually increased when the pressure is rebounded, but it just follows different rising paths for the permeability change. Overall, the irreversible permeability case is the extreme example of permeability hysteresis case, which presents the largest permeability difference when reservoir pressure is decreased and then increased. Fig. 67 presents the results of history matching bottom hole pressure for the case three with the permeability hysteresis. The BHP data after well shut-in is well matched, and the adjusted reservoir permeability making the match happening is 430 md. The skin factor caused by the presence zone of altered permeability is -4.1 based on Eq. (58).

By comparing the case one with constant permeability and the case two with reversible permeability change, a larger permeability was derived from history matching bottom hole pressure when the stress-dependent permeability is considered. In other words, based on certain given BHP data, if we don't consider the permeability change (constant permeability), the permeability derived from history matching BHP will be smaller, which in return explains why we could observe a larger permeability decline from the initial permeability. On the other hand, the permeability change along with the pressure change has already been proved based on our field data and laboratory measurements in the above sections. Therefore, the stress-dependent permeability must be considered for

the reservoir modeling of Gulf of Mexico Deepwater, especially when we try to derive reservoir permeability from history matching bottom hole pressure.

By comparing the case two with reversible permeability change and the case three with permeability hysteresis, a larger permeability was derived from the case three, even though only 10 md larger. The main reason for the small difference (10 md) is that there was not enough pressure drop during the reservoir depletion, which in return did not bring much permeability decline. Based on Fig. 67, only around 270 psi pressure drop is observed for bottom hole pressure from the beginning to the moment of well shut-in. Comparing with decline of the bottom hole pressure, the pressure drop for near wellbore reservoir zone would be smaller. Therefore, not large enough permeability decline would be produced from the small pressure drop, and the difference between the case two with reversible permeability and case three with permeability hysteresis is much smaller.

If a large reservoir pressure drop happens near wellbore zone, such as from high production rate or long production time, we could see obvious difference about the derived permeability between the two cases: reversible permeability change and permeability hysteresis. To sum up, correctly applying stress-dependent permeability correlation is critical for deriving reservoir permeability based on history matching bottom hole pressure. A small permeability will be obtained if reservoir permeability is simply assumed constant, which in return will be interpreted as a large permeability decline. The permeability hysteresis should be taken into account, and the correlations could be measured from laboratory measurements.

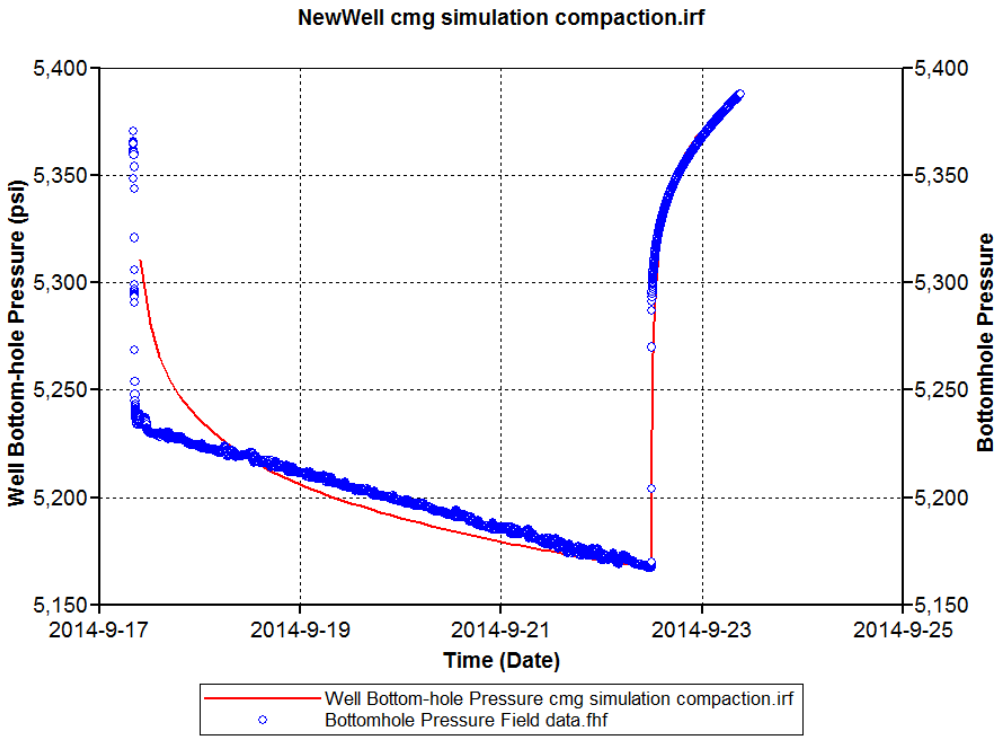

Figure 65: History matching bottom hole pressure for the case of compaction table with reversible change.

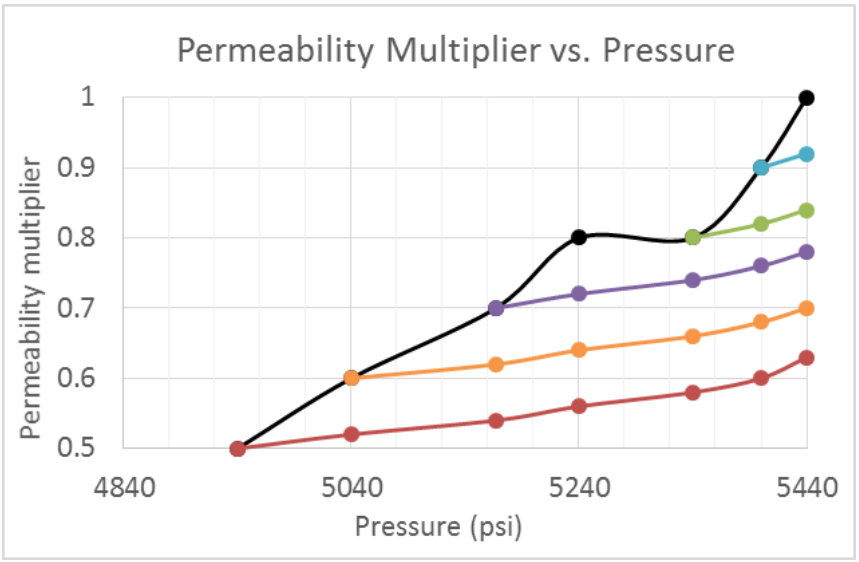

Figure 66: Permeability multiplier hysteresis along with the pressure change.

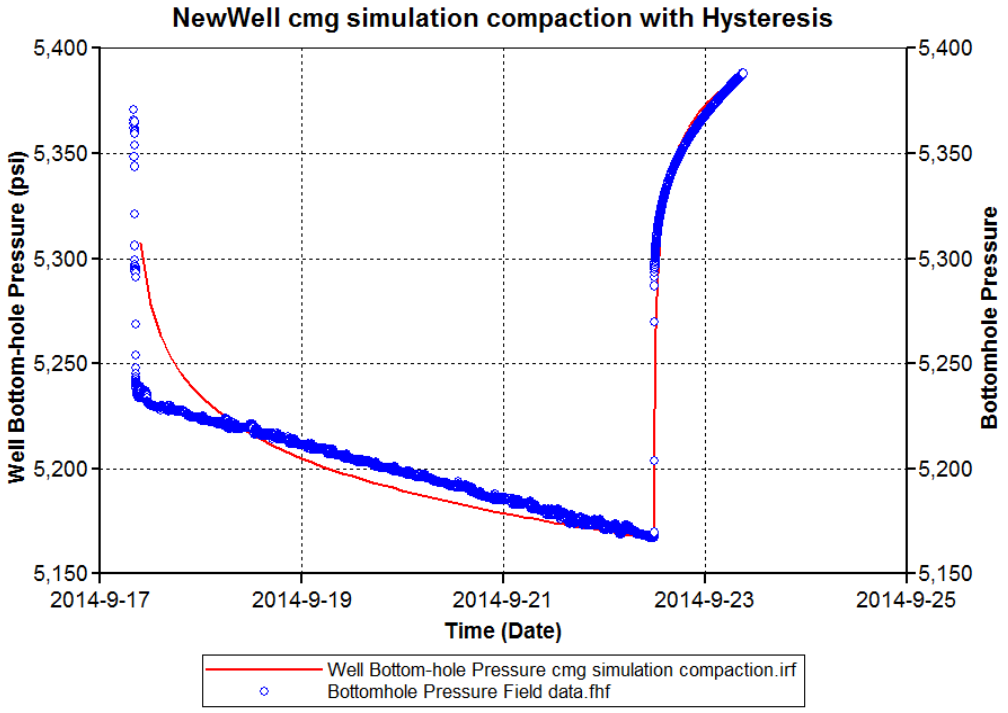

Figure 67: History matching bottom hole pressure for the case of permeability hysteresis.

5.5.3 Brugge Offshore Field Simulation

The Brugge offshore field is a synthetic reservoir built by TNO, which is often used as a unique SPE benchmark reservoir model for scientific research from water-flooding test to history matching validation. According to Peters et al. (2009), the Brugge field contains an East-West elongated half-dome with a large boundary fault at its northern edge, and an internal fault with a modest throw to the northern edge. The Brugge reservoir is designed as a typical North Sea Brent-type field in terms of the formation properties and thicknesses. The critical reservoir properties, such as porosity, permeability, water saturation, PVT, and sedimentary facies have been provided for reservoir simulation.

Fig. 68 shows a schematics of 3D reservoir model for Brugge offshore field, where 20 vertical production wells have been drilled and completed. The mesh dimensions of this 3D reservoir modeling are $70 \times 24 \times 9$. The Brugge field will be producing without pressure support from active aquifer. The initial reservoir pressure is 8000 psi, and the reservoir wells are scheduled to be produced for 20 years, where black oil isotropic model is applied. The default operating constraints for this reservoir modeling are 4000 psi of minimum bottom hole pressure and 10,000 STB/day of maximum production rate. In this section, we mainly focus on the effects of reservoir compaction and stress-dependent permeability on cumulative oil production based on the Brugge offshore field. Additionally, sensitivity analysis will be also conducted in terms of bottom hole pressure, production rate, shut-in periods, and water injection.

Fig. 69 shows effects of reservoir compaction on cumulative oil production for two different cases based on Brugge offshore field, where x axis is time and y axis is cumulative oil production. One case (red curve) is for constant permeability, and the other case (blue curve) is for permeability change with compaction table. Apparently, when the stress-dependent permeability (compaction table) is considered, the predicted cumulative oil production is much smaller than the case with constant permeability. The difference of cumulative oil production between the two cases is $5.8 \times 10^7\ STB$ for 10 years and $6.31 \times 10^7\ STB$ for 20 years, which means the production difference is increased along with the producing time. If we don't consider the stress-dependent permeability for reservoir simulation, the predicted cumulative oil production will be significantly over estimated, which will largely mislead reservoir management and field development.

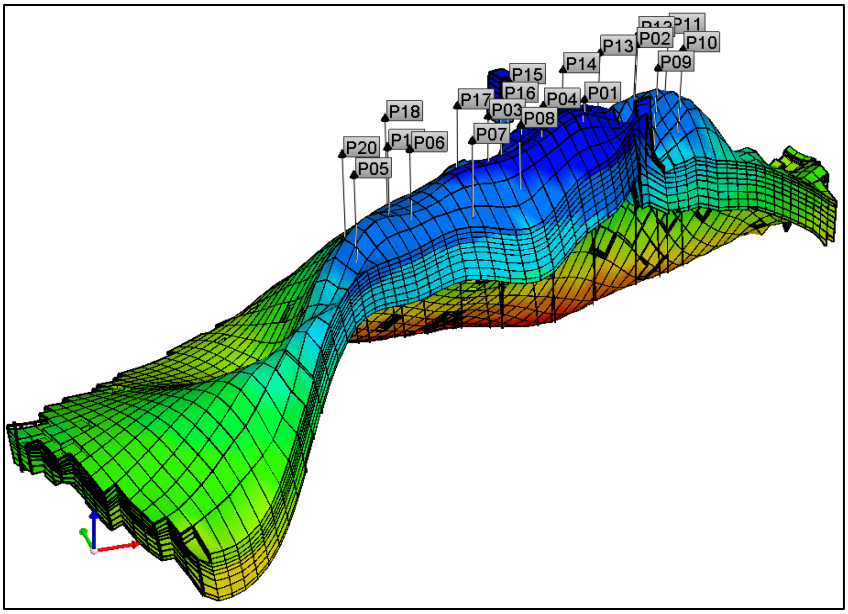

Figure 68: Schematic of 3D reservoir model for Brugge offshore field.

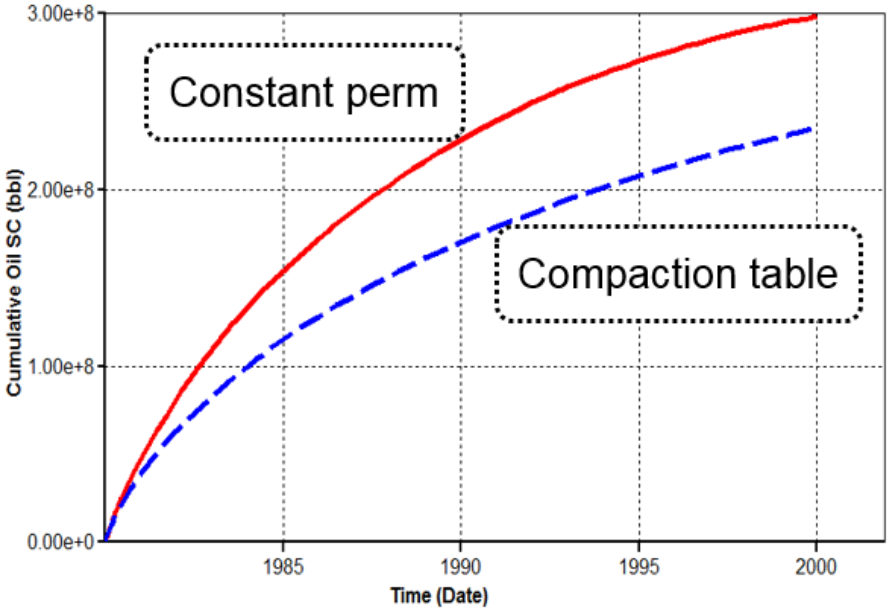

Figure 69: Effect of compaction on cumulative oil production.

In order to investigate the impacts of different parameters on cumulative oil production and learn how to optimize operation constraints for maximizing production, sensitivity analysis are performed as follows. Fig. 70 shows effect of bottom hole pressure on cumulative oil production. Four different numerical cases are conducted: the cases with constant permeability for bottom hole pressure of 2000 psi and 4000 psi, and the cases with compaction table for bottom hole pressure of 2000 psi and 4000 psi.

Several points are observed when we compare the numerical results among the four different cases. Firstly, the results on Fig. 70 confirm the cumulative production is largely increased at a lower bottom hole pressure, no matter if the stress-dependent permeability is considered or not. Secondly, by comparing the two cases with constant permeability, the cumulative production is increased about $6.43 \times 10^7\ STB$ when bottom hole pressure is decreased from 4000 psi to 2000 psi. By comparing the two cases with compaction table, the cumulative production is increased about $3.10 \times 10^7\ STB$ when bottom hole pressure is decreased from 4000 psi to 2000 psi. Therefore, the increase of cumulative production because of the smaller bottom hole pressure becomes significantly less when the stress-dependent permeability is considered. In other words, to reduce bottom hole pressure might not boost as much cumulative production as we expected when the stress-dependent permeability is taken into account.

Thirdly, by comparing the two cases with bottom hole pressure of 4000 psi, the cumulative production is reduced about 6.31×10^7 STB if we consider the compaction table for reservoir simulation. By comparing the two cases with bottom hole pressure of 2000 psi, the cumulative production is reduced about $9.64 \times 10^7\ STB$ if we consider the

compaction table for reservoir simulation. Therefore, the cumulative production drop caused by the stress-dependent permeability becomes much larger at lower bottom hole pressure. This is mainly because that a larger permeability decline was caused by a larger pressure drop.

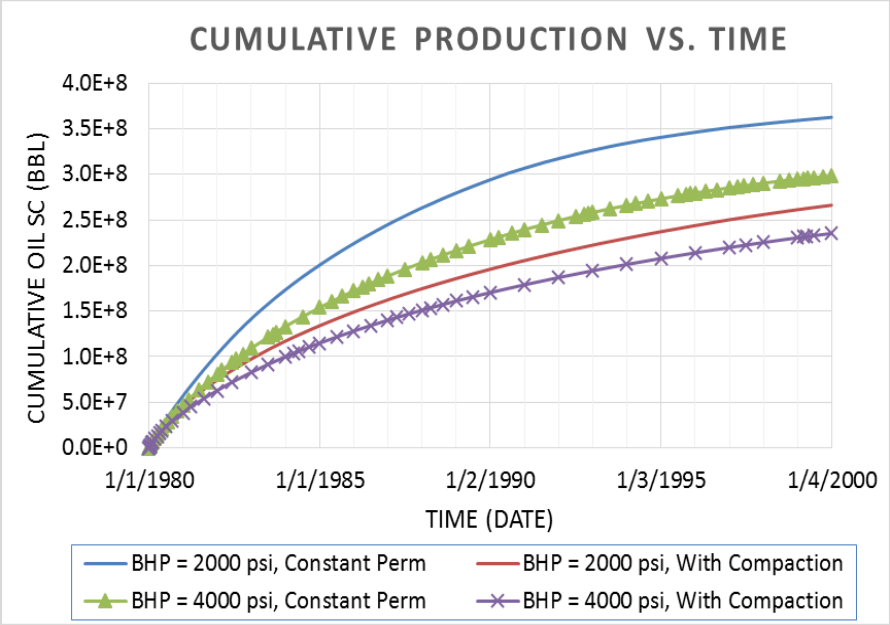

Figure 70: Effect of bottom hole pressure on cumulative oil production.

Fig. 71 presents the results of cumulative oil production along with time for five cases with different maximum production rate, where the stress-dependent permeability has been considered. The operating constraints are minimum bottom hole pressure of 4000 psi and varied maximum production rate. Five different maximum production rates are performed: 2000, 4000, 6000, 8000, and 10,000 STB. As on Fig. 71, when maximum production rate is larger than 4000 STB, such as 6000 and 8000 STB, there is no obvious difference for the cumulative oil production. The critical production rate could be roughly

estimated around 4000 STB based on that numerical results. Therefore, there is no obvious need to produce hydrocarbon at very high production rate from this offshore reservoir field since it does not contribute much for the increase of cumulative oil production, which, on the other hand, might quickly consume excessive reservoir energy.

However, if the stress-dependent permeability is considered, the results will be different in terms of critical production rate. Fig. 72 shows the results of cumulative oil production for five cases with different maximum production rates, where constant permeability is assumed. The results show obvious difference of cumulative production is observed among the cases of 2000, 4000, and 6000 STB. The critical production rate is roughly estimated around 6000 STB. When the maximum production rate is larger than 6000 STB, on obvious difference is observed for the cumulative production. By comparing the results from Fig. 71 and Fig. 72, the critical production rate is lower when the stress-dependent permeability was considered for reservoir simulation, which in return could provide some guides about optimizing production rate for better production performance.

Fig. 73 shows the results of cumulative oil production along with time for three cases with different compaction tables, where no well shut-in has been scheduled. The three different cases are reversible compaction table, compaction table with hysteresis, and irreversible compaction table (largest hysteresis). The results demonstrate the cumulative oil production is the same among the three cases if there are no well shut-in periods. The key difference between the three cases is the stress-permeability path when pressure is increased. However, if there is no pressure rebound caused by well shut-in or other operations, the permeability will just keep decreased along with the reservoir

pressure drop following the main stress-permeability path, which is exactly the same for all the three cases. Therefore, no difference of cumulative oil production is observed on the results of Fig. 73. However, on the other hand, the analyzed results above will be different if well shut-in are scheduled during the reservoir production.

Fig. 74 presents the results of cumulative oil production for three cases with different compaction tables, where well shut-in is scheduled to happen three times during the first six years. For example, wellbore maintenance could be one reason for well shut-in. When well shut-in is occurring, production rate will become zero, and the cumulative production curve will become flat, as shown on Fig. 74. The results show the cumulative oil production is lowest for the case of irreversible compaction table, which is about 4% less than the case of reversible compaction table in terms of final cumulative oil production. There is no obvious difference between the case of reversible compaction table and compaction table with hysteresis. Of course, the difference among the three cases highly depends on the amount of reservoir pressure drop, how strong the permeability hysteresis is, and the length of well shut-in. Overall, when adding well shut-in schedule, the cumulative oil production could be different for various compaction tables. Therefore, appropriate compaction table (stress-dependent permeability correlation) should be used for reservoir simulation and production prediction.

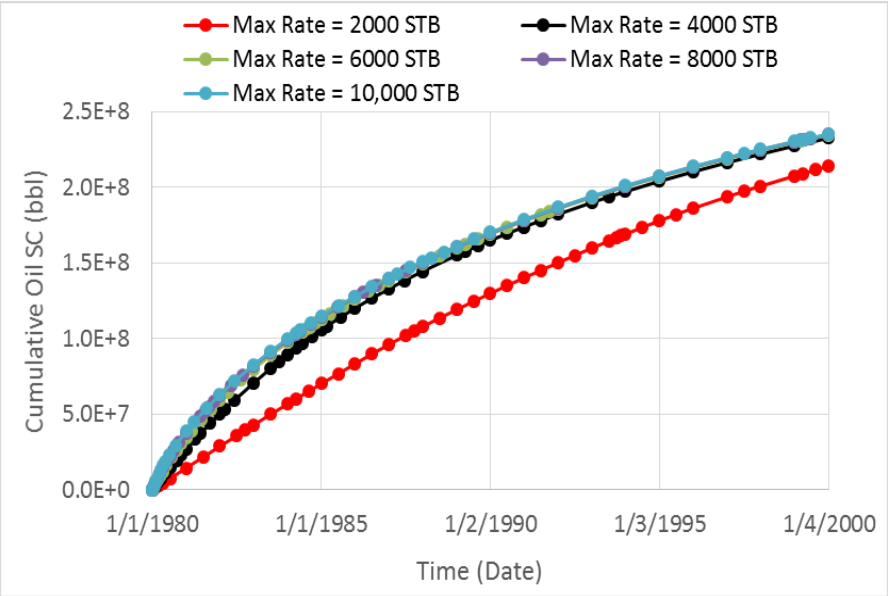

Figure 71: Effect of production rate on cumulative oil production for the case with permeability change.

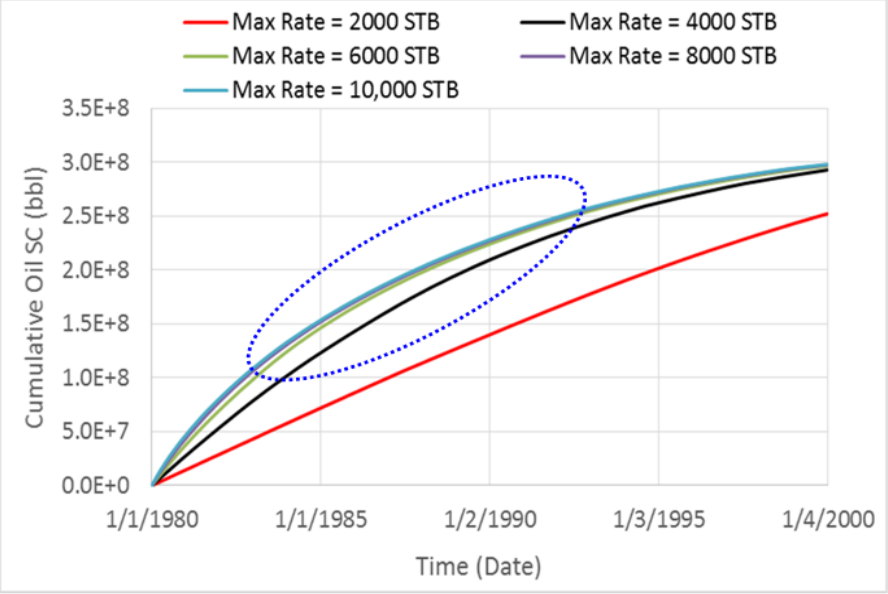

Figure 72: Effect of production rate on cumulative oil production for the case with constant permeability.

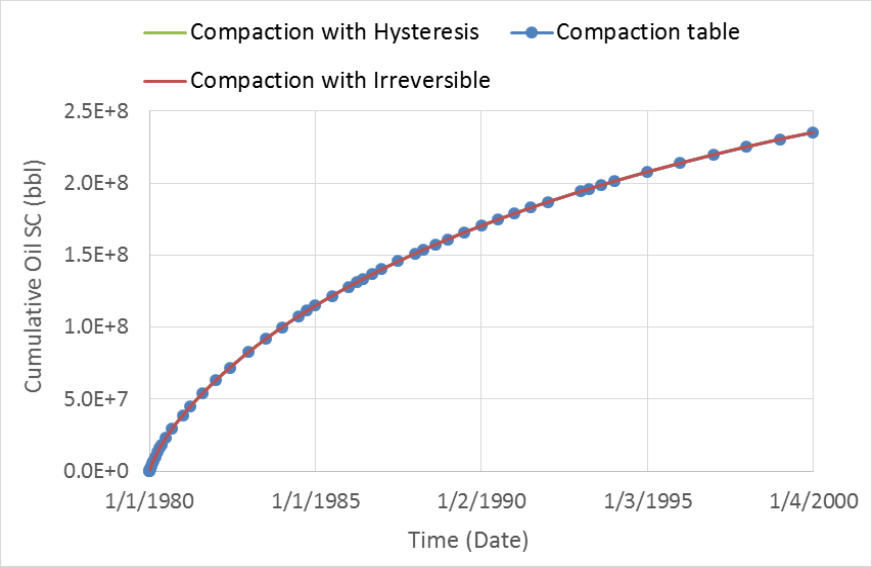

Figure 73: Effect of compaction on cumulative production without well shut-in.

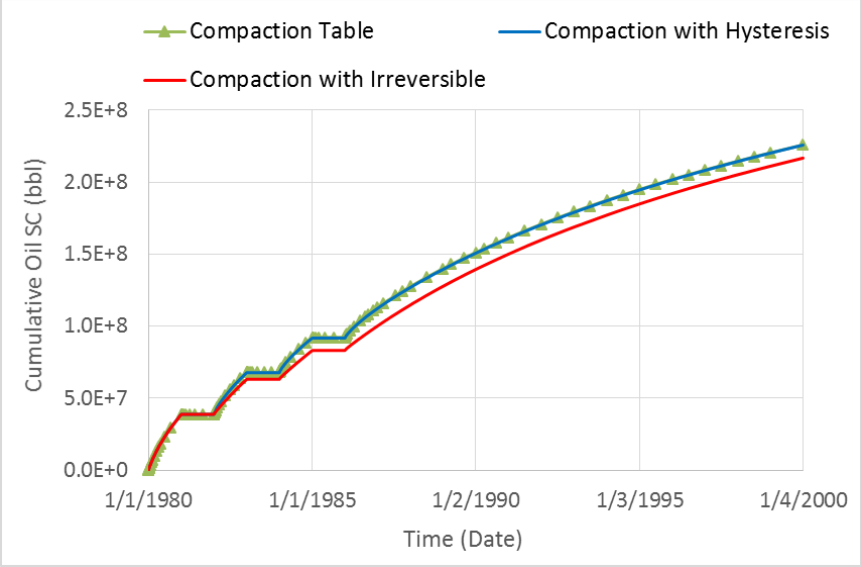

Figure 74: Effect of compaction on cumulative production with well shut-in.

Fig. 75 presents the effect of varied Bottom Hole Pressure (BHP) on cumulative oil production for three different cases: constant permeability, reversible compaction table, and irreversible compaction table. The motivation of varying bottom hole pressure is from the observation of daily production rate profile of on Fig. 62, where production rate fluctuated about 15%. The production rate fluctuation could be from the variation of bottom hole pressure. Therefore, we want to investigate the effects of varied BHP on cumulative production when different compaction tables are considered. In the three numerical cases above, bottom hole pressure was arranged to repeatedly go up and down 800 psi (20%) every month based on the initial BHP of 4000 psi.

As the results shown on Fig. 75, the cumulative oil production is different among the three cases. In terms of final cumulative oil production after 20 years, the case of constant permeability is 20% higher than the case of reversible compaction table, and the reversible compaction case is 4% higher than the irreversible compaction case. Therefore, the variation of bottom hole pressure could provide different result of cumulative oil production for various compaction tables. If the compaction table with permeability hysteresis is required to be considered for reservoir compaction behaviors, optimizing the schedule of different bottom hole pressures might improve overall production performance.

Fig. 76 shows the effect of water injection on cumulative oil production. Two cases are conducted: case one includes water injection, and case two does not. The stress-dependent permeability has been taken into account for both numerical cases above. The results present the cumulative oil production can be increased by water injection. This is

because water injection can maintain reservoir pressure and simultaneously minimize permeability decline. For the case two without water injection, reservoir permeability gradually decreases along with the drop of reservoir pressure. For the case one with water injection, the decline of reservoir permeability is weakened by the support of water injection.

The difference of cumulative production between the two cases becomes relative narrower at the late production stage on Fig. 76. The main reason is explained as following. For the case one with water injection, much more hydrocarbon has been produced because of relative high reservoir permeability. However, after around seven years' production, the production rate of case one gradually becomes smaller than the production rate of case two. This is because certain water injection is not enough to support excessive reservoir depletion caused by large hydrocarbon production. Overall, water injection can significantly improve the cumulative production for reservoir considering the stress-dependent permeability, at least for certain years. On the other hand, water injection might not be cost-efficient in terms of high expense for GOM Deepwater fields, except that there are existing available wells for water injection.

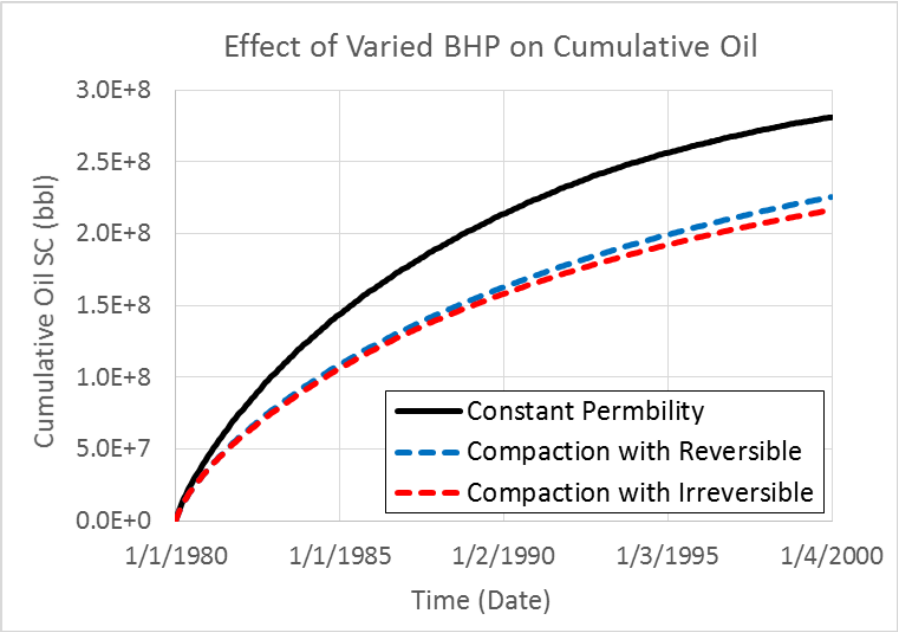

Figure 75: Effect of varied BHP on cumulative oil production for three different cases.

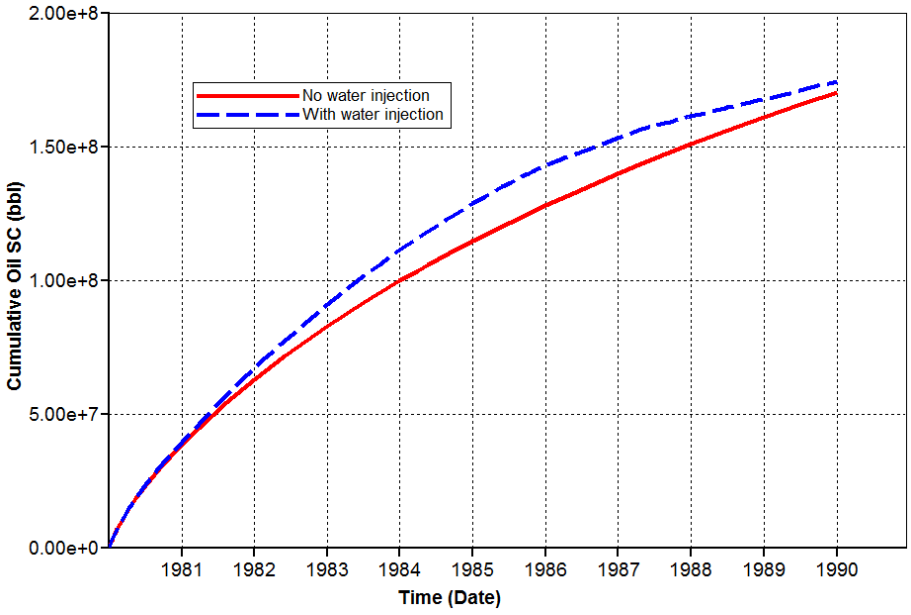

Figure 76: Effect of water injection on cumulative oil production.

5.6 Conclusions and Discussions

Based on the provided laboratory and field data of Gulf of Mexico Deepwater turbidite reservoirs, the dynamic compaction effects on the permeability loss and cumulative production have been investigated. The permeability hysteresis caused by natural irreversible compaction processes are proposed to explain the difference between the laboratory-measured and field-evaluated permeability decline trends. The well buildup pressure tests and history matching bottom hole pressure modeling are conducted to show the derived permeability differences among the numerical cases with different compaction tables. Additionally, the coupled flow and geomechanics models with proposed compaction mechanism have been built to predict the compaction impacts on the permeability decline and production performance for several different operating scenarios. Overall, several conclusions shown as follows are drawn from the results of this study:

1) The compaction processes can be generally divided into two phases for unconsolidated GOM sands: consolidation and deformation.
2) Irreversible compaction processes are obviously observed in thin section micrographs, which results in the hysteresis of rock compressibility and permeability.
3) The permeability decline is mainly caused by pore pressure drop and irreversible compaction.
4) The stress-dependent permeability largely reduces the cumulative hydrocarbon production.

5) Based on the pressure buildup tests, the reservoir permeability derived from Horner Plot method is smaller when the stress-dependent permeability is considered.
6) With considering compaction table, the permeability derived from history matching bottom hole pressure is larger, and the predicted critical production rate is smaller.
7) The modeling with different compaction tables show obvious differences on the cumulative production when either well shut-in periods or varied bottom hole pressure are considered.
8) Water injection could improve cumulative production by maintaining reservoir pressure and minimizing permeability loss, while it might be not cost-efficient.

Additional research is still required to further understand the mechanisms governing hydrocarbon flow and permeability change within the unconsolidated formations in order to mitigate compaction effects and maximize well production. Since natural irreversible compaction processes are widely observed in unconsolidated GOM Deepwater reservoirs, compaction effects and permeability hysteresis should be taken into account as an important part of integrated plan for reservoir management and field development. A compromise solution between maximizing hydrocarbon recovery benefitting from compaction drive and mitigating the compaction effects on reservoir integrity need to be made by controlling the production rate and flowing Bottom Hole Pressure (BHP). Continued filed monitoring is a critical part of reservoir development,

where the recorded data (BHP and production data) can be used to validate geomechanical reservoir modes and improve the accuracy of predictions.

To be specific, the recommendation of future work about this project can be briefly described as: a) analyze more pressure buildup data and conduct more history matching on BHP for cross-validating the proposed mechanism; b) develop a solid coupled flow and geomechanics reservoir model for the applied Deepwater well by history matching both production rates and multiple buildup BHP; c) improve techniques for deriving stress-permeability compaction tables without relying on significant production data, such as based on laboratory-measured data; d) apply the developed techniques and learned lessons to minimize compaction issues and optimize production performance for different operating scenarios in GOM Deepwater reservoirs.

CHAPTER VI

STRESS CREEP AND EFFECTIVE STRESS COEFFICIENT*

6.1 Introduction

The production and reserves decline from conventional resources has caused unconventional resources more and more important. Unconventional reservoirs, such as shale, coalbed methane, and heavy oil, typically have low porosity and extra-low permeability, so enhanced recovery techniques must be required. With the advanced technologies of multistage fracturing and horizontal drilling, significant amounts of hydrocarbons have been economically produced from shale reservoirs to satisfy the increasing global energy demand. By applying scanning electron microscope (SEM) images, different pore-media have been extensively observed in shale core samples: organic matter also known as kerogen, inorganic matter (such as clay, quartz, and carbonate), and the fractures. Due to different rock properties and flow mechanisms on each pore medium, the presence of multiple pore-media and fracture networks has made reservoir characterization and prediction of production performance more complex and challenging (An 2014; Zhang et al. 2017; Zhu et al. 2018; Zhang et al. 2018). Rock permeability is an essential factor for production prediction and economic evaluation, which is often measured based on core samples in laboratory. However, several

* Part of data reported in this chapter is reprinted with permission from "Impacts of Kerogen and Clay on Stress-Dependent Permeability Measurements of Shale Reservoirs" by An, C., Guo, X., Killough, J., 2018. Paper presented at the Unconventional Resources Technology Conference, 23-25 July, Houston, Texas, USA. Copyright 2018 by URTeC, whose permission is required for further use.

phenomena such as stress creep and effective stress coefficient still present difficulties in correctly measuring and interpreting permeability under varying compaction stresses for core measurements.

Based on the thorough literature review, not much research has been conducted to investigate the impacts of kerogen and clay on stress-dependent permeability measurements for shale rocks because of the presence of the creep phenomenon and path-dependent stress. The improved knowledge is inquired to enable the development of best practices for tight rock permeability measurements and provide more accurate results of permeability for reservoir management. Therefore, in the study of this chapter, the mechanisms of stress creep and effective stress coefficient are fully investigated. Their impact on permeability measurements are analyzed by various experiment data. Both physics, stress creep and effective stress coefficient, are highly related to the content of kerogen and clay in rock samples, so the targeted formation is mainly organic-rich or clay-rich shale reservoirs. The structure of this chapter is described as follows. Firstly, the creep strain model is introduced to calculate the creep strain and stress change over time based on the time-dependent behavior of compaction creep. Secondly, an improved stress-dependent permeability model is proposed to predict the permeability decline under constant stress along with time caused by the stress creep phenomenon. Thirdly, effective stress coefficient is thoroughly studied, where its effect on permeability change and cumulative production is investigated by the coupled flow-geomechanics model.

6.2 Creep Strain Model

6.2.1 Creep Behavior

The time-dependent behavior of soils and porous rocks has been widely investigated though uniaxial and triaxial tests (Augustesen et al. 2004, Danesh et al. 2017). The creep process performed under constant stress is shown in a strain-time diagram on Fig. 77, where the process is usually divided into three stages: primary creep (transient creep), secondary creep (steady-state creep), and tertiary creep (accelerating creep). At the initial time t_0, an initial strain ε_0 is brought by initial stress. When the exerted stress is kept constant, the strain still increases along with time. On the other hand, to correctly measure rock permeability and porosity is quite important for characterizing reservoir and predicting production performance during depletion, which is accomplished by experimental measurements in laboratory. However, most permeability experiments were performed in a relative short time, where the impacts of compaction creep on rock properties have not been taken into account. Based on the time-dependent strain, the compaction creep refers to a decline of measured permeability over time while a constant confining stress is applied.

Fig. 78 presents schematics of relationships among permeability, net stress (effective stress), and time during creep process. The left image describes permeability decreases along with the increasing of net stress, which has been observed on many experimental data (David et al. 1994, Mokhtari et al. 2013, Chhatre et al. 2014). When the net stress is kept constant from point A to B, the permeability still decreases because of compaction creep impacts. As Fig. 4 shows, the measured oil permeability decreases along

with time under constant net confining stress because of the stress creep phenomenon. Therefore, the objective of this study is to investigate the effects of compaction creep on permeability measurements and how to correctly quantitatively account for it. Before we move on, let us again elaborate on the concept of effective stress because it is extensively used in this chapter. Terzaghi (1923) was the first to introduce the equations of effective stress for soil analyses. Then Biot (1941) derived the elasticity equations governing poroelastic behaviors for calculating deformation. In the section four of chapter five, the equations of effective stress law are expressed as on Eq. (54) and (55). The effective stress is equal to total applied stress mines the product of pore pressure and Biot's coefficient, where Biot's coefficient α is typically very close to one.

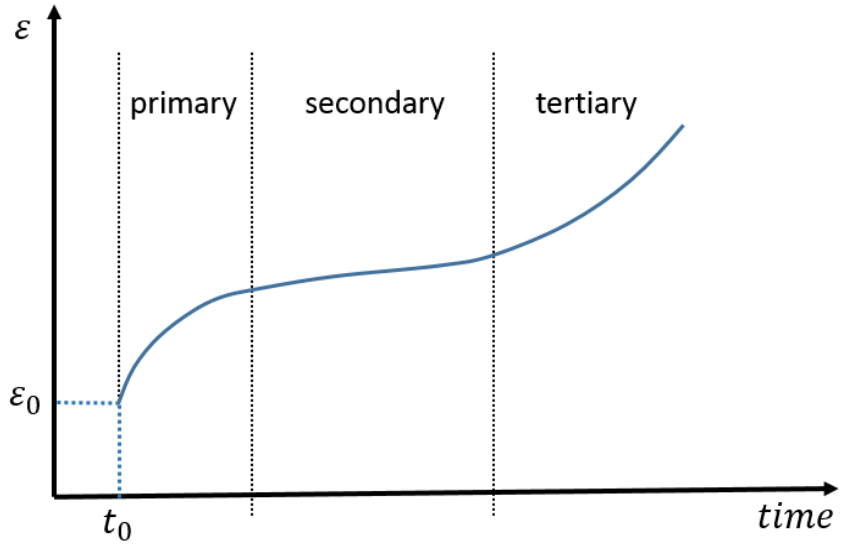

Figure 77: Three stages of creep behavior under constant stress.

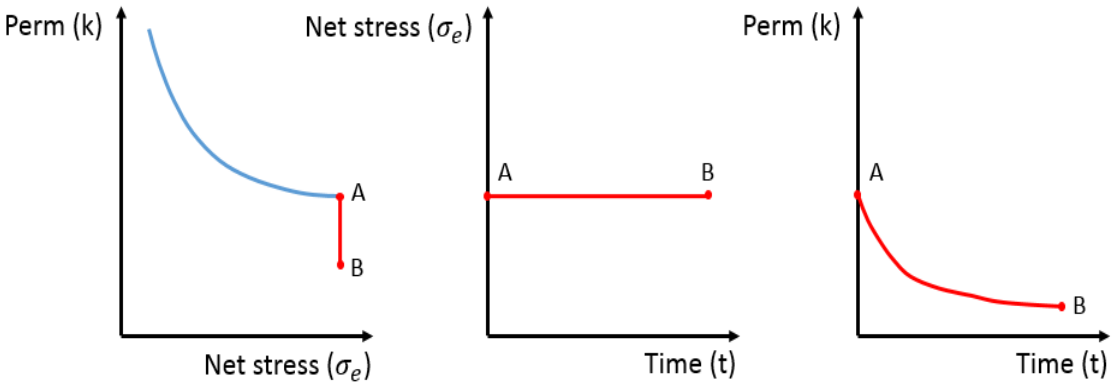

Figure 78: Schematics of relationships among permeability, net stress, and time during creep.

The creep process can be significantly complex because it could include elastic creep, viscoelastic creep, plastic creep, and brittle creep (Boukharov and Chanda, 1995). However, we only focus on the impacts of compaction creep on permeability measurements in this study. The tertiary stage of creep is often ignored because it is related to rock failure and we don't fracture core samples during core-flooding experiments. Usually, the proposed creep model become so complicated that there is no real practical way to apply it for engineering problems. Therefore, only the primary stage of compaction creep (transient creep) is considered in this study, and a simplified formulation is provided to calculate the creep strain along with time.

There are two major reasons for this proposal. Firstly, based on the experimental results of the strain behavior of porous media, some exponential functions have been observed to well match the creep strain data along with time (Sone and Zoback 2010, Brantut et al. 2013, Li et al. 2013, Liu et al. 2015, Yu et al. 2016). The primary stage of creep strain is mainly an exponential function. Secondly, the secondary stage of creep

(steady-state creep) strain is mainly a linear function of time and the slope is usually small. In other words, not much increase of strain will be observed during a certain long time in the secondary stage. Additionally, the creep strain of the primary stage is often much larger than that of the secondary stage.

The creep strain formulation derived from the primary stage are shown on Eq. (59) and (60) (Nishihara 1952, Skrzypek and Ganczarski 2015). The first term on the right hand σ/E_e denotes the instantaneous strain under stress at $t = 0^+$, and the second term stands for the viscoelastic strain changes along with time. This creep strain model is derived by combining the Maxwell model and the Kelvin-Voigt model, where the differential stress-balance equation is displayed in Eq. (60). By integrated Eq. (60) with initial condition, the strain Eq. (59) is obtained. Fig. 79 displays the schematic of the proposed creep model under compaction, where the total strain is made up of two parts. The instantaneous strain is mainly caused by the brittle part of rock based on Hookean substance law. The viscoelastic strain is primarily caused by both brittle and soft parts together in rock, which is based on Newtonian substance law.

The viscoelastic compaction strain occurs when the applied stress is less than the yield stress of rock, which is the most typical stress condition during permeability measurements. Even though permeability hysteresis and plastic strain were observed in some experimental data, we don't consider visco-plastic strain in this study as we explained above. The strain change related to thermal expansion is not taken into account as well.

$$\varepsilon(t) = \frac{\sigma}{E_e} + \frac{\sigma}{E_{ve}}\left[1 - \exp\left(-\frac{E_{ve}}{\eta_e}t\right)\right] \tag{59}$$

$$\frac{E_e E_{ve}}{E_e + E_{ve}} \varepsilon + \frac{\eta_e E_e}{E_e + E_{ve}} \frac{d\varepsilon(t)}{dt} = \sigma \tag{60}$$

where ε denotes strain, t represents time, σ is the applied stress on the rock surface, E_e and E_{ve} stand for elastic and viscoelastic moduli, η_e represents viscosity coefficient of material.

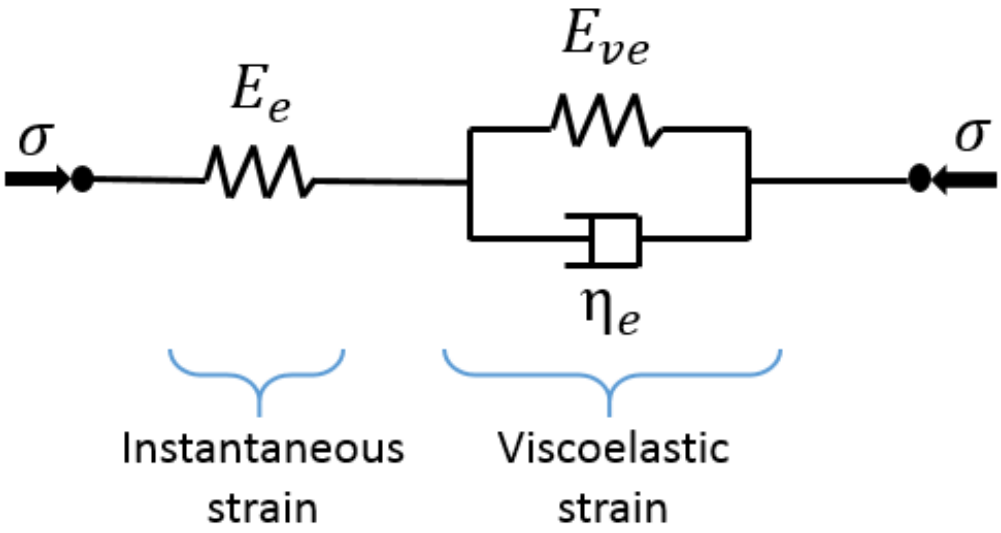

Figure 79: Schematic of compaction creep model.

6.2.2 Permeability Measurement Test

Permeability measurement is a critical part to predict the potential of hydrocarbon flow in core samples and productivity of the targeted formation. Due to low porosity, extra-low permeability, and complex lithology, to measure permeability for tight shale reservoirs is different from the procedures for conventional rocks. Steady state flow rate is the most typical method for the measurement of permeability, where a constant pressure drop is provided to allow gas or liquid flow from one side to other side of core, and then the permeability is calculated by Darcy's law. However, this method faces a few

challenges to low permeability rock, such as significantly longer equilibration time. In tight rocks, permeability has been also measured by unsteady state approaches based on core plug or crushed rock.

Two common unsteady-state approaches are pulse decay method and crushed rock method. For the pulse decay method (Dicker and Smits, 1988), a pressure pulse is provided at the upstream of core plug to allow pressure decay over time, where the transient pressure decay is used to derive permeability. For the crushed rock method (Luffel et al. 1993, Profice et al. 2012), a quantity of small rock particles is used to estimate permeability using a pulse decay experiment. Even though the crushed rock method is faster and less expensive than traditional plug tests, it is restricted to measurement in the absence of overburden stress effects, which does not represent in-situ reservoir condition. For both the steady-flow method and the pulse decay method, core plug is used to measure permeability under certain confining pressure, which means the stress impacts have been taken into account.

Fig. 80(a) presents a typical schematic of permeability measurement apparatus on core plug. Core plug is placed in a core holder, where a sleeve fluid system is used to provide a constant confining pressure. To realistic mimic reservoir conditions, fluid pressure inside pore media should be maintained by pump as well for permeability measurement. However, in many experiments, pore pressure is simply ignored for simplicity, and only the confining pressure is changed to adjust effective stress based on the effective stress law equation. Fig. 80(b) shows the stress state around core plug based on Fig. 80(a). In addition to pore pressure p_{pore} and confining pressure σ_c, the equal

uniaxial stresses are applied on the two sides of the core plug. It should be noted that P_{in} is certainly larger than P_{out} in order to provide driving force. However, since the pressure difference between them is usually significantly smaller than the confining stress and a stress balance system is required to calculate creep strain, it is assumed that we use their average value for the axial stress.

Based on the triaxial compression test theory, the stress-strain equations are displayed in Eq. (61) to (64). If the creep strain is calculated based on Eq. (59), Eq. (65) to (66) could be derived, where the creep strain is a function of stress and time. Because of the creep strain mechanism, the stress change over time is displayed as in Eq. (69) and (70), where the axial and lateral strain changes can be calculated based on Eq. (67) and (68). In order to derive these equations below, three major assumptions are required as follows: rock properties are homogeneous; Young's modulus and Poisson's ratio do not change over time because of creep; the stress balance is maintained all the time.

$$\varepsilon_{ax} = \frac{1}{E}\left[(\sigma_{ax} - \alpha p_{pore}) - 2v(\sigma_c - \alpha p_{pore})\right] \tag{61}$$

$$\varepsilon_{lateral} = \frac{1}{E}\left[(1 - v)(\sigma_c - \alpha p_{pore}) - v(\sigma_{ax} - \alpha p_{pore})\right] \tag{62}$$

$$\sigma_{ax} = \frac{E(1-v)}{(1+v)(1-2v)}\left[\varepsilon_{ax} + \frac{2v}{1-v}\varepsilon_{lateral}\right] + \alpha p_{pore} \tag{63}$$

$$\sigma_c = \frac{E}{(1+v)(1-2v)}[v\varepsilon_{ax} + \varepsilon_{lateral}] + \alpha p_{pore} \tag{64}$$

$$\varepsilon_{ax} = \frac{1}{E_e}\left[\sigma_{ax} - 2v\sigma_c + \alpha p_{pore}(2v - 1)\right] + \frac{1}{E_{ev}}\left[\sigma_{ax} - 2v\sigma_c + \alpha p_{pore}(2v - 1)\right]\left[1 - exp\left(-\frac{E_{ve}}{\eta_e}t\right)\right] \tag{65}$$

$$\varepsilon_{lateral} = \frac{1}{E_e}\left[(1-v)\sigma_c - v\sigma_{ax} + \alpha p_{pore}(2v-1)\right] + \frac{1}{E_{ev}}\left[(1-v)\sigma_c - v\sigma_{ax} + \alpha p_{pore}(2v-1)\right]\left[1 - exp\left(-\frac{E_{ve}}{\eta_e}t\right)\right] \quad (66)$$

$$\Delta\varepsilon_{ax}(t) = \frac{1}{E_{ev}}\left[\sigma_{ax} - 2v\sigma_c + \alpha p_{pore}(2v-1)\right]\left[1 - exp\left(-\frac{E_{ve}}{\eta_e}t\right)\right] \quad (67)$$

$$\Delta\varepsilon_{lateral}(t) = \frac{1}{E_{ev}}\left[(1-v)\sigma_c - v\sigma_{ax} + \alpha p_{pore}(2v-1)\right]\left[1 - exp\left(-\frac{E_{ve}}{\eta_e}t\right)\right] \quad (68)$$

$$\Delta\sigma_{ax}(t) = \frac{E_e(1-v)}{(1+v)(1-2v)}\left[\Delta\varepsilon_{ax}(t) + \frac{2v}{1-v}\Delta\varepsilon_{lateral}(t)\right] \quad (69)$$

$$\Delta\sigma_c(t) = \frac{E_e}{(1+v)(1-2v)}\left[v\Delta\varepsilon_{ax}(t) + \Delta\varepsilon_{lateral}(t)\right] \quad (70)$$

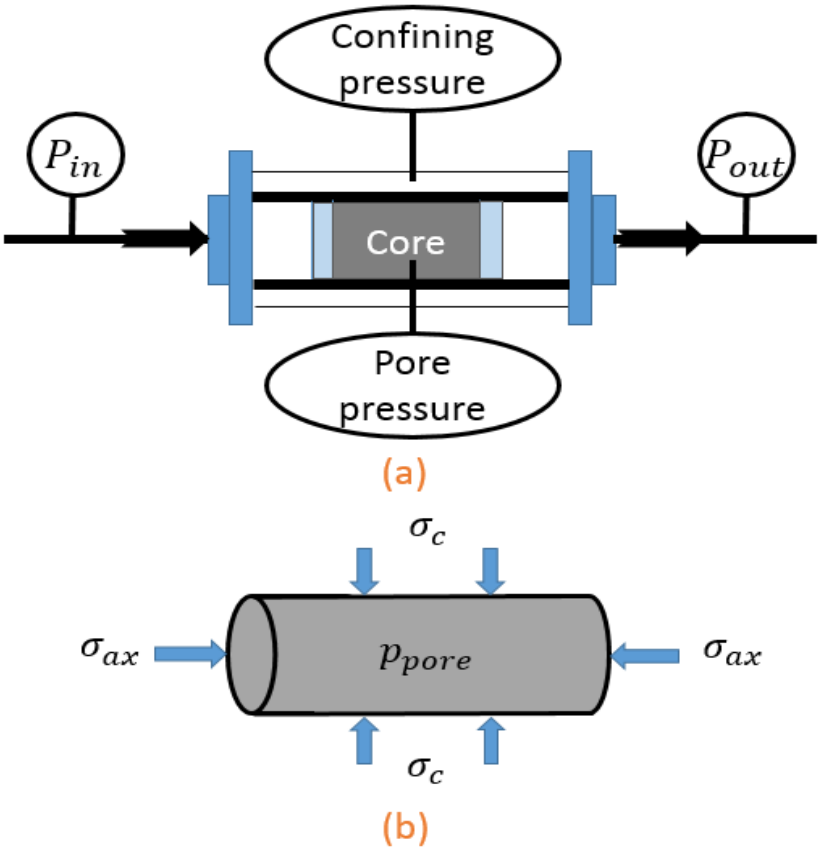

Figure 80: Schematics of (a) permeability measurement on core plug; (b) stress state on core plug.

6.3 Improved Stress-dependent Permeability Model

Effective stress has an obvious effect on rock permeability, especially on low-permeability sedimentary rocks. During reservoir depletion caused by hydrocarbon production, reservoir permeability is reduced along with the decrease of pore pressure and the increase of effective stress exerted on rock. Based on the experimental measured data, many empirical relationships have been proposed to describe the permeability change along with stress change (David et al. 1994, Evans et al. 1997, Ghabezloo et al. 2009). The fitting relationships can be generally divided into exponential law and power law relationships.

David et al. (1994) performed stress-dependent permeability experiments for five different sandstones by using water as test fluid. They suggested an exponential relationship would be suitable to describe the permeability reduction caused by compaction. Based on the results of measurements, Mokhtari et al. (2013) stated effective permeability declined exponentially with increasing effective stress for both fractured and unfractured shale core samples. Chhatre et al. (2014) used a steady-state method to measure liquid permeability of intact tight rock samples under net confining stress. The fitting curves based on their measurements display an exponential relationship between permeability and stress. Katsuki et al. (2016) stated the permeability of Eagle Ford core exponentially decreases with the increase of net stress based on their experimental permeability measurements.

Fig. 81 shows measured liquid permeability exponentially decreases with increasing drawdown pressure for three core samples, where the data were extracted from Chhatre (2014). The fitting dash curve is an exponential function. Therefore, the exponential relationship is chosen to describe the permeability change along with stress change in this study, which can be generally expressed as Eq. (71). Based on this equation, the permeability change because of the creep phenomenon can be calculated by deriving the effective stress change caused by the creep strain.

$$k = k_i \exp[-r(\sigma_e - \sigma_{ei})] \tag{71}$$

where k denotes the permeability under the effective stress σ_e, k_i represents the permeability under the effective stress σ_{ei}, r is the stress sensitivity coefficient of the material.

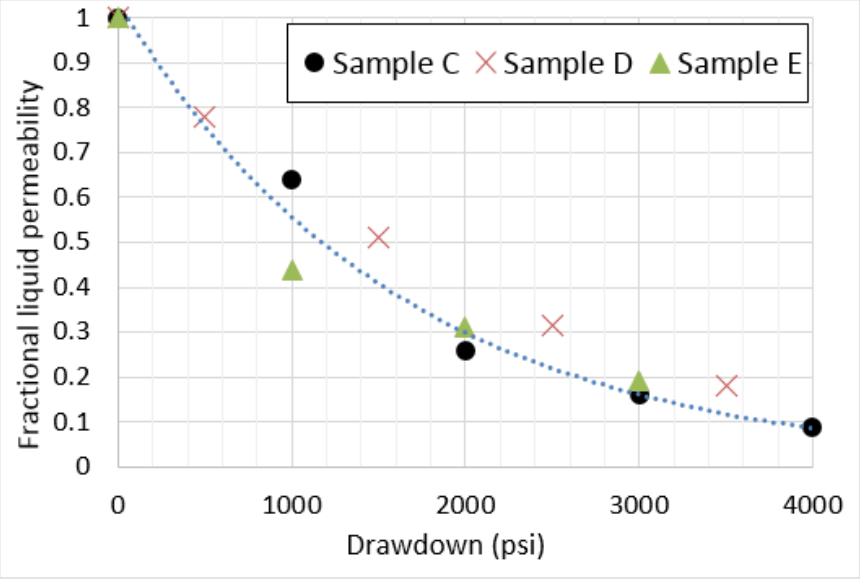

Figure 81: Measured liquid permeability decreases with increasing drawdown pressure for three core samples (modified from Chhatre et al. 2014).

As we mentioned earlier, it is often the confining pressure that is changed to alter the effective stress in most permeability measurements. Therefore, we assume the permeability change because of creep mechanism is mainly resulted by the confining stress change caused by the creep strain, where the pore pressure is constant. By inserting Eq. (70) into Eq. (71), the improved permeability model considering the creep effects is shown in Eq. (72). When the creep has not started at the initial time $t = 0^+$, Eq. (72) becomes exactly the same with Eq. (71). On the other hand, if the axial stress is near the confining stress, which might lead to close values between axial and lateral strain, the permeability including the creep effects could be calculated based on Eq. (73) and (74) (Yu et al. 2016). These equations describe a nonlinear relationship of permeability, porosity, and volumetric strain.

$$\frac{k}{k_i} = \exp[-r(\sigma_c - \sigma_{ci})] \times \exp\left[\frac{-rE_e}{(1+v)(1-2v)}\left(\frac{v}{E_{ev}}\left[\sigma_{ax} - 2v\sigma_c + \alpha p_{pore}(2v-1)\right]\left[1 - exp\left(-\frac{E_{ve}}{\eta_e}t\right)\right] + \frac{1}{E_{ev}}\left[(1-v)\sigma_c - v\sigma_{ax} + \alpha p_{pore}(2v-1)\right]\left[1 - exp\left(-\frac{E_{ve}}{\eta_e}t\right)\right]\right)\right] \tag{72}$$

$$\frac{k}{k_i} = \frac{1}{1+\varepsilon_v}\left(1 + \frac{\varepsilon_v}{\phi_i}\right)^3 \tag{73}$$

$$\varepsilon_v = \varepsilon_{ax} + 2\varepsilon_{lateral} \tag{74}$$

where ε_v stands for volumetric strain, ϕ_i represents initial rock porosity.

Yu et al. (2016) conducted laboratory creep tests for studying the creep behavior of shale core samples. The experimental data from a uniaxial compression creep test were extracted and plotted as blue dots on Fig. 82, where the measurement time was about 60 hours. Unfortunately, the rock sample minerology was not included for this experiment in the reference. Based on Eq. (61), the axial strain is calculated along with time, where the initial rock parameters of the creep model are shown in Table (12). On Table (12), the values of stresses and pore pressure are exactly the same with the experiment condition, and the rock modulus are obtained from matching these experimental data.

After we compared the model results with the uniaxial compression test, next step is to compare the results with the triaxial compression test. Sone and Zoback (2013) studied the axial and lateral creep strain responses of various shale rocks in a series of triaxial laboratory experiments. The blue dots on Fig. 83 are axial strain data during the triaxial stage from experiments using a Haynesville vertical sample, which was extracted from Sone and Zoback (2013). The brief summary of the Haynesville rock minerology is as following: the volume of clay is about 36% to 39%, the volume of kerogen is about 8%, the volume of carbonate is about 20% to 22%, and the estimated porosity is about 6%. The results of red curve are calculated based on the creep strain model. The measured experimental data are well matched with the exponential function of the creep strain model, which proves the accuracy and availability of the proposed model. In addition, their experimental data show the axial strain is much larger than the lateral strain. The creep strain behaviors highly depend on the rock composition and stress level as well.

Table 12: Initial rock parameters for creep strain model.

σ_{ax} (GPa)	0.025		σ_c (GPa)	0
E_e (GPa)	22.83		E_{ve} (GPa)	210
η_e (GPa·h)	1150		p_{pore} (GPa)	0

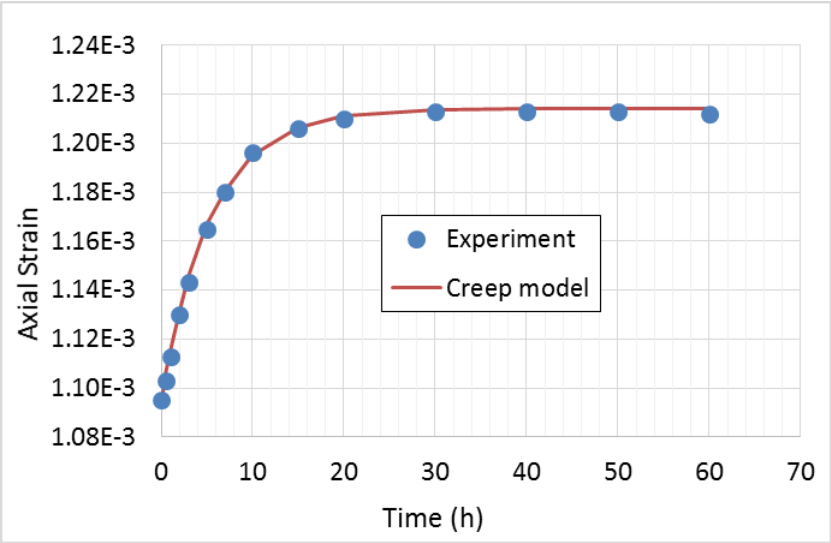

Figure 82: Creep strain model validated by uniaxial compression experimental data.

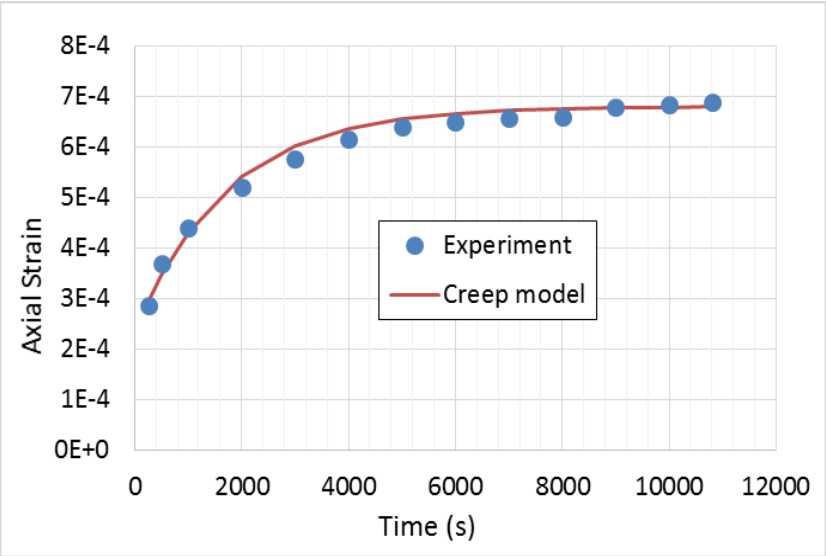

Figure 83: Creep strain model validated by triaxial compression experimental data.

After the strain equation is validated by experimental data above, the next step is to predict and validate the permeability change because of the creep phenomenon. However, unfortunately, extremely limited experimental data about creep permeability could be found from extensive literature review, especially for tight shale rock. Even though the presence of creep effects is recognized, most people don't choose to wait for a long time to conduct permeability measurements. Therefore, we determined to extract the measured permeability data from Chhatre et al. (2014), which are what we have found so far. Chhatre et al. used the steady-state method to measure liquid permeability for tight samples, and the effect of stress creep on liquid permeability measurements was investigated as well.

During the experiment, the fixed upstream and downstream pressure are used, and the flow rates are derived from one computer-controlled pump. Liquid was injected into the core plug by a pump from the upstream, and a back-pressure regulator was used at the

downstream. Steady-state flow is considered to be reached when the flow rate keep constant over a period of time. The liquid permeability measurements were conducted at room temperature and reservoir pore pressure. For the initial dry rock samples, the authors suggested to compare the total fluid volume injected with the pore volume of the core.

On Fig. 84, the blue dots represent the measured permeability data we extracted under constant net confining stress 2500 psi. The total organic carbon range was 0-12 weight percent, and the helium porosity was 4-17% for the tested core plugs. Unfortunately, the volume of clay and kerogen for the test sample were not included in the reference. Since both the rock parameters required for the creep permeability model and the exact measurement conditions have not been provided in Chhatre et al. (2014), we assumed an average value for elastic moduli, Poisson's ratio, and axial stress based on literature review. Then the viscosity coefficient η_e and viscoelastic moduli E_{ve} were adjusted to match the experimental data. Fluid pore pressure is neglected based on their experimental apparatus, where no fluid pump is available to provide pore pressure. The initial rock parameters for the creep permeability model were displayed in Table (13). On Fig. 84, the permeability calculated from the creep model is well matched with the experimental data. With provided rock parameters and approximate coefficients, the improved stress creep permeability model is capable of predicting the permeability decline along with time because of the creep phenomenon.

Based on the comparison of experimental data and model results above, several notes are worthy to be discussed as follows. Firstly, the impacts of stress creep on permeability measurement is significant for tight rock. Without considering the creep effects and waiting enough time for measurements, the permeability might be considerably overestimated. A practical approach is available to reduce the long measurement time, which is to load the samples in core holder under a certain net confining stress for about a few weeks before performing permeability measurements (Chhatre et al. 2014). Under that condition, the creep process has already been completed or stable, which should not lead an obvious influence on measured permeability.

Secondly, even though the proposed creep permeability model could predict approximate permeability decline caused by stress creep, the rock parameters are required to be evaluated or measured in advance, such as viscoelastic moduli and viscosity coefficient of rock samples. However, this manuscript mainly focuses on the physics mechanism and the concept model, so no measurement experiments have been conducted and discussed for the initial rock parameters. Additionally, no similar rock samples and equipment are currently available to our research group. But, the methods to measure these initial rock parameters in laboratory are briefly introduced as following.

Poisson's ratio can be obtained from direct measurement by using a strain measuring device. The elastic modulus E_e can be directly measured and calculated by dividing the loaded stress by the instantaneous strain. The viscoelastic modulus E_{ve} can be derived from the ultimate stable strain, which is equal to $\frac{\sigma}{E_e} + \frac{\sigma}{E_{ve}}$ based on Eq. (59). The viscosity coefficient of rock η_e can be derived from the increasing trend of strain in

the uniaxial compression creep process. On the other hand, these parameters are related to rock lithology and loaded stress. Therefore, the measurement results from one rock type cannot be directly used for another different rock type.

Thirdly, the stress creep highly depends on the rock composition, such as Total Organic Carbon (TOC) and clay content (Sone and Zoback 2011, Mighani et al. 2015). Their results show a higher TOC and clay content lead to a larger creep strain. We believe these soft materials including clay and TOC are correlated with viscoelastic modulus and viscosity coefficient. Before considering the creep effects, the permeability decline along with the increasing of effective stress is mainly caused by the closure of micro-fractures, shrinkage of pore space, and change of pore structure under stress compaction. These elastic behaviors occurred at instantaneous time are mostly involved with brittle materials, such as quartz, feldspars, and carbonates. The first term on right hand side of Eq. (59) represents this process. Then when the creep is taken into account, more strains are from the soft materials along with time.

During the primary creep stage, the increasing strains are from the closure of pre-existed micro-fractures and the compression of Nano-pores inside these soft materials, such as kerogen. As a result, an apparent decrease of permeability along with time was observed in Fig. 84. Next, during the secondary creep stage, the creep strain does not increase much because the micro-fractures and Nano-pores inside soft materials cannot be further compressed quickly. Consequently, the permeability does not decrease much and try to become stable over time. On the other hand, if the loaded stress is larger than the yield stress, the rock will be cracked, and more strains will be observed during the tertiary

creep stage. However, as we explained earlier, we mainly focus on the primary creep stage for permeability measurement in this study.

Fourthly, the ultimate and maximum strain is equal to $\frac{\sigma}{E_e} + \frac{\sigma}{E_{ve}}$ based on Eq. (59), which in return leads to an ultimate permeability over time based on Eq. (72). Both ultimate values are directly related to elastic modulus, viscoelastic moduli, and loaded stress. If the value of viscoelastic modulus is too large, the creep strain will be very small, and it can be ignored. Fifthly, the proposed creep strain and permeability model is a simplified solution to estimate the permeability change for permeability measurements, where the impacts of temperature, injection fluid, steady-state secondary creep state, heterogeneous rock properties have not been considered. Each of them above might have an obvious impact on the measurement results. Therefore, more experimental studies are required to better understand the stress creep cooperating with these different mechanisms and the impact on permeability measurements.

Table 13: Initial rock parameters for creep permeability model.

σ_{ax} (GPa)	1.034×10^{-3}		σ_c (GPa)	1.724×10^{-2}
E_e (GPa)	50		E_{ve} (GPa)	100
η_e (GPa·h)	3.6×10^4		p_{pore} (GPa)	0
v	0.3		r (1/Pa)	2.18×10^{-7}

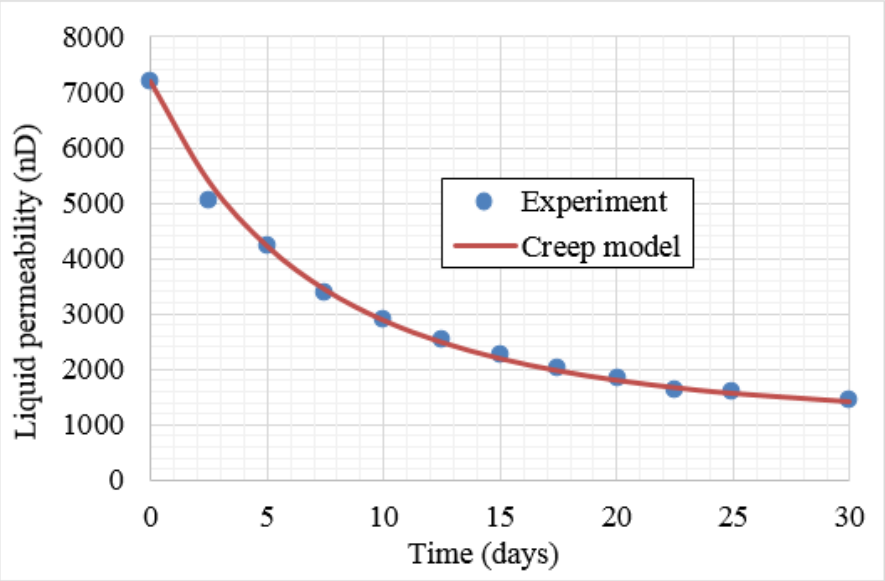

Figure 84: Improved permeability creep model validated by experimental data.

6.4 Effective Stress Coefficient

6.4.1 Path-dependent Effective Stress

Another important factor that could largely affect stress-dependent permeability measurements is effective stress coefficient. Let us firstly rewrite Eq. (54) for the condition of permeability measurement (Fig. 80a) as in Eq. (75). As we mentioned earlier, since the effective stress coefficient is close to one for most reservoir rocks based on Eq. (55), it has been just simply regarded as one in many reservoir studies. However, some experimental studies have already demonstrated the effective stress coefficient to be largely greater or smaller than one, especially for the rock containing much soft materials, such as clay and kerogen.

Zoback and Byerlee (1975) measured the permeability of the Berea sandstone and found pore pressure has a significantly larger effect on permeability than confining pressure, which means the effective stress coefficient $\alpha > 1$. They explained the permeability behavior under stress with the presence of highly compressible matrix materials. Fig. 85 shows the schematic of pore structure based on the above theory of Zoback and Byerlee, which is used to explain the large effective coefficient. Rock grains, indicated as gray color, usually have a low compressibility, such as quartz and feldspar. A layer of soft materials with high compressibility, which are highlighted as blue dots and red curves, is surrounding rock grain, such as clay and kerogen. Compressibility is defined as the fractional change of pore volume under a unit change in pressure.

According to Fig. 85, when an externally stress is applied on rock grain, a small strain will produce owing to its low compressibility. When that small strain is passed from rock grain to the layer of soft materials (from outside to inside), a small stress will be induced because of its high compressibility. Consequently, that small stress will only result in a small strain to the pore volume. The externally stress (or confining stress) has relatively little effect on the change of pore volume and strain. This is because the high compressibility materials, which locates between rock grain and pore space, largely weaken the compaction effect of external confining stress. However, the change of pore pressure could produce large pore stain because the pore stress change will directly apply on the high compressibility materials. Therefore, pore pressure has a considerably greater effect than external confining stress on the pore stain and permeability change, which leads to a larger-than-one effective stress coefficient. On the other hand, without these materials

with high compressibility, external confining stress will have an almost equal effect with pore pressure on the pore strain and permeability change.

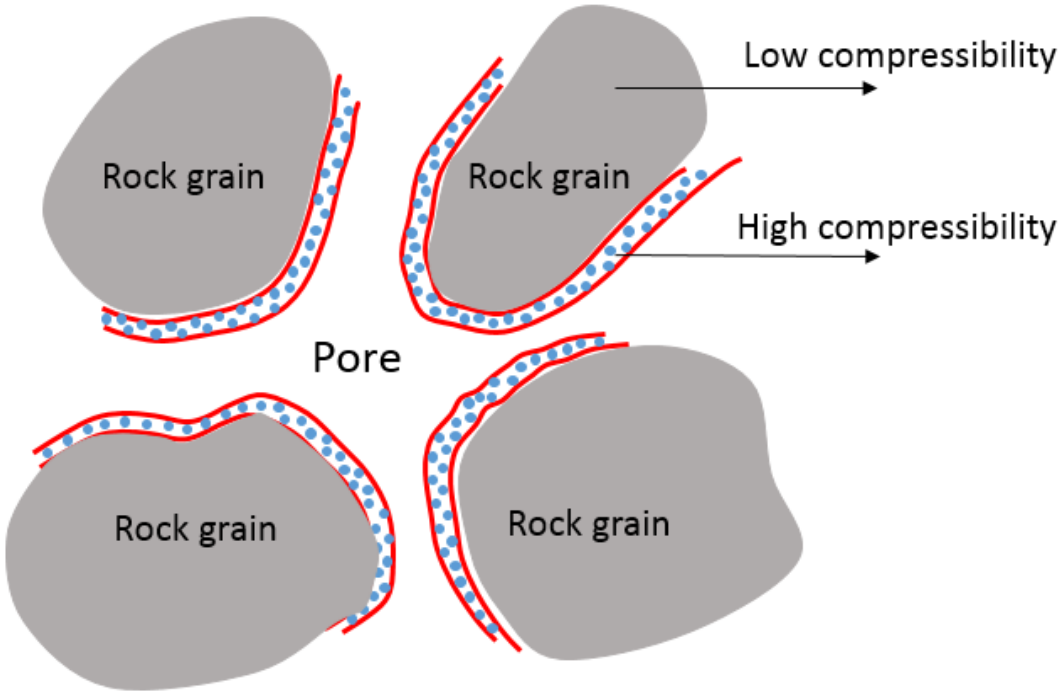

Figure 85: Schematic of pore structure with high compressible materials.

Al-Wardy and Zimmerman (2004) presented a similar model of clay-rich sandstones to explain the relative sensitivity of permeability to pore pressure and confining pressure. In their model, the clay is distributed in the form of particles that are only tangentially attached to the pore walls. They assumed the presented clays will have essentially no influence on the effect that the confining stress has on pore strain. In other words, an increase of confining stress will cause a same deformation of pore volume no matter the clays were present or not. However, on the other hand, the change of pore pressure will cause a displacement on the clay particles (compression or expansion), which

will in return affect the change of entire pore volume. Both models above predict that the permeability will be much more sensitive to the change in pore pressure than to the change in confining pressure, which indicates effective stress coefficient is larger than one. Additionally, although the two models above are highly ideal, both pore-lining clays and discrete clay particles are indeed frequently observed in cores of sandstones by scanning electron microscopy (Neasham 1977).

Based on similar permeability measurements on sandstone, Walls and Nur (1979) reported the effective stress coefficient has an apparent positive correlation with clay content, where α varies from 1 to as large as 7.1 depending on the clay content. Kwon et al. (2001) measured the permeability of illite-rich shale from the Wilcox formation as a function of effective pressure. Their measurements found the effective stress coefficient $\alpha \approx 1$ for shale with a clay content of around 45%. Heller et al. (2014) conducted laboratory experiments on gas shale to investigate the effects of confining stress and pore pressure on matrix permeability. Their results indicate the matrix permeability of gas shale is more sensitive to changes in confining pressure than changes in pore pressure, which means the effective stress coefficient $\alpha < 1$.

On the other hand, not all rock types are applicable to Eq. (55) for calculating effective stress coefficient, because it was derived with some presumptions. For example, the rock components were assumed homogenous, which ignored the large difference of properties among different components, such as quartz, feldspar, kerogen, and clay. In other words, we cannot simply use Eq. (55) to calculate effective stress coefficient for the rock containing many special components. Experimental measurements are the most

accurate method to obtain the effective stress coefficient, which will be introduced in detail soon. In the study of this chapter, we don't argue if the effective stress coefficient should be larger, smaller, or equal to one. What we want to highlight are two points: 1) the effective stress coefficient is not always equal to one, and we need to carefully derive it with correct experimental measurements; 2) the effective stress coefficient is highly related to the content of clay and kerogen because of their high compressibility.

$$\sigma_e = p_c - \alpha \times p_{pore} \tag{75}$$

Where σ_e is the effective stress, p_c is the confining stress, p_{pore} is the internal pore pressure, α represents the effective stress coefficient.

Let us use a simple example to explain why the effective stress coefficient is significantly important for predicting permeability change during reservoir depletion. There are two paths resulting in an increase of effective stress based on Eq. (75): increase confining pressure and decrease pore pressure. According to Fig. 80, we mentioned the confining pressure is often altered to change the effective stress on most steady-state permeability measurements. However, the reservoir pore pressure is decreased caused by hydrocarbon production to increase the effective stress. Obviously, the traditional experiments and real reservoir production follow two different paths to change the effective stress applied on formation rocks.

Assuming the permeability will reduce by 30% if the effective stress increase 1000 psi. Based on that, the reservoir permeability will decrease by 30% with the pore pressure drop of 1000 psi based on Eq. (75) if the effective stress coefficient is equal to one. However, supposing the effective stress coefficient is equal to two, the reservoir

permeability will decrease much more than 30% with the exactly same pore pressure drop of 1000 psi. This is because the effective stress is increased 2000 psi based on Eq. (75). Comparing the two cases, different stress coefficient brings large difference on the change of effective stress and permeability in terms of same pore pressure drop during reservoir depletion. On the other hand, if the pore pressure is altered to change the effective stress on permeability measurements under constant confining pressure, no such difference will exist no matter what value the effective stress coefficient is. Therefore, it is highly recommended to change pore pressure for stress-dependent permeability measurements, which of course requires more sophisticated and expensive experimental apparatus.

To calculate the effective stress coefficient, Bernabe (1986) introduced Eq. (76) based on the ratio of slope method, where the change of permeability with change in pore pressure is divided by the change of permeability with change in confining pressure. On Eq. (76), the numerator should be positive, and the denominator should be negative. This equation should be applicable to all rock conditions, no matter effective stress coefficient will be larger, equal, or smaller than one. Based on the same logic, Boitnott et al. (2009) presented three different permeability measurements to evaluate the effective stress coefficient in a similar fashion shown as Fig. 86, where α can be derived from any two of the measurements.

Additionally, whether α is equal to one or not can be easily determined by conducting the permeability measurement (left side), where both pore pressure and confining pressure are simultaneously changed in an equal amount. However, unfortunately, only the permeability measurement (right side) has been widely used,

where only confining pressure is changed and pore pressure is typically kept at a low and constant value. The temporary benefit is less experimental time and easier laboratory equipment. Furthermore, as we discussed on the previous sections, enough time should be given to permeability measurements in order to mitigate the creep effect. Repeated core measurements should be conducted multiple times to ensure the accuracy and avoid the measurement error.

$$\alpha = -\frac{\left(\frac{\partial k}{\partial p_{pore}}\right)_{constant\ p_c}}{\left(\frac{\partial k}{\partial p_c}\right)_{constant\ p_{pore}}} \tag{76}$$

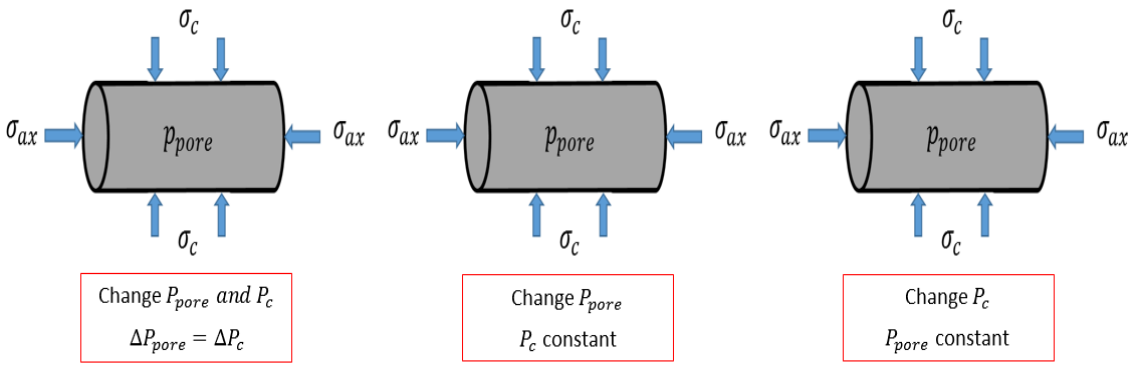

Figure 86: Three different permeability measurements for evaluating effective stress coefficient.

Two different data examples are introduced below to present the impact of effective stress coefficient and how we might use it to correctly interpret our measured-permeability data. Heller et al. (2014) measured permeability at different pore pressure and confining pressure for six shale samples. Helium was used as the test gas to avoid the potentially significant effects of gas adsorption and swelling for all measurements. Based

on the permeability value of the samples, both steady-state flow method and pressure pulse decay method were applied. The measurement results of Barnett 31 are extracted from their publication and plotted on Fig. 87. Under four constant pore pressures from 1000 to 4000 psi, confining pressure is scheduled to change from 2000 to 8000 psi to achieve effective stress ranging from 1000 to 4000 psi.

If the effective stress coefficient is simply assumed one without much consideration, the results are shown on Fig. 87(a). The stress-dependent permeability follows different curve paths, which leads to difficulties in predicting the function of permeability change. Additionally, since the measurements were from the same formation rock, they are supposed to follow a same function curve. By using a less effective stress coefficient 0.68, all measured data follow a unique stress-permeability function curve as in Fig. 87(b), which provides a consistent interpretation of stress-dependent permeability. The small effective stress coefficient means the change of permeability and effective stress are more sensitive to the change in confining pressure than pore pressure.

Rock measurements in laboratory are a critical way to evaluate permeability and predict the dynamic production performance. On the other hand, as we have already introduced in the chapter five, Pressure Transient Analysis (PTA) is often conducted for reservoir characterization as well, where bottom hole pressure is typically collected from pressure gauges to evaluate the product of permeability and thickness and skin. Therefore, the permeability derived from Pressure Transient Analysis is usually used to compare with the permeability measured from core samples in laboratory. Based on the same formation rock, the permeability change trend derived from both methods should follow the same

stress-dependent function law. However, unfortunately, we have not found any PTA-derived permeability at various effective stresses for shale reservoirs from literature review. Therefore, we decided to use some available permeability data from the chapter five, which is for one Gulf of Mexico Deepwater reservoir.

The permeability data were extracted from Shumbera and Wang (2008), and they are plotted on Fig. 88(a), where permeability reduction factor on y axis is defined as the ratio of permeability at certain effective stress to the initial permeability. Blue dots represent permeability measured from core experiments, and red triangles stand for permeability derived from Pressure Transient Analysis (PTA). Both curves show the permeability largely decreases along with the increase of effective stress, but they follow different curve paths. Different possible mechanisms have been proposed to explain that difference (Pourciau et al. 2005), but the real reason hasn't been figured out yet. Due to the presence of large amount of clay in core samples, we assume effective stress coefficient as two. Then effective stress is recalculated, and the results are plotted in Fig. 88(b), where all stress-permeability data follow a same curve trend.

Apparently, when the effective stress coefficient is equal to two, the two permeability data sets are fitted on a unique curve trend, which provide a consistent interpretation to permeability change under compaction. It should be noted that the larger effective stress coefficient just provides a possible mechanism to explain the permeability loss trend difference between core measurements and Pressure Transient Analysis. More data from different wells and the same reservoir formation are definitely required to validate this mechanism. On the other hand, even though Gulf of Mexico Deepwater

reservoir used above is significantly different from shale reservoirs, the common point is the large presence of high compressibility materials, such as clay, which could lead to large effective stress coefficient. Therefore, more attention should be given to the effective stress coefficient for rich-clay or rich-kerogen shale reservoirs, especially for similar cases as explained above.

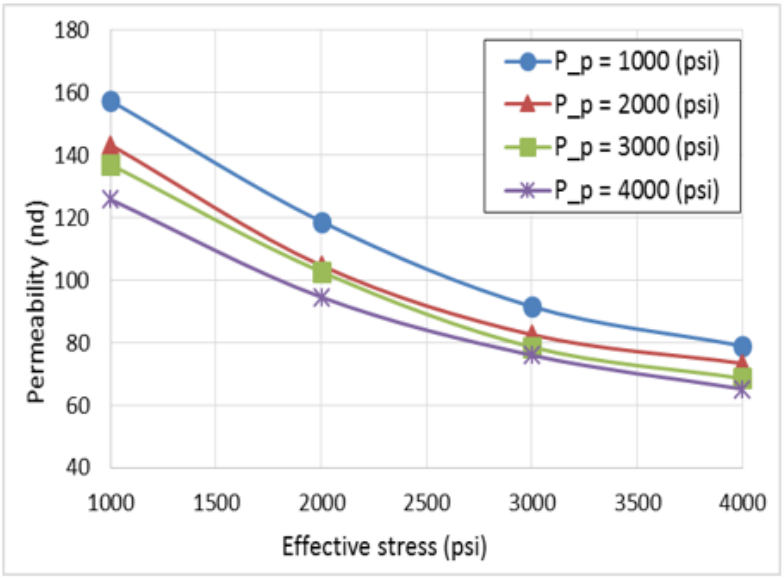

(a) $\sigma_e = p_c - p_{pore}$

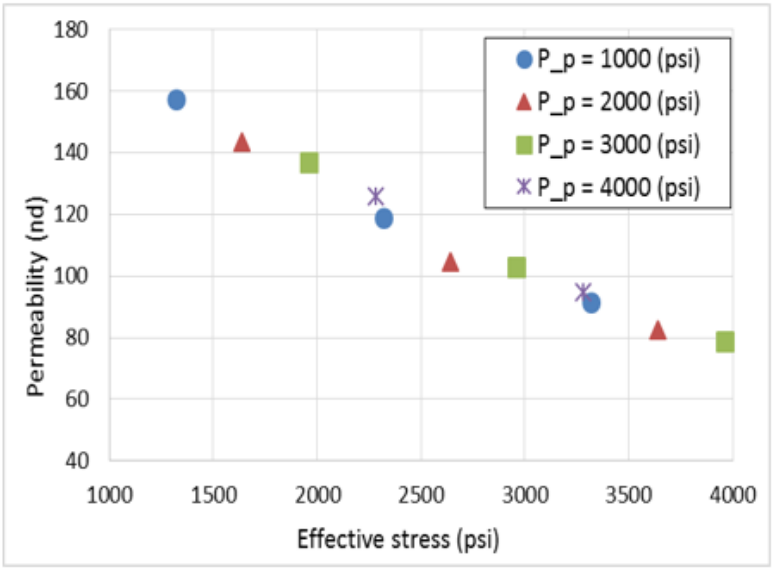

(b) $\sigma_e = p_c - 0.68 \times p_{pore}$

Figure 87: Measured permeability versus effective stress under different pore pressures for two coefficients α.

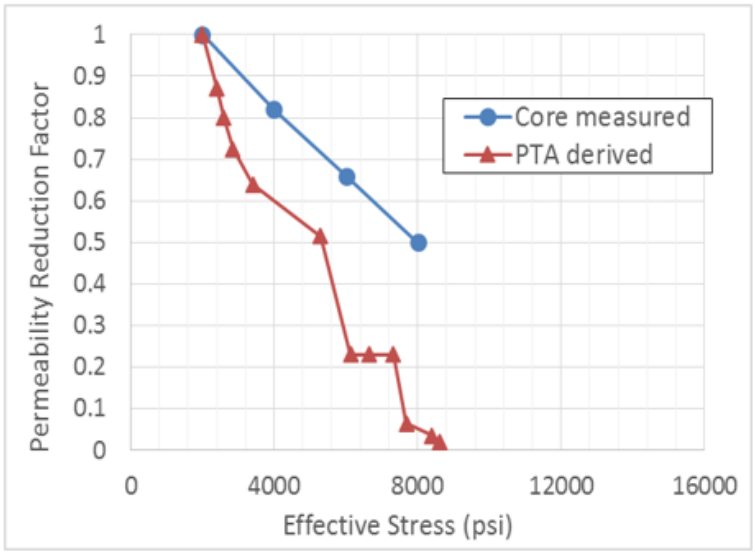

(a) $\sigma_e = p_c - p_{pore}$

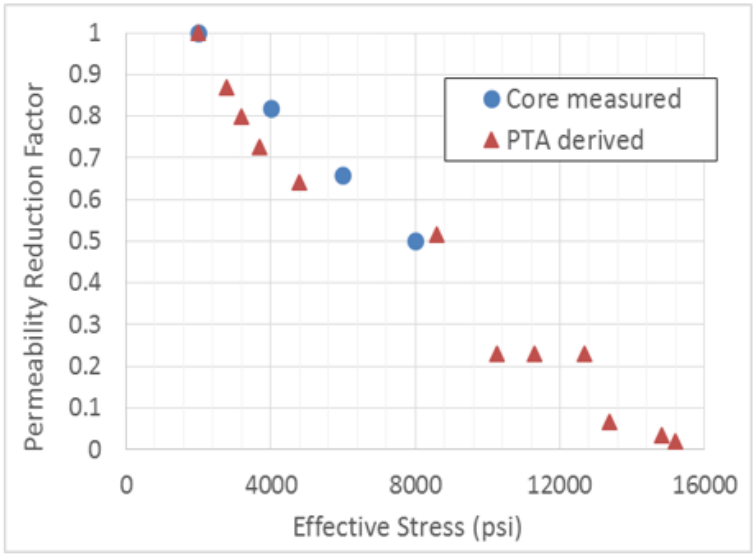

(b) $\sigma_e = p_c - 2 \times p_{pore}$

Figure 88: Comparison of core-measured and PTA-derived permeability loss trends for Gulf of Mexico reservoir.

6.4.2 Numerical Simulation Results

In order to present the impact of effective stress coefficient on stress-dependent permeability and production performance, the developed coupled flow-geomechanics model will be used, where both stress-dependent permeability and stress-strain correlation are considered. The governing mass conversation equation for flow is presented as Eq. (1), and the governing stress equilibrium equation is presented as Eq. (13). The sequential fixed-stress split scheme is used for the coupled system, where the flow equation is solved first for pressure variable, and then the mechanics balance equation is solved for displacement variable. The effective stress coefficient or the Biot's coefficient is used in two parts of this coupled model: one is for the coupling Eq. (19) and (20), and the other is to calculate effective stress for stress-dependent permeability.

Fig. 89 presents the synthetic mesh schematic of the 2D coupled model, where the gray grids stand for wellbore, the deep green grids are hydraulic fractures, and the rest white grids stand for shale matrix. There is no direct connection between matrix grids and wellbore, which means hydrocarbon must flow from matrix into hydraulic fracture first, and then flow into wellbore. Since the objective is to present the impact of effective stress coefficient on cumulative production, a single oil phase is used in the coupled model for simplicity. For the geomechanics modulus, the hybrid stress and displacement boundary conditions are used. The horizontal displacement is not permitted for the left boundary and the vertical displacement is not permitted for the bottom boundary. Simultaneously, a constant overburden stress is applied on both top boundary and right boundary as

confining stress. In addition to pressure gradient caused by bottom hole pressure, the confining stress could be another driver to push pore fluid into wellbore.

Table (14) shows the initial condition of rock and fluid for the coupled model, where different rock properties are assigned to matrix and fractures. The initial reservoir pressure and bottom hole pressure are given, so the production rate will be calculated based on the pressure gradient. The pressure of horizontal wellbore is assumed to be constant and equal to the bottom hole pressure. The cumulative production is calculating by adding all of the production from hydraulic fractures to the wellbore. The temperature is assumed constant all the time for our model which means no heat transfer and waste occurred. Young's modulus and Poisson's ratio are provided as well for the geomechanics modules. During the reservoir production, the reservoir pressure decreases, and the net effective stress increases.

Based on the exponential function of Eq. (71), the stress-dependent permeability curve is shown in Fig. 90, where the x axis is the increase of effective stress and y axis is the normalized permeability. The exponential curve equation is presented as well, where the stress sensitivity coefficient is equal to $2 \times 10^{-4}\ 1/psi$. Four cases with different effective stress coefficients are performed: $Alpha = 0.4, Alpha = 0.8, Alpha = 1.0, Alpha = 1.5, Alpha = 2.0$. Based on Eq. (75), the value of effective stress coefficient determines how much effective stress change caused by the change of pore pressure.

Therefore, by using the same exponential equation shown in Fig. 90, the pore pressure dependent permeability trends for different effective stress coefficients are presented in Fig. 91, where the x axis is the decrease of pore pressure. When $Alpha =$

1.0, the pore pressure dependent permeability from Fig. 91 is the same with the stress dependent permeability curve on Fig. 90. This is because the change of effective stress is equal to the change of pore pressure. When $Alpha > 1.0$, the permeability declines more severe with the same amount of pore pressure drop, which in return leads to less flow productivity.

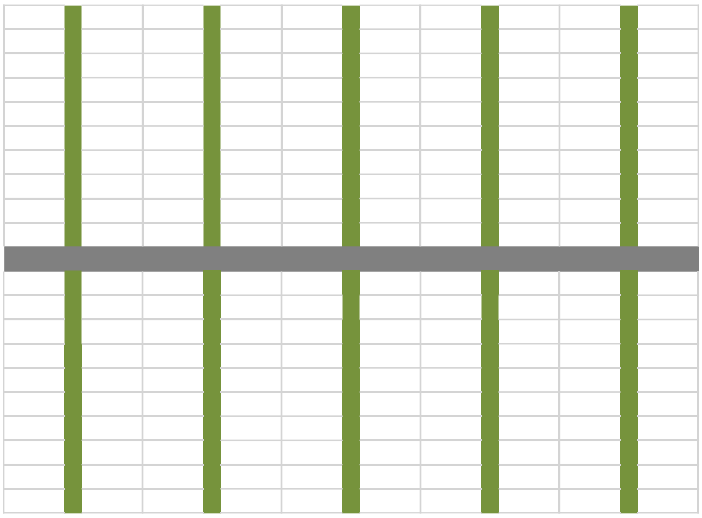

Figure 89: Mesh schematic of 2D coupled model including fracture network.

Table 14: Initial condition of rock and fluid for the coupled model.

Initial Parameters	Values
Reservoir pressure	3.103×10^7 (Pa)
Matrix porosity	7%
Matrix permeability	7.895×10^{-19} (m^2)
Fracture permeability	7.895×10^{-14} (m^2)
Reservoir Temperature	366.48 (K)
Bottom hole pressure	1.034×10^7 (Pa)
Fluid viscosity	8×10^{-4} (Pa·s)
Fluid compressibility	7.252×10^{-10} (1/Pa)
Poisson's ratio	0.3
Young's modulus	3×10^9 (Pa)
Overburden stress	3.103×10^7 (Pa)

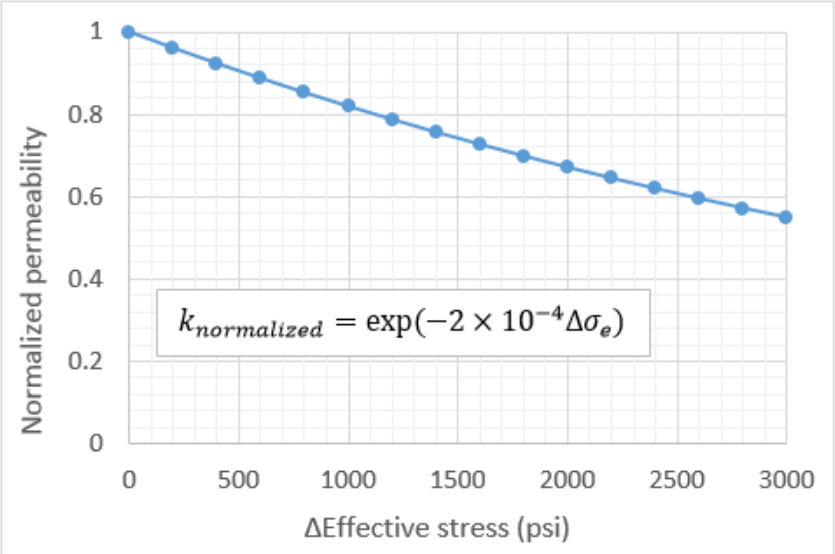

Figure 90: Stress-dependent permeability based on exponential law for the coupled model.

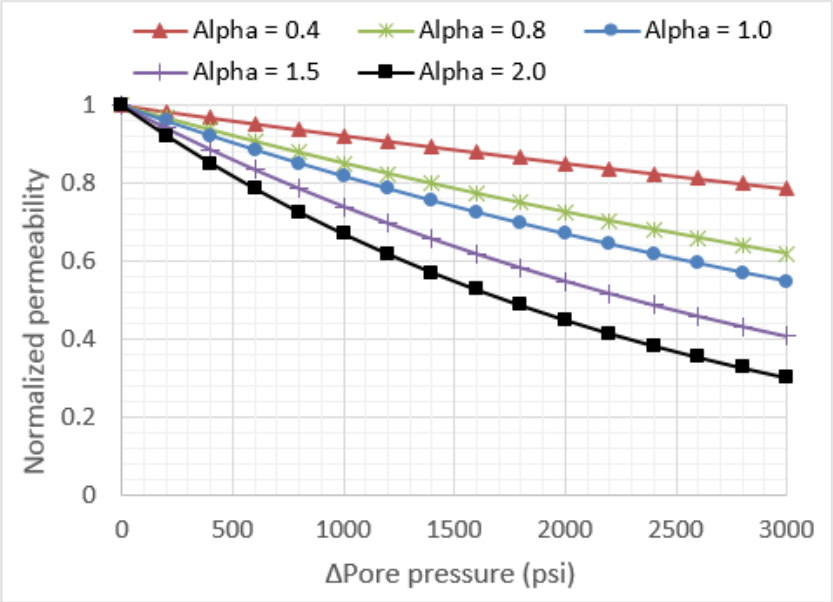

Figure 91: Pore pressure dependent permeability trends for different effective stress coefficients (Alpha).

After the coupled flow-geomechanics model is used for the five reservoir cases with different effective stress coefficients, Fig. 92 shows the results of pressure distribution at a chosen time of 1.30×10^5 (s). The color value bar is the same for the five pressure images, where blue color stands for low pressure and red color represents high pressure. Due to high flow conductivity, the wellbore and hydraulic fractures have already reached the provided bottom hole pressure for all the five cases. However, the matrix pressure is quite different for the cases with different effective stress coefficients because of dissimilar permeability decline displayed as on Fig. 91.

The higher the effective stress coefficient is, the higher the matrix pore pressure maintains. When effective stress coefficient is small, such as 0.4, the reservoir permeability does not reduce much along with the decrease of pore pressure.

Consequently, the pore fluid is easily drained out and produced, which leads to a decrease of pore pressure. When effective stress coefficient is large, such as 2.0, the permeability significantly reduces along with the drop of pore pressure. As a result, the pore fluid is difficult to be drained out and the pore pressure is maintained at a high level.

Fig. 93 presents the results of cumulative production versus time for four different effective stress coefficients, where x axis is time and y axis is cumulative production mass. The original point of this plot is not (0, 0) in order to distinguish the differences between these cases. Two important points are observed from this plot. First, a smaller alpha result in a less increase of effective stress, which leads to a less decrease of permeability. Consequently, the reservoir reaches the final pressure-stable condition, which is defined when the entire reservoir pressure is equal to the bottom hole pressure and there is no pressure gradient for fluid flow any more, in a relative short time for a small alpha case because of high flow conductivity. For example, the case of 0.4 takes about 1.7×10^5 seconds to reach the final pressure-stable condition, while the case of 2.0 needs about 5.7×10^5 seconds.

Second, a larger alpha case predicts a higher cumulative production. To the single-phase flow simulation, the driving forces of production are both pore pressure depletion and effective stress acted on rock surface. For the case with larger alpha, a unit of pore pressure decline leads to bigger increase of effective stress, which in return provides larger force to squeeze pore fluid as production. Therefore, even though the pore pressure depletion is the same for all four cases, the case with larger alpha still predicts a higher cumulative production.

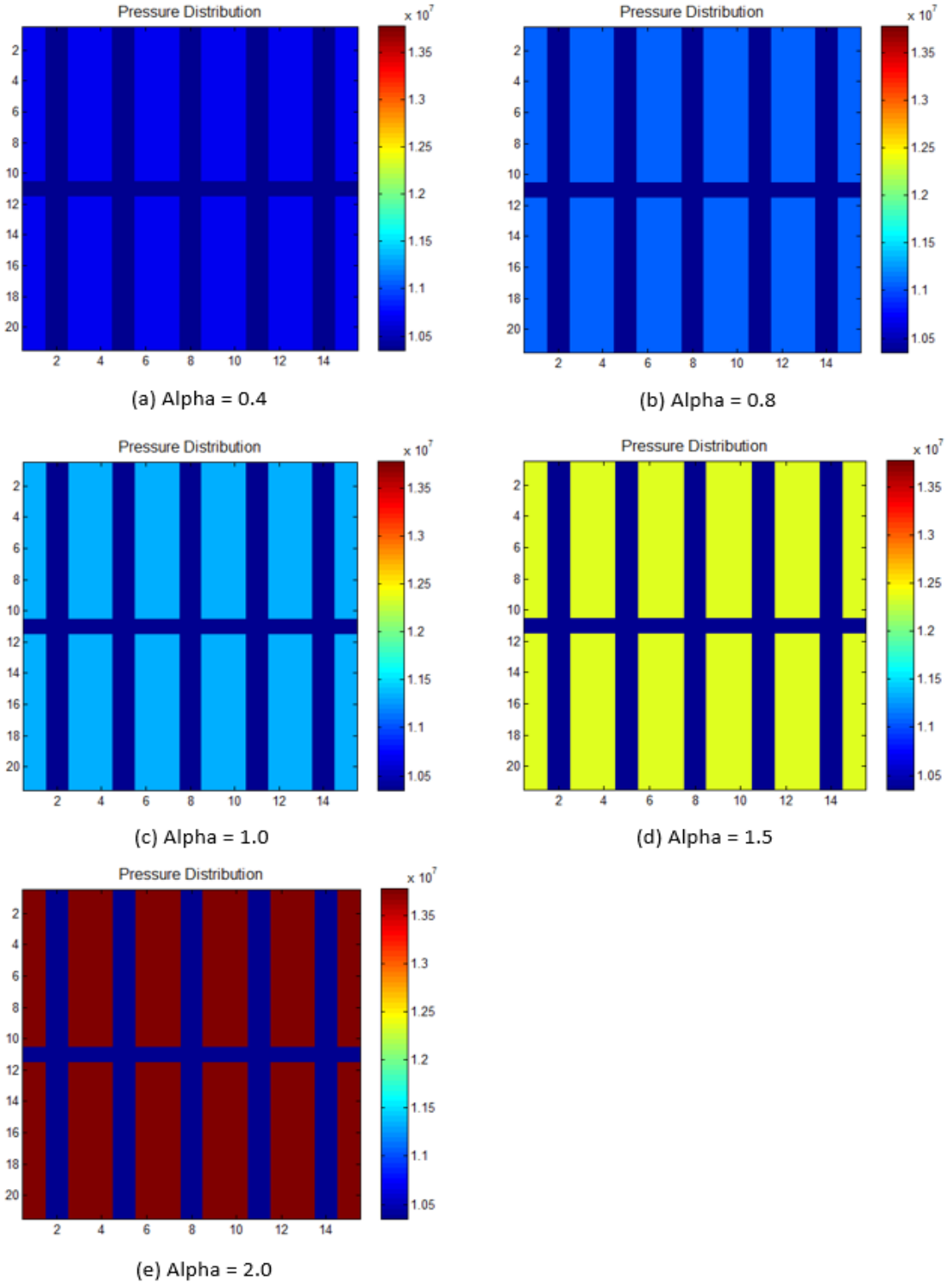

Figure 92: Pressure distribution of reservoir mesh for different effective stress coefficients (Alpha).

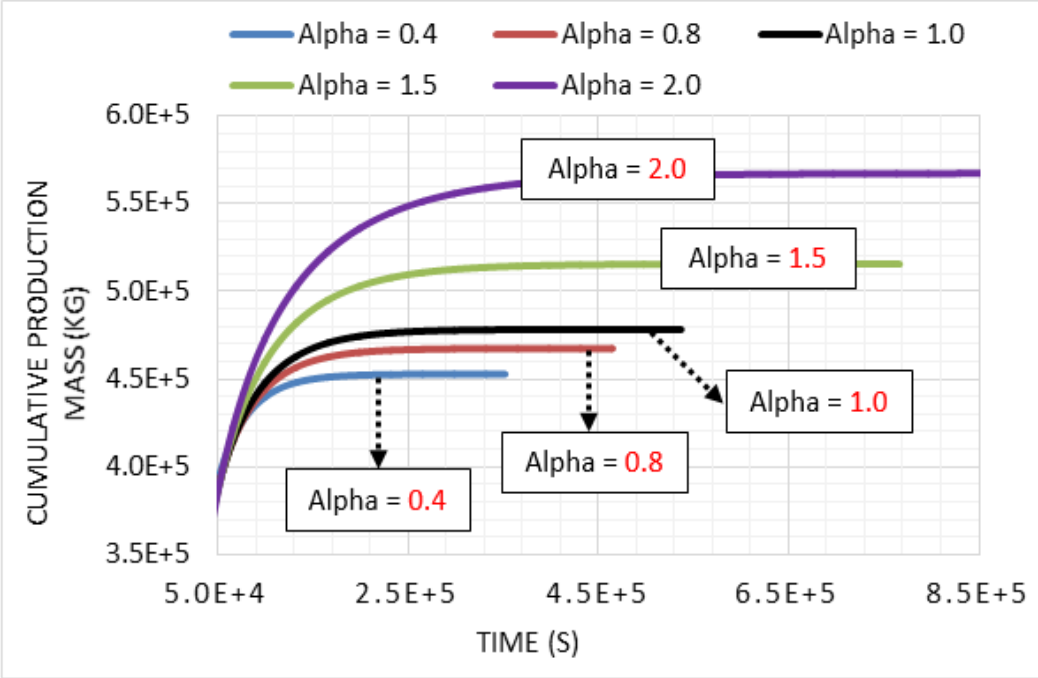

Figure 93: Cumulative production versus time for different effective stress coefficients (Alpha).

6.5 Conclusions and Discussions

The stress creep phenomenon could significantly affect permeability measurements for the shale rock samples containing rich kerogen or clay content. Based on the time-dependent behavior of compaction creep, the creep strain model has been introduced to calculate the creep strain over time, where the primary creep stage is primarily considered, and the creep strain is contributed by instantaneous strain and viscoelastic strain. The stress creep highly depends on rock compositions, and it is positively related with the content of kerogen and clay. Additionally, the creep strain

model was validated by comparing with experimental data of both a uniaxial and triaxial compression creep test.

On the other hand, the stress change caused by the creep is derived from triaxial compression test theory for typical permeability measurements with core plug. By inserting the stress change into an exponential permeability function, the improved stress-dependent permeability model was obtained, which is capable of predicting the measured permeability decline under constant stress along with time caused by the stress creep mechanism. The improved stress-dependent permeability model was validated by comparing with measured oil permeability data. To apply the proposed creep strain and improved permeability models, the initial rock parameters are required to be measured or evaluated in advance.

In terms of the effects of stress creep on permeability measurements, three different approaches are available to roughly eliminate the error: 1) measure rock permeability at different stresses and wait for a relative long time until the permeability reaches stable; 2) load the rock sample with a certain confining stress in core holder for about several weeks before conducting permeability measurements; 3) Apply the proposed permeability model to calculate the impacts caused by the time-dependent creep strain. The schedule management and time issue are the challenges for the first two approaches above. The challenge for the third method is to evaluate the rock parameters by the compression-strain experiments. Additionally, the proposed permeability model is relative simple because some other impact factors have not been considered in the mathematical equation, such as temperature, secondary creep stage, injection fluid, and heterogeneous

rock properties. More experimental data are required to improve the understanding and knowledge gap.

Effective stress coefficient is critical to correctly interpret and apply the stress-dependent permeability measured from laboratory into reservoir-field applications. More importantly, effective stress coefficient is not equal to one for some shale rock types. Effective stress coefficient is highly related to the content of clay and kerogen because of their property of high compressibility. As two previous examples show, an approximate effective stress coefficient could better explain the permeability decline trend and match the permeability data between core measurements and pressure transient analysis. The equation calculating effective stress coefficient is introduced, followed by the design of three different permeability measurements. In a word, permeability should be measured under a series of both pore pressures and confining pressures.

A coupled flow-geomechanics model has been applied to investigate the effect of different effective stress coefficients on permeability change and cumulative production. The pressure distribution of reservoir mesh is presented for the cases with different effective stress coefficients. A large effective stress coefficient (larger than one) means the variation of effective stress is more sensitive to the change of pore pressure than confining pressure. Consequently, a certain drop of pore pressure will lead to a large permeability decline during reservoir depletion. Based on the simulation results, the small effective stress coefficient case is much quickly to reach the final pressure-stable condition, also known as pressure convergence.

On the other hand, the case of larger effective stress coefficient could provide higher cumulative production owing to stronger compression from effective stress. To be noted, this conclusion above is sensitive to the reservoir mesh size. For the area of only stimulated reservoir volume, the larger cumulative production is obtained as shown on Fig. 93. This is because the entire area could be drained until the reservoir pressure reaches the given bottom hole pressure. However, if the large unstimulated reservoir area is included, the result might be different, and more studies are required. Due to extra-low permeability of shale matrix, the pore fluid cannot be effectively produced even with enough pressure gradient, especially when the permeability still keeps decreasing during reservoir production.

CHAPTER VII

CONCLUSIONS AND RECOMMENDATIONS

7.1 Conclusions

In this work, an in-house mathematical simulator coupling fluid flow and geomechanics behaviors has been developed on FORTRAN. How to derive the governing equations of the coupled model and solve them by numerical methods was introduced in detail. The coupled simulator was validated by comparing with the analytical solutions of Terzaghi's consolidation problem and Mandel's consolidation problem. In addition, the developed coupled simulator has been applied to various reservoir applications, where different flow mechanisms and geomechanical effects were considered. Based on the results of previous chapters, some major conclusions are presented as follows to summarize this study:

1) If the stress-dependent permeability is considered, the permeability and cumulative production will be significantly reduced. Additionally, the production loss is highly dependent on the selected permeability correlations and their coefficients.
2) The matrix shrinkage on organic matter could rebound the permeability and improve the cumulative production at the low reservoir pressure stage. However, the impact of matrix shrinkage on cumulative production is quite limited, which is largely related to Total Organic Carbon, the correlation coefficients, gas desorption pressure, and bottom hole pressure.

3) When the adaptive time stepping method is implemented for the coupled model, the total computational time is significantly reduced and the simulation accuracy is maintained as well.
4) Choosing a proper error tolerance of displacement is really important to optimize the time step size for the modified local error method. Also, how to modify the time step size plays an important role in the stability and computational efficiency for the coupled model.
5) Irreversible compaction processes are obviously observed in thin section micrographs, which could result in the hysteresis of rock compressibility and permeability.
6) The compaction processes can be generally divided into two phases for Gulf of Mexico Deepwater unconsolidated reservoirs: consolidation and deformation.
7) The stress-dependent permeability largely reduces the cumulative hydrocarbon production for GOM Deepwater reservoirs, and the permeability decline is mainly caused by pore pressure drop and irreversible compaction.
8) Based on the pressure buildup tests, the reservoir permeability derived from the Horner Plot method is smaller when the stress-dependent permeability is considered.
9) With considering a compaction table, the permeability derived from history matching bottom hole pressure is larger, and the predicted critical production rate is smaller.

10) Based on the time-dependent behavior of compaction creep, a creep strain model was introduced to calculate the creep strain over time, which is contributed by instantaneous strain and viscoelastic strain.
11) Based on the typical permeability measurements with core plugs, an improved stress-dependent permeability model was derived to predict the measured permeability decline under constant stress along with time caused by the stress creep mechanism.
12) The effective stress coefficient is critical to correctly interpret and apply the stress-dependent permeability measured from laboratory into reservoir-field applications, where the effective stress coefficient cannot be simply assumed one for some shale reservoir rock, especially for the rock containing much clay or kerogen.

7.2 Recommendations

Inspired by the investigation and the results of this study, some recommendations are provided for future work:

- Natural fractures and carbonates are extensively observed in core samples of the Eagle Ford shale, while both of them behave differently with the primary shale matrix under compaction stress, especially for the permeability change. The coupled simulator could be applied to investigate the effects of natural fractures and carbonates on permeability upscaling.

- The parallel computing is essential for both scaling and execution on advanced architectures, especially for the coupled model, where a significant amount of computation is required for the geomechanics module. Therefore, future work could go to identify steps necessary for implementation of parallelization techniques, such as parallel solver, domain decomposition, and combined MPI-OpenMP approach.
- The coupled flow and geomechanics simulator could be more flexible, where no major changes are required for the governing equations of flow and geomechanics. To build a third-party shared platform, the individual flow simulation or the geomechanics module could be easily coupled with commercial geomechanics software or pre-existed reservoir flow simulation.
- Another interesting topic is to build two different grid meshes for the coupled model: one mesh is for reservoir simulation, and the other mesh is for geomechanics. One major benefit is the geomechanics mesh could include the reservoir rock above and below the targeted hydrocarbon zone in order to investigate their displacement change, such as surface subsidence.
- The linear elasticity deformation is assumed for the coupled model of this study. Therefore, nonlinear plastic deformation could be considered for better describing some compaction behaviors, such as fracture propagation.

7.3 Unique Contributions of This Study

The coupled flow and geomechanics simulator has been developed by me from the scratch, and the main procedures include: 1) derive governing equations based on mass balance and momentum balance; 2) solve nonlinear governing equations by integral finite difference method and finite element method; 3) write code on FORTRAN and debug the program; 4) test and validate the coupled simulator. However, even though a significant amount of time was spent to these procedures above, developing the coupled stimulator is not new and unique. The major highlights and contributions of this study are the applications of the developed coupled simulator into different reservoir formations, where various and unique physics mechanisms and geomechanics effects are proposed to describe and interpret some uncommon compaction-related reservoir problems. Generally speaking, the unique contributions of this study are briefly described as follows:

- Based on different rock properties and compaction behaviors, various stress-permeability correlations are separately applied into different sub-pore media (organic matter, non-organic matter, and natural fractures).
- The matrix shrinkage phenomenon is considered for organic matter, and its impacts on permeability change and cumulative production are investigated.
- An adaptive time stepping method is introduced to improve the computational efficiency of the coupled model, where the time step size is dynamically adjusted based on the change of displacement.

- Irreversible compressibility and permeability hysteresis are proposed to explain the difference of permeability loss trends between field-derived and laboratory-measured permeability for Gulf of Mexico Deepwater reservoirs.
- An improved stress-dependent permeability model is derived to consider the effect of time-dependent compaction behavior on permeability measurements by incorporating the stress creep mechanism.
- The effective stress coefficient is studied in detail, especially when $\alpha > 1$. The impacts of effective stress coefficient on the interpretation of stress-dependent permeability measurement results and the prediction of field permeability change are investigated.

NOMENCLATURE

h_l	Specific enthalpy of component l
A_{nm}	Common surface between grid n and m
C_R	Heat capacity of dry rock
C_{dr}	Elasticity tensor
D_g	Gas diffusivity coefficient
E_e	Elastic modulus
E_{ve}	Viscoelastic modulus
F_{global}	Global force vector
F_{grid}	Local force vector
K_R	Thermal conductivity of rock
K_c	Constrained modulus
K_d	Dry rock bulk modulus
K_g	Thermal conductivity of gas
K_{global}	Global stiffness matrix
K_{grid}	Local stiffness matrix
K_o	Thermal conductivity of oil
K_s	Bulk modulus of solid grain
K_w	Thermal conductivity of water
M_h	Heat accumulation

P_L	Langmuir pressure
P_g	Gas pressure
P_{well}	Pressure of block containing the well
P_{wf}	Flowing bottom hole pressure
$R_n^{l,t+1}$	Residual of component l at time step $t+1$ for grid block n
V_L	Langmuir volume
V_n	Volume of grid n
c_f	Pore fluid compressibility
c_g	Gas compressibility
c_t	Total compressibility
c_v	Consolidation coefficient
k_i	Initial permeability
k_{rl}	Relative permeability of component l
k_s	Permeability of damaged zone
$\dot{m}$	Fluid mass per unit bulk volume
p_{pore}	Pore pressure
r_s	Radius of penetration damage zone
r_w	Wellbore radius
t_{next}	Size of next time step
t_p	Production time before well shut-in
u_c	Coarse displacement

u_f	Fine displacement
u_{global}	Global displacement vector
u_{grid}	Local displacement vector
u_x	Displacement in horizontal direction
u_y	Displacement in vertical direction
v_f	Pore fluid velocity
$x_{i,p+1}$	Primary variable in grid block i
ε_1	Relative convergence criterion
ε_u	Error tolerance of displacement
ε_v	Volumetric strain
η_e	Viscosity coefficient of material
$\rho_{g_{std}}$	Gas density at standard pressure and temperature
ρ_b	Bulk density
ρ_f	Pore fluid density
ρ_s	Density of solid phase
σ_c	Confining stress
σ_e	Effective stress
σ'_m	Mean effective stress
σ_v	Total mean stress
ϕ_i	Initial porosity
ϕ_r	Residual porosity

Δt	Size of time step
Δx	Grid block size
BHP	Bottom Hole Pressure
GOM	Gulf of Mexico
PTA	Pressure Transient Analysis
SEM	Scanning Electron Microscope
STB	Stock Tank Barrel
TOC	Total Organic Carbon
B	Skempton's pore pressure coefficient
E	Young's modulus
F	Mass flux
G	Shear modulus
I	Rank-2 identity tensor
M	Mass accumulation
Q	Source and sink
U	Specific internal energy
WI	Well index
ax	Axial direction
b	Klinkenberg factor
e	Element number
g	Gravitational acceleration
i	Element node number

k	Rock permeability
$lateral$	Lateral direction
n	Number of time step
p	Pore pressure
q	Volume flow rate of source and sink
s	Skin factor
t	Time
u	Displacement vector
v	Poisson's ratio
w	Weighting function
α	Biot coefficient (effective stress coefficient)
δ	Relative local error
ε	Strain tensor
μ	Fluid viscosity
σ	Total stress
ϕ	Rock porosity

REFERENCES

Abousleiman, Y., Cheng, A.H.-D., Cui, L., Detournay E., and Roegiers, J.C. 1996. Mandel's problem revisited, Ge´otechnique, 46, 187-195.

AI Ismail MI, Zoback MD. 2016. Effects of rock mineralogy and pore structure on stress-dependent permeability of shale samples. Phil. Trans. R. Soc. A 374: 20150428. http://dx.doi.org/10.1098/rsta.2015.0428.

Alfi, M., An, C., Cao, Y., Yan, B., Barrufet, M. A., and Killough, J. E. 2017. Pore Size Variability and Sieving Effect in Liquid Shale - A Multiple Permeability Approach and Eagle Ford Case Study. Society of Petroleum Engineers. doi:10.2118/182643-MS.

Ali, T. A. and Sheng, J. J. 2015. Evaluation of the Effect of Stress-dependent Permeability on Production Performance in Shale Gas Reservoirs. Society of Petroleum Engineers. doi:10.2118/177299-MS.

Alpak, F.O., 2015. Robust Fully-implicit Coupled Multiphase-flow and Geomechanics Simulation. Society of Petroleum Engineers. https://doi.org/10.2118/172991-PA.

Al-Wardy, W., and R. W. Zimmerman. 2004. Effective stress law for the permeability of clay-rich sandstones: Journal of Geophysical Research, v. 109, p. B04203, doi: 10.1029/2003JB002836.

Ambrose, R.J., Hartman, R.C., Diaz Campos, M., and et al. 2010. New Pore-Scale Considerations for Shale Gas in Place Calculations. Society of Petroleum Engineers. DOI: 10.2118/131772-MS.

An, C. 2014. Modeling of Magnetic Nanoparticles Transport in Shale Reservoirs. Master's thesis, Texas A & M University. Available electronically from http://hdl.handle.net/1969.1/154172.

An, C., Alfi, M., Yan, B., Cheng, K., Heidari, Z. and Killough, J. E. 2015. Modeling of Magnetic Nanoparticle Transport in Shale Reservoirs. Society of Petroleum Engineers. doi:10.2118/173282-MS.

An, C., Alfi, M., Yan, B., Killough, J.E. 2016. A new study of magnetic nanoparticle transport and quantifying magnetization analysis in fractured shale reservoir using numerical modeling. J. Nat. Gas Sci. Eng. https://doi.org/10.1016/j.jngse.2015.11.052.

An, C., Fang, Y., Liu, S., Alfi, M., Yan, B., Wang, Y. and Killough, J. 2017b. Impacts of Matrix Shrinkage and Stress Changes on Permeability and Gas Production of Organic-Rich Shale Reservoirs. Society of Petroleum Engineers. doi:10.2118/186029-MS.

An, C., Guo, X., and Killough, J. 2018. Impacts of Kerogen and Clay on Stress-Dependent Permeability Measurements of Shale Reservoirs. Unconventional Resources Technology Conference. doi:10.15530/URTEC-2018-2902756.

An, C., Killough, J., Mi, L. 2019. Stress-dependent permeability of organic-rich shale reservoirs: Impacts of stress changes and matrix shrinkage, J. Petrol. Sci. Eng. 172, 1034-1047. https://doi.org/10.1016/j.petrol.2018.09.011.

An, C., Wang, Y., Wang, Y., Killough, J. 2017d. A modified local error method for adapting time step-size in coupled flow-geomechanics problems, J. Pet. Sci. Eng. 162, 763-773, https://doi.org/10.1016/j.petrol.2017.11.004.

An, C., Yan, B., Alfi, M., Mi, L., Killough, J. E., and Heidari, Z. 2017c. Estimating spatial distribution of natural fractures by changing NMR T2 relaxation with magnetic nanoparticles. J. Pet. Sci. Eng. https://doi.org/10.1016/j.petrol.2017.07.030.

An, C., Zhou, P., Yan, B., Wang, Y., and Killough, J. 2017a. Adaptive Time Stepping with the Modified Local Error Method for Coupled Flow-Geomechanics Modeling. Society of Petroleum Engineers. doi:10.2118/186030-MS.

Armero, F. and Simo, J.C. 1992. A new unconditionally stable fractional step method for non-linear coupled thermomechanical problems. Int. J. Numer. Methods Eng. 35: 737-766.

Augustesen A., Liingaard M., and Lade, P.V. 2004. Evaluation of time-dependent behavior of soils. International Journal of Geomechanics 4(3):137-56.

Bernabe, Y. 1986. The effective pressure law for permeability in Chelmsford granite and Barre granite, Int. J. Rock Mech. Min. Sci., 23, 267-275.

Biot, M.A. 1941. General Theory of Three-Dimensional Consolidation. J. Appl. Phys. 12 (2): 155-164. doi:10.1063/1.1712886.

Biot, M.A. 1956. General Solutions of the Equations of Elasticity and Consolidation for a Porous Material. J Appl. Mech. 27. 91-96.

Boitnott, G., Miller, T. and Shafer, J. 2009. Pore pressure effects and permeability: Effective stress issues for high pressure reservoirs. Int. Symp. of the Society of Core Analysts, Noordwijk aan Zee, Netherlands.

Borja, R.I., 2006. On the mechanical energy and effective stress in saturated and unsaturated porous continua. Int. J. Solids Struct. 43 (6), 1764-1786. https://doi.org/10.1016/j.ijsolstr.2005.04.045.

Boukharov, G.N. and Chanda, M.W. 1995. The three processes of brittle crystalline rock creep. International Journal of Rock Mechanics and Mining Science 32, 325-335.

Brace, W. F. 1965. Some new measurements of linear compressibility of rocks. Journal of Geophysical Research, 70, 391-398. https://doi.org/10.1029/JZ070i002p00391.

Brantut, N., Heap, M. J., Meredith, P. G., and Baud, P. 2013. Time-dependent cracking and brittle creep in crustal rocks: A review, J. Struct. Geol., 52(0), 17-43.

Bustin, R. M., Bustin, A. M. M., Cui, A., Ross, D., and Pathi, V. M. 2008. Impact of Shale Properties on Pore Structure and Storage Characteristics. Society of Petroleum Engineers. doi:10.2118/119892-MS.

Cheng, A.D.H. and Detournay, E. 1988. A Direct Boundary Element Method for Plane Strain Poroelasticity. International journal for Numerical and Analytical Methods in Geomechanics. 12: 551-572.

Chhatre, S. S., Sinha, S., Braun, E. M., et al. 2014. Effect of Stress, Creep, and Fluid Type on Steady State Permeability Measurements in Tight Liquid Unconventional Reservoirs. Unconventional Resources Technology Conference. doi:10.15530/URTEC-2014-1922578.

Chin, L. Y., Thomas, L. K., Sylte, J. E. et al. 2002. Iterative Coupled Analysis of Geomechanics and Fluid Flow for Rock Compaction in Reservoir Simulation. In Oil Gas Sci. Technol. 57 (5): 485-497. http://dx.doi.org/10.2516/ogst:2002032.

Cho, Y., Ozkan, E., and Apaydin, O. G. 2013. Pressure-Dependent Natural-Fracture Permeability in Shale and Its Effect on Shale-Gas Well Production. Society of Petroleum Engineers. doi:10.2118/159801-PA.

Civan, F., Rai, C., Sondergeld, C. 2011. Shale-gas permeability and diffusivity inferred by improved formulation of relevant retention and transport mechanisms. Transport Porous Media 86 (3), 925-944. https://doi.org/10.1007/s11242-010-9665-x.

Connell, L.D. 2009. Coupled flow and geomechanical processes during gas production from coal seams. International Journal of Coal Geology, 79(1-2), 18-28.

Coussy, O. 1995. Mechanics of Porous Continua. John Wiley & Sons, Chichester, England.

Cryer, C. W. 1963. A comparison of the three-dimensional consolidation theories of Biot and Terzaghi. Q. J. Mech. Appl. Math., Vol. 16, 401-412.

Curtis, M.E., Ambrose, R.J., and Sondergeld, C.H. 2010. Structural characterization of gas shales on the micro- and nano-scales. Soc. Pet. Eng. http://dx.doi.org/10.2118/137693-MS.

Dake, L. P. & Knovel (Firm) 1978. Fundamentals of reservoir engineering. Elsevier Scientific Pub. Co.; New York: distributors for the U.S. and Canada Elsevier North-Holland, Amsterdam; New York.

Dake, L. P. 1983. Fundamentals of Reservoir Engineering. Elsevier Science.

Danesh, N.N., Chen, Z., Connell, L., et al. 2017. Characterisation of creep in coal and its impact on permeability: an experimental study. Int. J. Coal Geol. 173: 200-211.

David C., Wong T.F., Zhu W., Zhang J. 1994. Laboratory measurement of compaction induced permeability change in porous rocks: implication for the generation and maintenance of pore pressure excess in the crust. Pure Appl. Geophys. 143:425-56.

Davies, J. P. and Davies, D. K. 1999. Stress-Dependent Permeability: Characterization and Modeling. Society of Petroleum Engineers. doi:10.2118/56813-MS.

Davies, J. P. and Davies, D. K. 2001. Stress-Dependent Permeability: Characterization and Modeling. Society of Petroleum Engineers. doi:10.2118/71750-PA.

Dean, R. H., Gai, X., Stone, C. M., and Minkoff, S. E. 2006. A Comparison of Techniques for Coupling Porous Flow and Geomechanics. Society of Petroleum Engineers. doi:10.2118/79709-PA.

Dicker, A. I., and Smits, R. M. 1988. A Practical Approach for Determining Permeability From Laboratory Pressure-Pulse Decay Measurements. Society of Petroleum Engineers. doi:10.2118/17578-MS.

Durucan, S. and Edwards, J. S. 1986. The effects of stress and fracturing on permeability of coal, Mining Sci. Tech. 3, 205-216.

Ertekin, T., Abou-Kassem, J. H., and King, G. R. 2001. Basic Applied Reservoir Simulation. In Society of Petroleum Engineers Textbook Series, Texas.

Espinoza, C. E. 1983. A New Formulation for Numerical Simulation of Compaction, Sensitivity Studies for Steam Injection. Society of Petroleum Engineers. doi:10.2118/12246-MS.

Evans J.P., Forster C.B., and Goddard J.V. 1997. Permeability of fault-related rocks, and implications for hydraulic structure of fault zones. J. Struct. Geol. 19(11):1393-1404.

Fatt, I. 1958. Pore Volume Compressibilities of Sandstone Reservoir Rocks. Society of Petroleum Engineers. doi:10.2118/970-G.

Fung, L.S.K., Buchanan, L., and Wan, R.G. 1994. Coupled Geomechanical-Thermal Simulation for Deforming Heavy-Oil Reservoirs. J. Cdn. Pet. Tech. 33, No. 4, 22.

Gale, J.F.W., Laubach, S.E., Olson, J.E., Eichhubl, P., Fall, A. 2014. Natural fractures in shale: a review and new observations. AAPG Bull, 98 (11), pp. 2165-2216.

Gear, C. W. 1971. Numerical Initial Value Problems in Ordinary Differential Equations. Prentice-Hall: Englewood Cliffs, NJ.

Ghabezloo S., Sulem J., Gue´don S. 2009. Martineau F., Effective stress law for the permeability of a limestone. Int. J. Rock Mech. Min. Sci. 46:297-306.

Gibson, R.E., Knight, K., Taylor, P.W. 1963. A critical experiment to examine theories of three-dimensional consolidation, in: European Conference on Soil Mechanics and Foundations, Proceedings, Vol. 1, Wiesbaden (Germany), 69-76.

Gilman, A., Beckie, R. 2000. Flow of coal-bed methane to a gallery. Transport in Porous Media 41, 1-16.

Gray, I. 1987. Reservoir engineering in coal seams: Part 1 - The physical process of gas storage and movement in coal seams, SPE Reservoir Eng. 28-34.

Guenther, K. T., Perkins, D. S., Dale, B. A., Pakal, R., and Wylie, P. L. 2005. South Diana, Gulf of Mexico, U.S.A.: A Case Study in Reservoir Management of a Compacting Gas Reservoir. International Petroleum Technology Conference. doi:10.2523/IPTC-10900-MS.

Gutierrez, M., Oino, L., and Nygard, R. 2000. Stress-dependent Permeability of a De-mineralised Fracture in Shale, Marine and Petroleum Geology, 17(8), 895-907.

Heller, R., Vermylen, J., Zoback, M. 2014. Experimental investigation of matrix permeability of gas shales. AAPG Bull. 98 (5), 975-995.

Hughes T.J.R. 1987. The Finite Element Method: Linear Static and Dynamic Finite Element Analysis. Englewood Cliffs, NJ: Prentice-Hall.

Jarvie, D. 2004. Evaluation of hydrocarbon generation and storage in Barnett Shale, Fort Worth Basin, Texas. Paper presented at the Petroleum Technology Transfer Council. The University of Texas at Austin, Bureau of Economic Geology.

Javadpour, F. 2009. Nanopores and apparent permeability of gas flow in mudrocks (Shales and Siltstone). J. Can. Pet. Technol. 48, 16-21.

Jeannin, L., Mainguy, M., Masson, R., and Vidal-Gilbert, S. 2006. Accelerating the Convergence of Coupled Geomechanical-Reservoir Simulations. International Journal for Numerical and Analytical Methods in Geomechanics 31 (10):1163-1181. doi:10.1002/nag.576.

Jonas, E. C. and McBride, E. F. 1977. Diagenesis of sandstone and shale: Application to exploration for hydrocarbons. American Association of Petroleum Geologists Continuing Education Program Publication 1, 120 p.

Katsuki, D., Deben, A. P., Adekunle, O., Rixon, A. J., & Tutuncu, A. N. 2016. Stress-Dependent Permeability and Dynamic Elastic Moduli of Reservoir and Seal Shale. Unconventional Resources Technology Conference. doi:10.15530/URTEC-2016-2461613.

Kim, J. 2010. Sequential methods for coupled geomechanics and multiphase flow. Ph.D. Thesis, Department of Energy Resources Engineering, Stanford University, California, 264 pp.

Kim, J., Tchelepi, H. A., and Juanes, R. 2011a. Stability, Accuracy, and Efficiency of Sequential Methods for Coupled Flow and Geomechanics. Society of Petroleum Engineers. doi:10.2118/119084-PA.

Kim, J., Tchelepi, H.A., and Juanes, R. 2011b. Stability and convergence of sequential methods for coupled flow and geomechanics: Fixed-stress and fixed-strain splits. Comput. Meth. Appl. Mech. Eng. 200(13-16): 1591-1606. http://dx.doi.org/10.1016/j.cma.2010.12.022.

Kim, J.M., 2000. Generalized poroelastic analytical solutions for pore water pressure change and land subsidence due to surface loading. Geosci. J. 4 (2), 95-104.

Kwon, O., Kronenberg, A. K., Gangi, A. F. and Johnson, B. 2001, Permeability of Wilcox shale and its effective pressure law, J. Geophys. Res., 106, 19,339-19,353, doi:10.1029/2001JB000273.

Li, S., Zhang, Q., and Chen, Z. 2013. Experimental Study of Compaction Creep Model of Broken Rock, J. Min. World Express 2, 76-81.

Liu, S., Harpalani, S. 2013. Permeability prediction of coalbed methane reservoirs during primary depletion. International Journal of Coal Geology 113, 1-10.

Liu, X., Liu, J., Liang, N., et al. 2016. Experimental and theoretical analysis of permeability characteristics of sandstone under loading and unloading. Journal of Engineering Science and Technology Review, 9(5):36-43.

Liu, Z., Xie, S., Shao, J., Conil, N. 2015. Effects of deviatoric stress and structural anisotropy on compressive creep behavior of a clayey rock. Appl. Clay Sci. 114, 491-496.

Loucks, R.G., Reed, R.M., Ruppel, S.C., et al. 2012. Spectrum of pore types and networks in mudrocks and a descriptive classification for matrix-related mudrock pores. AAPG Bull. 96 (6), 1071-1098. https://doi.org/10.1306/08171111061.

Luffel, D. L., Hopkins, C. W., and Schettler, P. D. 1993. Matrix Permeability Measurement of Gas Productive Shales. Society of Petroleum Engineers. doi:10.2118/26633-MS.

Mandel, J. 1953. Consolidation des Sols, Ge´otechnique, 7, 287-299.

Mi, L., An, C., Cao, Y., Yan, B., Jiang, H., Pei, Y., and E. Killough, J. 2016. A Guideline on Optimizing Fracture Modeling for Fractured Reservoir Simulation. Society of Petroleum Engineers. doi:10.2118/181814-MS.

Mighani, S., Taneja, S., Sondergeld, C. H., and Rai, C. S. 2015. Nanoindentation Creep Measurements on Shale. American Rock Mechanics Association.

Minkoff, S. E., and Kridler, N. M. 2005. A comparison of adaptive time stepping methods for coupled flow and deformation modeling, Appl. Math. Model., 30, 993-1009.

Minkoff, S.E., Stone, C.M., Bryant, S., Peszynska, M., Wheeler, M.F. 2003. Coupled fluid flow and geomechanical deformation modeling. J. Pet. Sci. Eng. 38, 37-56.

Mokhtari, M., Alqahtani, A. A., Tutuncu, A. N., and Yin, X. 2013. Stress-Dependent Permeability Anisotropy and Wettability of Shale Resources. Unconventional Resources Technology Conference.

Nagel, N.B. 2001. Compaction and subsidence issues within the petroleum industry: from Wilmington to Ekofisk and beyond. Phys. Chem. Earth (A) 26, 3e14.

Neasham, J. W. 1977. Application of scanning electron microscopy to the characterization of hydrocarbon-bearing rocks, Scanning Electr. Microsc. 1, 101-108.

Nishihara, M. 1952. Creep of shale and sandy-shale. J. Geol. Soc. Jpn. 58, 373-377.

Norman, D., Pourciau, R. D., Dusterhoft, R. G., and Schubarth, S. K. 2005. Understanding the Effects of Reservoir Changes in Sand-Control Completion Performance. Society of Petroleum Engineers. doi:10.2118/96307-MS.

Ostermeier, R. M. 1996. Stressed Oil Permeability of Deepwater Gulf of Mexico Turbidite Sands: Measurements and Theory. Society of Petroleum Engineers. doi:10.2118/30606-PA.

Ostermeier, R. M. 2001. Compaction Effects on Porosity and Permeability: Deepwater Gulf of Mexico Turbidite. Society of Petroleum Engineers. doi:10.2118/66479-JPT.

Palmer, I. and Mansoori, J. 1996. How Permeability Depends on Stress and Pore Pressure in Coalbeds: A New Model. Society of Petroleum Engineers. doi:10.2118/36737-MS.

Pan, P. Z., Rutqvist, J., Feng, X. T., Yan, F. 2013. An approach for modeling rock discontinuous mechanical behavior under multiphase fluid flow conditions. Rock Mechanics and Rock Engineering, 1-15, http://dx.doi.org/10.1007/s00603-013-0428-1.

Peaceman, D. W. 1983. Interpretation of Well-Block Pressures in Numerical Reservoir Simulation With Nonsquare Grid Blocks and Anisotropic Permeability. Society of Petroleum Engineers. doi:10.2118/10528-PA.

Peters, L., Arts, R., Brouwer, G., and Geel, C. 2009. Results of the Brugge Benchmark Study for Flooding Optimisation and History Matching. Society of Petroleum Engineers. doi:10.2118/119094-MS.

Petro, D. R., Chu, W. C., Burk, M. K., and Rogers, B. A. 1997. Benefits of Pressure Transient Testing in Evaluating Compaction Effects: Gulf of Mexico Deepwater Turbidite Sands. Society of Petroleum Engineers. doi:10.2118/38938-MS.

Pourciau, R. D., Fisk, J. H., Descant, F. J., and Waltman, B. 2005. Completion and Well Performance Results, Genesis Field, Deepwater Gulf of Mexico. Society of Petroleum Engineers. doi:10.2118/84415-PA.

Profice, S., Lasseux, D., Jannot, Y. et al. 2012. Permeability, Porosity and Klinkenberg Coefficient Determination on Crushed Porous Media. Society of Petrophysicists and Well-Log Analysts.

Raghavan, R. and Chin, L. Y. 2004. Productivity Changes in Reservoirs With Stress-Dependent Permeability. Society of Petroleum Engineers. doi:10.2118/88870-PA.

Rutqvist, J., Wu, Y. S., Tsang, C. F., and Bodvarsson, G. 2002. A modeling approach for analysis of coupled multiphase fluid flow, heat transfer, and deformation in fractured porous rock. Int. J. Rock. Mech. Mining Sci. 39:429-442

Samier, P. and Gennaro, S.D. 2008. A practical iterative scheme for coupling geomechanics with reservoir simulation. SPE Reservoir Eval. Eng. 11 (5), 892–901.

Seidle, J. R. and Huitt, L. G. 1995. Experimental Measurement of Coal Matrix Shrinkage Due to Gas Desorption and Implications for Cleat Permeability Increases. Society of Petroleum Engineers. doi:10.2118/30010-MS.

Settari, A. and Mourits, F.M. 1994. Coupling of geomechanics and reservoir simulation models. Comp. Methods and Advances in Geomech., Siriwardaneand Zeman (eds.), Balkema, Rotterdam, 2151-2158.

Settari, A. T. and Walters, D. A. 1999. Advances in Coupled Geomechanical and Reservoir Modeling With Applications to Reservoir Compaction. Society of Petroleum Engineers. doi:10.2118/51927-MS.

Settari, A. 2002. Reservoir compaction. Journal of Petroleum Technology 54 (8), 62-69.

Shabro, V., Torres-Verdin, C., Javadpour, F. 2011. Numerical simulation of shale-gas production: from pore-scale modeling of slip-flow, knudsen diffusion, and

Langmuir desorption to reservoir modeling of compressible fluid. Soc. Petrol. Eng. https://doi.org/10.2118/144355-MS.

Shampine, L.F. 2004. Error estimation and control of ODEs, J. Sci. Comput. 25 (112) 3-15.

Shi, J.Q. and Durucan, S. 2004. Drawdown Induced Changes in Permeability of Coalbeds: A New Interpretation of the Reservoir Response to Primary Recovery, Transport in Porous Media, 56, 1.

Shumbera, D. A. and Wang, M. 2008. Comparison of Predicted to Field-Measured Compaction Permeability Effects for Gulf of Mexico Deepwater Turbidite Reservoirs by Reservoir Monitoring and Surveillance, Eni E&P Petroleum Engineering Convention.

Sinha, S., Braun, E. M., Determan et al. 2013. Steady-State Permeability Measurements on Intact Shale Samples at Reservoir Conditions - Effect of Stress, Temperature, Pressure, and Type of Gas. Society of Petroleum Engineers. doi:10.2118/164263-MS.

Sinkin, O. V., Holzlöhner, R., Zweck, J., and Menyuk, C. R. 2003. Optimization of the split-step Fourier method in modeling optical-fiber communications systems, J. Lightwave Technol. 21, 61-68.

Skempton, A.W. 1954. The pore pressure coefficients A and B, Ge´otechnique, 4, 143-147.

Skrzypek, J.J. and Ganczarski, A.W. 2015. Mechanics of Anisotropic Materials, Engineering Materials, DOI 10.1007/978-3-319-17160-9_2.

Soeder, D.J. 1988. Porosity and Permeability of Eastern Devonian Gas Shale. SPE Formation Evaluation, pp. 116-124.

Sone H, Zoback MD. 2013. Mechanical properties of shale-gas reservoir rocks - part 2: ductile creep, brittle strength, and their relation to the elastic modulus. Geophysics. 78: D393–402.

Sone, H. and Zoback, M. D. 2010. Strength, Creep And Frictional Properties of Gas Shale Reservoir Rocks. American Rock Mechanics Association.

Sone, H. and Zoback, M. D. 2011. Visco-plastic Properties of Shale Gas Reservoir Rocks. American Rock Mechanics Association.

Spears, R. W., Dudus, D., Foulds, A., Passey, Q., Esch, W. L., and Sinha, S. 2011. Shale Gas Core Analysis: Strategies For Normalizing Between Laboratories And a Clear Need For Standard Materials. Society of Petrophysicists and Well-Log Analysts.

Terzaghi, K. 1923. Die Berechnung der Durchlassigkeitsziffer des Tones aus Dem Verlauf der Hidrodynamichen Span-nungserscheinungen Akademie der Wissenschaften in Wien. Mathematish Naturwissen-Schaftiliche Klasse, Vol. 132, pp. 125-138.

Terzaghi, K. 1925. Erdbaumechanik auf bodenphysikalischer Grundlage, Deuticke, Wien.

Thornton, D.A. and Crook, A.J.L. 2014. Rock Mech. Rock Eng. 47: 1533. doi:10.1007/s00603-014-0589-6.

Tinni, A., Fathi, E., Agarwal, R., Sondergeld, C. H., Akkutlu, I. Y., and Rai, C. S. 2012. Shale Permeability Measurements on Plugs and Crushed Samples. Society of Petroleum Engineers. doi:10.2118/162235-MS.

Tran, D., Settari, A., and Nghiem, L. 2004. New Iterative Coupling between a Reservoir Simulator and a Geomechanics Module. Society of Petroleum Engineers. doi:10.2118/88989-PA.

Verruijt, A. 2013. Theory and Problems of Poroelasticity, Delft University of Technology.

Walls, J. and Nur, A. 1979. Pore pressure and confining pressure dependence of permeability in sandstone, paper presented at 7th Formation Evaluation Symposium, Can. Well Logging Soc., Calgary, Alberta.

Wan, J. 2002. Stabilized finite element methods for coupled geomechanics and multiphase flow. PhD Dissertation, Petroleum Engineering, Stanford University, California.

Wang, F., Mi, Z., Sun, Z., et al. 2017. Experimental Study on the Effects of Stress Variations on the Permeability of Feldspar-Quartz Sandstone. Geofluids, doi.org:10.1155.

Wang, F.P. and Reed, R.M. 2009. Pore networks and fluid flow in gas shales. Soc. Pet. Eng. http://dx.doi.org/10.2118/124253-MS.

Wang, Z., Li, C., and King, M. 2017. Validation and Extension of Asymptotic Solutions of Diffusivity Equation and Their Applications to Synthetic Cases. Society of Petroleum Engineers. doi:10.2118/182716-MS.

Warpinski, N. R. and Teufel, L. W. 1992. Determination of the Effective-Stress Law for Permeability and Deformation in Low-Permeability Rocks. Society of Petroleum Engineers. doi:10.2118/20572-PA.

Watts, H.A. 1984. Step size control in ordinary differential equation solvers, Trans. Soc. Computer Simulation 1, 15-25.

Yan, B., Alfi, M., An, C., Cao, Y., Wang, Y., and Killough, J.E. 2016. General Multi-Porosity simulation for fractured reservoir modeling. J. Nat. Gas Sci. Eng. 33, 777-791.

Yan, B., Wang, Y., and Killough, J. E. 2013. Beyond Dual-Porosity Modeling for the Simulation of Complex Flow Mechanisms in Shale Reservoirs. Society of Petroleum Engineers. doi:10.2118/163651-MS.

Yu, C., Li, H., Wu, R. and Sun, Y. 2016. A Novel Method for Stress Calculation Considering the Creep Behaviour of Shale Gas Reservoir, J. Eng. Sci. and Tech. Review 9 (4), 120-127.

Zhang, F., An, M., Yan, B., Wang, Y., Han, Y. 2019. A novel hydro-mechanical coupled analysis for the fractured vuggy carbonate reservoirs, Computers and Geotechnics, V. 106, 68-82.

Zhang, F., Saputra, I. W. R., Adel, I. A., and Schechter, D. S. 2018. Scaling for Wettability Alteration Induced by the Addition of Surfactants in Completion Fluids: Surfactant Selection for Optimum Performance. Unconventional Resources Technology Conference.

Zhang, S. and Zhu, D. 2017. Inversion of Downhole Temperature Measurements in Multistage Fracture Stimulation in Horizontal Wells. SPE Annual Technical Conference and Exhibition, San Antonio, Texas, USA, 9-11 October. SPE-187322-MS. https://doi.org/10.2118/187322-MS.

Zhu, D., Hill, D., and Zhang, S. 2018. Using Temperature Measurements from Production Logging/Downhole Sensors to Diagnose Multistage Fractured Well Flow Profile. SPWLA 59th Annual Logging Symposium, London, UK, 2-6 June.

Zoback, M. D. and Byerlee, J. D. 1975. Permeability and effective stress. Amer. Assoc. Pet. Geol. Bull. 59, 154-58.

APPENDIX A

STABILITY ANALYSIS FOR THE FIXED-STRESS METHOD

Based on the Fourier decomposition of numerical error, von Neumann stability analysis is widely used to check the stability of finite difference schemes as applied to linear partial differential equations. If the errors calculated at current time step do not cause the errors at future computation to be magnified, a finite difference scheme is regard to stable. In this appendix, the stability of the sequential fixed-stress method is investigated by von Neumann stability analysis, where the one-dimensional coupled single phase flow and geomechanics system is chosen and no source or sink terms are included. The governing equations are presented as Eq. (A-1) and (A-2), where Eq. (A-1) is the mechanics balance equation and Eq. (A-2) is the flow mass balance equation. Fig. 94 shows the schematic of element and element nodes. By plugging the Fourier term expressions as Eq. (A-3) to Eq. (A-6) into Eq. (A-1) and Eq. (A-2), the expanded equations are obtained as Eq. (A-7) and Eq. (A-8). Through dividing Eq. (A-7) by $r^{n+1}\exp(ij\theta)$, dividing Eq. (A-8) by $r^{n-1}\exp(ie\theta)$, and rearranging both equations, the final results are showed on Eq. (A-9) and Eq. (A-10).

$$K_c\left(-\frac{1}{\Delta x}u_{j-1}^{n+1}+2\frac{1}{\Delta x}u_j^{n+1}-\frac{1}{\Delta x}u_{j+1}^{n+1}\right)-\alpha(P_{e-1}^{n+1}-P_e^{n+1})=0 \tag{A-1}$$

$$\left(\phi c_f+\frac{\alpha-\phi}{K_s}+\frac{\alpha^2}{K_c}\right)\frac{P_e^{n+1}-P_e^n}{\Delta t}\Delta x-\frac{\alpha^2}{K_c}\frac{P_e^n-P_e^{n-1}}{\Delta t}\Delta x+\frac{\alpha}{\Delta t}\left(\left(-u_j^n+u_{j+1}^n\right)-\left(-u_j^{n-1}+u_{j+1}^{n-1}\right)\right)$$
$$-\left(\frac{k}{\mu}\frac{P_{e-1}^{n+1}-2P_e^{n+1}+P_{e+1}^{n+1}}{\Delta x}\right)=0 \tag{A-2}$$

$$P_e^n = r^n \hat{P}^0 \exp(ie\theta) \tag{A-3}$$

$$\mu_j^n = r^n \hat{\mu}^0 \exp(ij\theta) \tag{A-4}$$

$$e = j + \frac{1}{2} \tag{A-5}$$

$$e^{i\theta} = \cos(\theta) + i\sin(\theta) \tag{A-6}$$

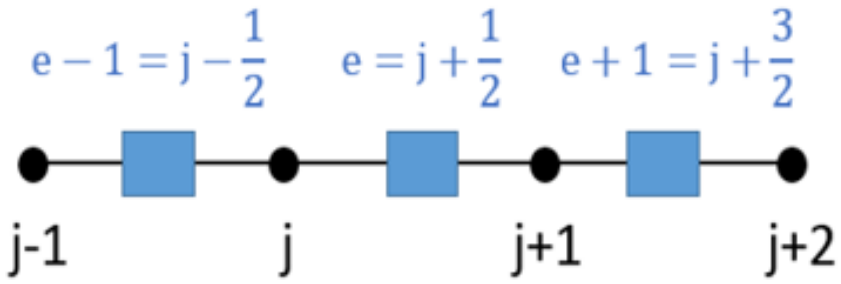

Figure 94: Schematic of element and nodes.

$$K_c\left(-\frac{1}{\Delta x}\gamma^{n+1}\hat{\mu}^0 \exp(i(j-1)\theta) + 2\frac{1}{\Delta x}\gamma^{n+1}\hat{\mu}^0 \exp(ij\theta) - \frac{1}{\Delta x}\gamma^{n+1}\hat{\mu}^0 \exp(i(j+1)\theta)\right) - \alpha\left(\gamma^{n+1}\hat{P}^0 \exp(i(e-1)\theta) - \gamma^{n+1}\hat{P}^0 \exp(ie\theta)\right) = 0 \tag{A-7}$$

$$\left(\phi c_f + \frac{\alpha-\phi}{K_s} + \frac{\alpha^2}{K_c}\right)\frac{\gamma^{n+1}\hat{P}^0\exp(ie\theta) - \gamma^n\hat{P}^0\exp(ie\theta)}{\Delta t}\Delta x - \frac{\alpha^2}{K_c}\frac{\gamma^n\hat{P}^0\exp(ie\theta) - \gamma^{n-1}\hat{P}^0\exp(ie\theta)}{\Delta t}\Delta x + \frac{\alpha}{\Delta t}[(-\gamma^n\hat{\mu}^0\exp(ij\theta) + \gamma^n\hat{\mu}^0\exp(i(j+1)\theta)) - (-\gamma^{n-1}\hat{\mu}^0\exp(ij\theta) + \gamma^{n-1}\hat{\mu}^0\exp(i(j+1)\theta))] - \left(\frac{k}{\mu}\frac{\gamma^{n+1}\hat{P}^0\exp(i(e-1)\theta) - 2\gamma^{n+1}\hat{P}^0\exp(ie\theta) + \gamma^{n+1}\hat{P}^0\exp(i(e+1)\theta)}{\Delta x}\right) = 0 \tag{A-8}$$

$$\frac{K_c}{\Delta x}(2 - 2cos\theta)\hat{\mu}^0 + 2\alpha i sin\frac{\theta}{2}\hat{P}^0 = 0 \tag{A-9}$$

$$\left(\phi c_f + \frac{\alpha-\phi}{K_s} + \frac{\alpha^2}{K_c}\right)\frac{r(r-1)\Delta x}{\Delta t}\hat{P}^0 - \frac{\alpha^2}{K_c}\frac{(r-1)\Delta x}{\Delta t}\hat{P}^0 + \frac{\alpha}{\Delta t}2i(r-1)sin\frac{\theta}{2}\hat{\mu}^0 -$$

$$\frac{kr^2(2cos\theta-2)}{\mu\Delta x}\hat{P}^0 = 0 \qquad \text{(A-10)}$$

The matrix form of Eq. (A-9) and Eq. (A-10) is displayed as below on Eq. (A-11). In order to obtain an effective solution for displacement and pressure, the left side matrix of Eq. (A-11) is required to be singular (Armero and Simo 1992). In other words, an effective solution of r must exist for the determinant of that left matrix $F(r)$ equal to zero, as Eq. (A-12) shows. For linear stability, we need the solution $|r| \leq 1$ (Hughes 1987). After rearranging and removing several terms, the determinant function $F(r)$ can be expressed as on Eq. (A-13). Two roots of r are solved and shown on Eq. (A-14). Apparently, both roots satisfy the criteria of stability $|r| \leq 1$ without any additional requirement. Therefore, the sequential fixed-stress method is unconditionally stable in terms of numerical stability for the couple flow-geomechanics problem.

$$\begin{vmatrix} \frac{K_c}{\Delta x}(2-2cos\theta) & 2\alpha i sin\frac{\theta}{2} \\ \frac{2\alpha i}{\Delta t}(\gamma-1)sin\frac{\theta}{2} & \left(\phi c_f + \frac{\alpha-\phi}{K_s} + \frac{\alpha^2}{K_c}\right)\frac{r(r-1)\Delta x}{\Delta t} - \frac{\alpha^2}{K_c}\frac{(r-1)\Delta x}{\Delta t} - \frac{kr^2(2cos\theta-2)}{\mu\Delta x} \end{vmatrix} \cdot \begin{vmatrix} \hat{\mu}^0 \\ \hat{P}^0 \end{vmatrix} = \begin{vmatrix} 0 \\ 0 \end{vmatrix}$$

(A-11)

$$F(\gamma) = \frac{K_c}{\Delta x}(2-2cos\theta)\left[\left(\phi c_f + \frac{\alpha-\phi}{K_s} + \frac{\alpha^2}{K_c}\right)\frac{r(r-1)\Delta x}{\Delta t} - \frac{\alpha^2}{K_c}\frac{(r-1)\Delta x}{\Delta t} - \frac{kr^2(2cos\theta-2)}{\mu\Delta x}\right] -$$

$$\frac{2\alpha i}{\Delta t}(\gamma-1)sin\frac{\theta}{2}\cdot 2\alpha i sin\frac{\theta}{2} = 0 \qquad \text{(A-12)}$$

$$F(\gamma) = \left(\phi c_f + \frac{\alpha-\phi}{K_s} + \frac{\alpha^2}{K_c} - \frac{(2cos\theta-2)k\Delta t}{\mu\Delta x^2}\right) r^2 - \left(\phi c_f + \frac{\alpha-\phi}{K_s} + \frac{\alpha^2}{K_c}\right) r = 0 \qquad \text{(A-13)}$$

$$r = 0,\ r = \frac{\phi c_f + \frac{\alpha-\phi}{K_s} + \frac{\alpha^2}{K_c}}{\phi c_f + \frac{\alpha-\phi}{K_s} + \frac{\alpha^2}{K_c} + \frac{4k\Delta t}{\mu\Delta x^2}\left(sin\frac{\theta}{2}\right)^2} \qquad \text{(A-14)}$$